

# RADAR-INERTIAL ODOMETRY FOR COMPUTATIONALLY CONSTRAINED AERIAL NAVIGATION

Jan Michalczyk, M.Sc.

## DISSERTATION

submitted in fulfillment of the requirements for the degree of  
*Doctor of Technical Sciences*



University of Klagenfurt  
Faculty of Technical Sciences

### Supervisors

Univ.-Prof. Dr. Stephan Weiss University of Klagenfurt Institute of Smart Systems Technologies	Assoc. Prof. Dr. Jan Steinbrener University of Klagenfurt Institute of Smart Systems Technologies
---	--

### Expert Reviewers

Prof. Konstantinos Alexis, Ph.D. Norwegian University of Science and Technology Department of Engineering Cybernetics	Prof. Martin Saska, Ph.D. Czech Technical University in Prague Department of Cybernetics
---	---

Klagenfurt, September 2025

---

# Affidavit

I hereby declare in lieu of an oath that

- the submitted academic paper is entirely my own work and that no auxiliary materials have been used other than those indicated,
- I have fully disclosed all assistance received from third parties during the process of writing the thesis, including any significant advice from supervisors,
- any contents taken from the works of third parties or my own works that have been included either literally or in spirit have been appropriately marked and the respective source of the information has been clearly identified with precise bibliographical references (e.g. in footnotes),
- I have fully and truthfully declared the use of generative models (Artificial Intelligence, e.g. ChatGPT, Grammarly Go, Midjourney) including the product version,
- to date, I have not submitted this paper to an examining authority either in Austria or abroad and that
- when passing on copies of the academic thesis (e.g. in printed or digital form), I will ensure that each copy is fully consistent with the submitted digital version.

I am aware that a declaration contrary to the facts will have legal consequences.

Jan Michalczyk m.p.

Klagenfurt, September 2025

---

## Disclosure

I hereby declare the use of AI-assisted technologies, including Grammarly and GPT 3.5, as online spell-checking tools during the preparation of this manuscript. Note that none of the aforementioned technologies were directly used to generate complete paragraphs within this thesis.

---

## Acknowledgments

I would like to thank my supervisors, Professor Stephan Weiss and Professor Jan Steinbrener for their support and guidance. My gratitude to you both is beyond words.

I want to thank all my colleagues from the Control of Networked Systems (CNS) group for interesting research discussions as well as great time and fun together.

I wish to thank my parents for sparking my curiosity of the world which eventually led me to the path of a researcher.

Last but not least, I would like to express my deepest appreciation to Professor Martin Saska and Professor Konstantinos Alexis for reviewing this dissertation.

I wish to dedicate this work to my wife Julieta and our daughter Gali♥

---

# Abstract

Radar or RAdio Detection And Ranging, which is a process consisting in transmission and reception of electromagnetic waves enabling the measurement of distance, bearing angle and radial velocity of reflecting objects, has a longstanding history across various domains of engineering. Recently, the progress in the radar sensing technology consisting in the miniaturization of the packages and increase in their measuring precision has drawn the interest of the robotics research community. Indeed, a crucial task enabling autonomy in robotics is to precisely determine the pose of the robot in space. To fulfill this task sensor fusion algorithms are often used, in which data from one or several exteroceptive sensors like, for example, LiDAR, camera, laser ranging sensor or GNSS are fused together with the Inertial Measurement Unit (IMU) measurements to obtain an estimate of the navigation states of the robot. Nonetheless, owing to their particular sensing principles, some exteroceptive sensors are often incapacitated in extreme environmental conditions, like extreme illumination or presence of fine particles in the environment like smoke or fog. Radars are largely immune to aforementioned factors thanks to the characteristics of electromagnetic waves they use. In this thesis, we present Radar-Inertial Odometry (RIO) algorithms to fuse the information from IMU and radar in order to estimate the navigation states of a (Uncrewed Aerial Vehicle) UAV capable of running on a portable resource-constrained embedded computer in real-time and making use of inexpensive, consumer-grade sensors. We present novel RIO approaches relying on the multi-state tightly-coupled Extended Kalman Filter (EKF) and Factor Graphs (FG) fusing instantaneous velocities of and distances to 3D points delivered by a lightweight, low-cost, off-the-shelf Frequency Modulated Continuous Wave (FMCW) radar with IMU

readings. We also show a novel way to exploit advances in deep learning to retrieve 3D point correspondences in sparse and noisy radar point clouds. This thesis advances the knowledge of how lightweight and consumer-grade FMCW millimeter-wave radar sensors can be used together with IMU sensors to build localization systems for UAVs.

---

# Publications

The results presented in this dissertation are included in multiple papers in internationally recognized peer-reviewed conference proceedings.

## Conference papers

- ▲ J. Michalczyk, C. Schöffmann, A. Fornasier, J. Steinbrener, and S. Weiss, "Radar-Inertial State-Estimation for UAV Motion in Highly Agile Manoeuvres", in 2022 International Conference on Unmanned Aircraft Systems (ICUAS), 2022. [IEEExplore]
- ▲ J. Michalczyk, R. Jung, and S. Weiss, "Tightly-Coupled EKF-Based Radar-Inertial Odometry", 2022 IEEE/RSJ International Conference on Intelligent Robots and Systems (IROS), 2022. [IEEExplore]
- ▲ J. Michalczyk, R. Jung, C. Brommer, and S. Weiss, "Multi-State Tightly-Coupled EKF-Based Radar-Inertial Odometry With Persistent Landmarks" 2023 IEEE International Conference on Robotics and Automation (ICRA), 2023. [IEEExplore]
- ▲ J. Michalczyk, M. Scheiber, R. Jung, and S. Weiss, "Radar-Inertial Odometry for Closed-Loop Control of Resource-Constrained Aerial Platforms," 2023 IEEE International Symposium on Safety, Security, and Rescue Robotics (SSRR), 2023. [IEEExplore]
- ▲ J. Michalczyk, J. Quell, F. Steidle, M. G. Müller, and S. Weiss, "Tightly-Coupled Factor Graph Formulation For Radar-Inertial Odometry," 2024 IEEE/RSJ International Conference on Intelligent Robots and Systems (IROS), 2024. [IEEExplore]

- ▲ J. Michalczyk, S. Weiss, and J. Steinbrener, "Learning Point Correspondences In Radar 3D Point Clouds For Radar-Inertial Odometry," 2025 IEEE/RSJ International Conference on Intelligent Robots and Systems (IROS), 2025. Accepted in June 2025 (not yet published). Preprint: [ArXiv]

---

## Acronyms

**CFAR** Constant False Alarm Rate

**CNN** convolutional neural network

**DCS** dynamic covariance scaling

**EKF** extended Kalman filter

**FFT** fast fourier transform

**FIFO** first in first out

**FMCW** frequency modulated continuous wave

**FOV** field of view

**GNSS** global navigation satellite system

**ICP** iterative closest point

**IF** intermediate frequency

**IMU** inertial measurement unit

**LIO** lidar inertial odometry

**LSA** linear sum assignment

**MAE** mean absolute error

**NDT** Normal Distributions Transform

**NEES** normalized estimation error squared

**PCA** Principal Component Analysis

**RANSAC** random sample consensus

**RCS** radar cross section

**RIO** radar-inertial odometry

**RMSE** root mean square error

**RO** radar odometry

**SLAM** simultaneous localization and mapping

**SoC** system on chip

**SVD** singular value decomposition

**SVM** support vector machines

**TTD** total traveled distance

**UAV** uncrewed aerial vehicle

**UGV** uncrewed ground vehicle

**UKF** unscented Kalman filter

**VIO** visual-inertial odometry

---

# Contents

<b>Publications</b>	<b>vii</b>	
<b>1</b>	<b>Introduction</b>	<b>1</b>
1.1	Motivation . . . . .	2
1.2	Contributions . . . . .	3
1.3	Outline . . . . .	4
1.4	Notation . . . . .	5
<b>2</b>	<b>Related Work</b>	<b>7</b>
2.1	Radar-Based State Estimation Using Spinning Radars . . . . .	7
2.2	Radar-Inertial State Estimation Using SoC Radars . . . . .	10
<b>3</b>	<b>The Fundamentals Of Millimeter-Wave FMCW Radar Sensing</b>	<b>16</b>
3.1	Millimeter-Wave FMCW radar sensing . . . . .	16
3.2	FMCW Radar Signal Processing . . . . .	21
3.2.1	Range . . . . .	21
3.2.2	Radial Velocity . . . . .	22
3.2.3	Bearing Angle . . . . .	23
3.2.4	Radar Cross Section . . . . .	25
3.3	Summary . . . . .	25
<b>4</b>	<b>Radar-Inertial Odometry Using The Extended Kalman Filter</b>	<b>26</b>
4.1	EKF RIO using distance measurements to fixed anchors . . . . .	27
4.1.1	Methodology . . . . .	27

4.1.2	Experiments . . . . .	31
4.1.3	Conclusions . . . . .	38
4.2	RIO EKF using distance and Doppler velocity measurements of 3D points . . . . .	39
4.2.1	System Overview . . . . .	39
4.2.2	Radar-Inertial State Estimation . . . . .	40
4.2.3	Experiments . . . . .	47
4.2.4	Conclusions . . . . .	54
4.3	RIO Multi-State EKF using distance, Doppler velocity measurements of 3D points, and persistent landmarks . . . . .	55
4.3.1	System Overview . . . . .	56
4.3.2	Multi-State Radar-Inertial State Estimation With Persistent Landmarks . . . . .	57
4.3.3	Experiments . . . . .	63
4.3.4	Online Calibration and its Impact on the Accuracy and Consistency of The Multi-State EKF RIO . . . . .	66
4.3.5	Multi-State EKF RIO Closed-Loop Flights . . . . .	71
4.3.6	Evaluation of the State Estimation in the Artificial Fog . . . . .	74
4.3.7	Conclusions . . . . .	75
4.4	Conclusions . . . . .	78
<b>5</b>	<b>Radar-Inertial Odometry Using Factor Graphs</b>	<b>79</b>
5.0.1	Estimator Overview . . . . .	80
5.0.2	Factors . . . . .	82
5.0.3	Partial Marginalization . . . . .	84
5.1	Results . . . . .	85
5.1.1	Experimental Setups . . . . .	85
5.1.2	Evaluation . . . . .	87
5.2	Conclusions . . . . .	88
<b>6</b>	<b>Sparse And Noisy 3D Radar Point Cloud Matching Using Deep Learning</b>	<b>94</b>
6.1	Learning 3D Point Correspondences In Radar 3D Point Clouds	94
6.1.1	Network Architecture . . . . .	95
6.1.2	Network Training And Inference . . . . .	96
6.2	Results . . . . .	99
6.2.1	Experiments . . . . .	99
6.2.2	Evaluation . . . . .	101
6.3	Conclusions . . . . .	106
<b>7</b>	<b>Discussion and Conclusions</b>	<b>110</b>

<i>CONTENTS</i>	xiii
7.1    Discussion . . . . .	110
7.2    Conclusions . . . . .	111
<b>Bibliography</b>	<b>113</b>

---

# List of Figures

2.1	Spinning and SOC radar sensor examples . . . . .	8
3.1	Single FMCW linear chirp . . . . .	18
3.2	Radar frame consisting of several FMCW linear chirps . . . . .	18
3.3	Radar cube consisting of measurements across multiple antennas	19
3.4	CFAR algorithm . . . . .	20
3.5	Angles resolution in FMCW radars using multiple antennas . .	24
4.1	Range-amplitude plot from FFT processing . . . . .	29
4.2	Experimental UAV platform used for state estimation using fixed anchors . . . . .	31
4.3	Corner reflectors used as fixed anchors . . . . .	31
4.4	Corner reflectors as seen from the onboard camera . . . . .	33
4.5	Ground truth trajectory of the UAV above corner reflectors . .	33
4.6	Range-Doppler map generated from sensing corner reflectors . .	34
4.7	Ranges measured matched to ground truth ranges . . . . .	34
4.8	Absolute position estimation error in feature-rich scenario . .	36
4.9	Absolute position estimation error in feature-poor scenario . .	37
4.10	Attitude estimation error in feature-rich scenario . . . . .	37
4.11	Estimated IMU-radar translation . . . . .	38
4.12	Spatial frames arrangement in the two-frame RIO method . . .	40
4.13	Relative coherence between 3D points in subsequent scans . . .	44
4.14	Matched 3D points between two scans . . . . .	45
4.15	Experimental platform with TI radar mounted . . . . .	48
4.16	Indoor space used for experiments . . . . .	49
4.17	Top view of the uncrewed aerial vehicle (UAV) 3D trajectory .	50
4.18	Side view of the uncrewed aerial vehicle (UAV) 3D trajectory .	50

4.19	Estimated position in the approach with one past frame	51
4.20	Estimated attitude in the approach with one past frame	52
4.21	Estimated velocity in the approach with one past frame	53
4.22	Drift over the TTD in the approach with one past frame	53
4.23	Measurement trails used in multi-frame approach	57
4.24	Spatial arrangement of frames in the multi-state EKF RIO	58
4.25	Augmentation of the state and covariance with a persistent landmark	62
4.26	Experimental platform and the scene used for evaluation of the multi-state approach	66
4.27	Sample of the executed trajectories for evaluation of the multi-state approach	67
4.28	Mean of the norm of MAE for the multi-state approach	67
4.29	Mean of the norm of mean absolute error (MAE) for the flown dataset with online calibration	69
4.30	Comparison of the position estimation errors and the $\pm 3\sigma$ uncertainty envelopes	70
4.31	Comparison of the position NEES	71
4.32	Convergence of the rotational extrinsic calibration parameters in the multi-state approach	72
4.33	Convergence of the translation extrinsic calibration parameters in the multi-state approach	73
4.34	Closed-loop flight 3D plot top-view	74
4.35	Closed-loop flight 2D plot	75
4.36	Sequence of the images used by the OpenVINS to track features	76
4.37	Comparison of position estimates for the flight in the fog	76
4.38	Experimental platform and the scene used in the flight in the fog evaluation	77
5.1	Experimental platforms CNS UAV and ARDEA-X	80
5.2	Snapshot of the sliding window of states and measurements and the corresponding factor graph	81
5.3	Initialization of the newest inertial measurement unit (IMU) state in the sliding window	82
5.4	Marginalization of the oldest inertial measurement unit (IMU) state	86
5.5	Sample trajectories from each dataset with the take-off and landing points	89
5.6	Estimated position of the UAV using both FG and EKF methods - trajectory 1	90

5.7	Estimation results for the position of the UAV using both FG and EKF methods - trajectory 2 . . . . .	91
5.8	Plot of the estimates of position of the UAV using both FG and EKF methods - trajectory 3 . . . . .	92
5.9	Plot of convergence of the mean of errors in speed (norm of the velocity) in the case of incorrect velocity initialization for both methods . . . . .	93
6.1	Architecture of the network for radar 3D point matching . . . . .	97
6.2	Inferred correspondence likelihood matrix and matches . . . . .	100
6.3	Platforms used in experiments and the Doppler-only trajectory	102
6.4	Method performance on coloradar dataset . . . . .	103
6.5	Position estimates for the ARDEA-X flight . . . . .	104
6.6	Attitude estimates for the ARDEA-X flight . . . . .	105

---

## List of Tables

4.1	Experiments and root mean square error (RMSE) after convergence . . . . .	36
4.2	Initial standard deviation of the navigation states in the two-frame method experiments . . . . .	48
4.3	Evaluation metrics for the multi-state approach . . . . .	65
4.4	Execution timings for the multi-state approach . . . . .	65
4.5	Metrics for the closed-loop flights evaluation . . . . .	73
4.6	Onboard execution timings . . . . .	73
5.1	Evaluation of position estimates for both EKF and FG methods	88
6.1	Evaluation of position for both DL and classical matching methods	107
6.2	Evaluation of attitude for both DL and classical matching methods	108

# CHAPTER 1

---

## Introduction

Achieving accurate spatial awareness in global navigation satellite system (GNSS)-denied environments is a key task for a reliably operating autonomous uncrewed aerial vehicle (UAV) in many scenarios. Most notably, it is a prerequisite for controlling the motion of a UAV in space. This task is commonly approached by the fusion of measurements from a combination of sensors within a state estimation framework.

In the area of UAVs localization without GNSS support, a prominent place is held by visual-inertial odometry (VIO) approaches employing a camera and an inertial measurement unit (IMU) [32, 46, 58]. This prominence is partly due to the rich information provided by camera sensors which paved the way to the significant body of research devoted to using computer vision and image processing techniques in robot navigation in recent years. Nonetheless, camera sensors exhibit drawbacks rendering them vulnerable in certain environmental conditions such as extreme illumination (both very low and high), lack of features, or presence of air obscurants like fog or smoke. Other limiting factors for camera-based perception systems include sharp motions causing image blur, lack of metric measurements, and in some contexts, privacy issues related to grabbed images.

LiDAR-based odometry systems for small-sized robots are mentioned in [85] and [86]. LiDAR uses time-of-flight of laser pulses from the visible spectrum to generate fine-grained 3D point clouds. Given the spectrum of used pulses, LiDAR is susceptible to same environmental factors as cameras. Using shorter wavelengths also reduces the range of measurements.

Recently, fusing millimeter-wave frequency modulated continuous wave (FMCW) radar and IMU measurements has gained popularity in the UAVs autonomy research. A setup composed of these two sensors offers not only

robustness against low-visibility environments, but also long-range perception thanks to the properties of electromagnetic waves used in radars [43, 65, 63], and allows for IMU drift reduction, enabling accurate ego-motion estimation even in conditions challenging to camera or LiDAR-based setups.

Several kinds of FMCW radars have been used in the context of autonomous navigation. The most common ones are scanning radars [36, 11, 6, 64] and system on chip (SoC) radars [53, 54, 31, 61, 43, 48, 65, 23, 4]. Scanning radars are bulky and expensive mechanically rotating sensors. After performing a  $360^\circ$  scan they provide polar images of the environment with a high angular resolution. They typically do not provide the relative velocity (Doppler) information. SoC radars are usually much smaller in size and require less power. SoC radars output distance, relative radial velocity, azimuth (and sometimes elevation) angles of reflecting points in the environment in the form of a 4D pointcloud (3D position and Doppler velocity). Their accuracy and resolution vary broadly depending on the antenna array characteristics and on-chip processing algorithms. Using millimeter-wave technology in automotive industry [35, 69, 71] brought about the miniaturization of the radar sensors and boosted their accuracy. This in turn, paved the way for using them onboard small UAVs and uncrewed ground vehicle (UGV)s for fusion with the IMU sensors. Interestingly, current generation SoC radars price tags vary significantly as a function of the sensor characteristics and range between several tens (consumer-grade) to several thousands (industry-grade) of euros.

It seems both challenging and appealing to try to build an accurate localization system for a UAV exploiting solely consumer-grade sensors. Hence, in this dissertation we explore methods to leverage measurements from consumer-grade millimeter-wave FMCW SoC radar and fuse them together with IMU sensor measurements in radar-inertial odometry (RIO) state estimation frameworks with the goal of endowing small UAVs with accurate localization capabilities in unknown and potentially visually degraded environments.

## 1.1 Motivation

Since several years, a standard approach to estimating the odometry of a small UAV or UGV, a setup consisting of a camera and an IMU has been used with impressive results. Nonetheless, there exist potential deployment conditions which incapacitate camera sensors rendering the state estimates unusable. These conditions are, however, not as challenging to radar as they

are to a camera. When aiming at the environmental resilience, it is therefore purposeful to build robot localization systems based on radar. Given the research community interest, and the increasing prevalence of millimeter-wave FMCW radars lending themselves to usage in robotics due to their cost, size and power consumption, there is also a need to research effective methods to use these sensors in robotic tasks. Recently, works which aim at closing this gap started to appear such as [23, 24, 22, 25]. Nonetheless, given the rich information about the environment which radar sensors perceive and the large knowledge in state estimation theory applied to other sensor setups such as VIO and lidar inertial odometry (LIO), there exists large room for improvement and still many promising research avenues to explore in the area of RIO research. In this dissertation we aim at expanding the knowledge on fusing together consumer-grade FMCW radar and IMU data in order to estimate the navigation state of small-sized UAVs as well as pushing the boundaries of the state-of-the-art in terms of accuracy obtained by designed state estimators.

## 1.2 Contributions

The core contributions of this thesis are:

- *Tightly-coupled formulation to include both radar distance and velocity measurements for IMU integration correction in an extended Kalman filter (EKF) framework, allowing accurate 3D velocity and 6DoF pose estimation.*
- *Application of stochastic cloning for inclusion of single and multiple past robot poses used for formulating an update equation on the accurately measured distances (rather than on the full 3D point positions polluted by the highly imprecise azimuth and elevation angular measurements) to multiple points in radar measurement trails allowing the extension of the initial single-state EKF approach into a multi-state EKF RIO.*
- *Improved 3D point matching across sparse, noisy radar scans in full 6DoF motion allowing ad-hoc point correspondence generation for point-distance based observation inclusion with only past radar poses (or a single radar pose) in the state in contrast to maintaining many 3D point vectors in the state.*
- *Efficient trail generation/handling for using past measurement-trails and extension of the radar feature matching to work with the trails of*

*features as well as extension of the distance measurement update to work with the measurement trails in the EKF.*

- *Introduction of the online estimation of the extrinsic calibration parameters and thus simplifying the use of the EKF framework as well as improving its accuracy and consistency.*
- *Tightly-coupled formulation of a sliding window factor graph-based RIO making maximal use of all the noisy measurements from a light-weight, inexpensive SoC FMCW radar sensor to correct the IMU drift.*
- *Implementation of persistent radar landmarks for increased estimation accuracy in both EKF and factor graph method as well as their inclusion in the update equation of the EKF and as a factor in the factor graph.*
- *One-to-one comparison of the factor graph RIO with the multi-state EKF-based RIO.*
- *Implementation of both RIO frameworks capable of executing in real-time on a portable resource-constrained credit-card sized onboard computer allowing the evaluation of the implemented framework in closed-loop control flights.*
- *Deep learning framework for predicting robust correspondences in sparse and noisy FMCW SoC radar 3D point clouds, in which the formulation of the learning problem is posed as multi-label classification which allows training (using self-supervised method not requiring hand annotated ground-truth data) on the sparse and noisy 3D point clouds yet results in unambiguous matches.*

The source code of the implementation of both the EKF and factor graph methods is made open-source and available here: [https://github.com/aaucns/aaucns\\_rio](https://github.com/aaucns/aaucns_rio).

### 1.3 Outline

The remaining chapters of this thesis are organized as follows. In **chapter 2** and **chapter 3** we introduce the related work and the fundamentals of radar sensing. In particular, **chapter 2** introduces the most recent advances in the area of radar-based state estimation discussing methods based on the SoC as well as spinning FMCW radars, methods making use

of the Doppler velocity only as well as methods utilizing also 3D point matches. We mention both classical and learning-based RIO methods. In some cases, mostly the case of imaging (mechanically spinning) radars, we introduce methods which rely solely on radar and are thus radar odometry (RO) methods. In the **chapter 3** we outline the necessary principles related to the radar sensing. We also show the signal processing pipeline in a FMCW SoC radar leading to the measurement of 3D points and Doppler velocities. In **chapter 4** we present our progressive research within the EKF-based RIO which led to the final formulation of the multi-state RIO with self-calibration capabilities. We show how this final implementation is used in closed-loop flights and how it successfully deals with deployment in the dense *artificial* fog where a state-of-the-art VIO fails. In **chapter 5** we present an implementation of RIO based on the optimization of factor graphs. We compare and contrast this state estimation formalism with the presented earlier EKF-based one. In **chapter 6** we propose a learning framework based on the transformer architecture to learn point correspondences between pairs of sparse and noisy 3D point clouds measured by SoC FMCW radar sensor. At the end, in the **chapter 7**, we offer closing discussion and conclusions.

## 1.4 Notation

In this section we introduce the notation used throughout this dissertation.

Vector spaces are denoted with blackboard letters such as  $\mathbb{X}$ . Vectors expressing elements of some  $n$ -dimensional vector space  $\mathbb{X} \subset \mathbb{R}^n$  are denoted by lowercase bold letters such as  $\mathbf{x}$ . Matrices representing linear operators on vector spaces are denoted by capital bold letters such as  $\mathbf{X}$ .

Vectors describing quantities  $\mathbf{x}$  of a target object  $\{B\}$ , observed from a *frame of reference*  $\{O\}$  and expressed in a *frame of reference*  $\{A\}$ , are denoted by  ${}_O^A \mathbf{x}_B$ . Note that when the observer frame and the coordinate frame coincide, the left subscript is dropped  ${}_A^A \mathbf{x}_B = {}^A \mathbf{x}_B$ .

Thus, to denote the translation between a frame of reference  $\{A\}$  and a frame of reference  $\{B\}$  expressed in the frame of reference  $\{A\}$  we write  ${}^A \mathbf{p}_B$ . To denote the relative velocity of a moving frame of reference  $\{B\}$  expressed in a frame of reference  $\{A\}$  we write a vector  ${}^A \mathbf{v}_B$ .

Rotation matrices encoding the orientation of a frame of reference  $\{B\}$  with respect to a reference  $\{A\}$  are denoted by  ${}^A \mathbf{R}_B$ . In particular,  ${}^A \mathbf{R}_B$  is the matrix whose columns are the orthonormal vectors defining the axes of  $\{B\}$  expressed in  $\{A\}$ :

$${}^A \mathbf{R}_B = \begin{bmatrix} {}^A \mathbf{e}_{B_x} & {}^A \mathbf{e}_{B_y} & {}^A \mathbf{e}_{B_z} \end{bmatrix} \in \mathbb{R}^{3 \times 3}.$$

Pose matrices encode simultaneously the orientation and the translation of a frame of reference  $\{B\}$  with respect to a reference  $\{A\}$ , and are denoted by  ${}^A\mathbf{T}_B$ , as in

$${}^A\mathbf{T}_B = \begin{bmatrix} {}^A\mathbf{R}_B & {}^A\mathbf{p}_B \\ \mathbf{0}_{1 \times 3} & 1 \end{bmatrix} \in \mathbb{R}^{4 \times 4}.$$

The transformation of a vector  ${}^C\mathbf{p}_{P_1}$  pointing from the origin of the reference frame  $\{C\}$  to a point  $P_1$ , expressed in  $\{C\}$ , can be transformed into the frame  $\{A\}$  by  $\begin{bmatrix} {}^A\mathbf{p}_{P_1} \\ 1 \end{bmatrix} = {}^A\mathbf{T}_C \begin{bmatrix} {}^C\mathbf{p}_{P_1} \\ 1 \end{bmatrix}$  (read as  ${}^{from}_{in} \mathbf{x}_{to}$ ). A normally distributed multivariate variable is defined as  $\mathbf{X}_i \sim \mathcal{N}(\mathbf{x}_i, \Sigma_{ii})$ , with a mean  $\mathbf{x}_i$  and covariance (uncertainty)  $\Sigma_{ii}$ , which is called the belief of  $i$ . We often express rotations as unit quaternion  $\bar{\mathbf{q}} \in \text{SO}(3)$  with  $\|\bar{\mathbf{q}}\| = 1$  allowing a direct mapping between rotation matrices and unit Hamiltonian quaternions by  ${}^A\mathbf{R}_B = \mathbf{R}\{{}^A\bar{\mathbf{q}}_B\} \in \text{SO}^3$  and  ${}^A\bar{\mathbf{q}}_B = \bar{\mathbf{q}}\{{}^A\mathbf{R}_B\}$  [75].  $\mathbf{I}$  is the identity matrix. The *a priori* and *a posteriori* of a belief are indicated by a  $\{\bullet\}^{(-)}$  and  $\{\bullet\}^{(+)}$ , respectively.  $\{\bullet\}^{\#}$  specifies measured (perturbed) quantities. For vectors and block matrices, semicolons and colons improve the readability such that  $[\mathbf{A}; \mathbf{B}] \equiv \begin{bmatrix} \mathbf{A} \\ \mathbf{B} \end{bmatrix}$  and  $[\mathbf{A}, \mathbf{B}] \equiv [\mathbf{A} \mathbf{B}]$ . We use capital calligraphic letters to denote sets, for example,  $\mathcal{L}$  is a set of landmarks, while  $\mathcal{R}$  is a set of extrinsic calibration state variables corresponding to the position and orientation of the radar sensor with respect to the IMU. Sometimes we use small calligraphic letters to denote elements of sets, for example,  $\ell$  is a single landmark.

# CHAPTER **2**

---

## Related Work

This chapter presents the relevant recent scientific work in the area of radar-based state estimation. Given the diversity in measurements quality and density among radar sensors, some approaches presented in this chapter will rely only on radar for the task of state estimation. This is mostly the case with mechanically spinning radars, but also with some higher-end SoC radars. In these approaches, the IMU sensor is omitted rendering the respective methods radar-only, thus RO. Though mechanically spinning radars have the same underlying principle of sensing as their SoC counterparts, given their highly superior perception quality, they can be considered a different class of sensors. Spinning radars are sometimes called *imaging* radars, due to their finer spatial granularity. Although in this thesis the focus is set on using consumer-grade, inexpensive and lightweight SoC radar variants, it is still meaningful to consider relevant works with spinning radars, as some concepts from the state estimation using spinning radars can and are still be exploited with SoC radar sensors.

### 2.1 Radar-Based State Estimation Using Spinning Radars

Scanning radars rotate around their vertical axis while continuously emitting frequency-modulated radio-frequency waves. Along each azimuth angle (determined by the number of discrete azimuth bins) the sensor measures power returns at discrete range bins. These sensors possess a remarkable feature of being able to sense detections up to around 500 m while spanning 360° in azimuth. Unlike SoC version, the spinning radars provide neither



Figure 2.1: Examples of a spinning (left) and SoC (right) radar sensors mentioned in the following sections. The depicted SoC radar is a high-end automotive radar (Continental ARS548) used in [87, 38]. For an example of consumer-grade radar sensors (used in this work) see figure 4.2 and figure 4.15. (Spinning radar example is taken from <https://navtechradar.com/>).

the elevation nor (typically) the Doppler information resulting in the planar perception. Given low scanning frequencies (4 Hz for NavTech CIR 304-H), the scans exhibit distortions due to the motion of the platform on which they are mounted [34]. Some localization methods explicitly compensate for this effect as in [9]. A number of radar-based localization and simultaneous localization and mapping (SLAM) methods have been presented in the scientific community in the past few years exploiting mechanically rotating FMCW radars. These significant contributions have been made mostly in the autonomous driving and mining domains given the size, cost and power requirements of this sensor.

One of the pioneering works which sparked resurgence in research into SLAM was [13] where the authors use a rotating radar to implement RO estimating the ego-motion of a vehicle, making use of landmarks extraction based on estimating the signal noise statistics and subsequent matching of these landmarks exploiting local geometrical relationships between them within the scan. The estimated signal noise statistics are used to scale the power spectrum which is subsequently searched for peaks. Their matching algorithm does not require any prior guess of the transform between the scans and relies on exploiting the unary descriptors as well as the mutual geometrical relationships between the landmarks. Once the proposed set of matches is returned based on the unary descriptors, a positive-semi

definite matrix is built based on the pairwise similarity of the proposed matches. In the next steps, the normalized eigenvector of the maximum eigenvalue is found and used within greedy search to find iteratively the best set of matches which serves to estimate the relative motion using the singular value decomposition (SVD). Once the relative motion is recovered, the scans can be re-aligned and a second round of association and motion estimation takes place. In the second round, the only difference is the kind of unary descriptors used to describe landmarks.

Authors in [36] aim at achieving a SLAM system able to function under extreme weather conditions. To this end, they propose a RO system using a scanning radar incorporating pose tracking, local mapping, loop closure detection and pose graph optimization. The authors present a novel point cloud generation algorithm robust to noise in radar images which exploits modeling of the power along each azimuth by a Gaussian distribution. Pose tracking is achieved by point matching between the current frames and keyframes. Specifically, SURF features are extracted in both frames, which are subsequently matched using motion prior and pairwise consistency constraint (as in [13]). Matched points are used to calculate the relative transformation using SVD. Once a new keyframe is created, the mapping thread optimizes jointly the poses of keyframes and the belonging keypoints. Once a loop is detected, the pose graph optimization is performed on all keyframes and all keypoints are updated to form a global map. The approach is shown to outperform the results presented in [13].

In [6], a convolutional neural network (CNN)-based RO is introduced capable of predicting robust features in radar scans, which are then used to estimate the optimal relative transformation. In particular, the authors design a deep learning architecture self-supervised with the odometry error. The architecture achieves self-supervision by embedding the differentiable SVD for point-based motion estimation. The output of the learned model are the keypoints, descriptors and scores. Owing to the learning problem formulation the learned keypoints are well-tailored to the localization task and assumptions-free as opposed to the hand-designed keypoints. The authors claim improvement over the method in [13] by 45 % in translation and 29 % in rotation respectively, and order of magnitude faster runtime. This result suggests that learned features enables surpassing the performances achieved with hand-designed features.

In [64] a direct RO approach is shown using the entire radar scan as opposed to only extracted features. Namely, the application of Fourier-Mellin transform to Cartesian and log-polar scans is explored to obtain translation and rotation of the robot, respectively. Even though direct methods require heavy computations as they operate on full scans, the presented

approach achieves real-time performance at 10 Hz thanks to coarse-to-fine pre-processing of the radar images. Odometry is computed using pose graph optimization.

In [2] the authors incorporate the vehicle dynamics of the platform in order to refine the landmarks association from [13]. Making assumptions on the platform motion allows for rejecting associations which do not conform to the constant-curvature motion constraints imposed by the assumed model. Found correspondences are used to calculate the relative motion between the scans using SVD. [12] presents an approach in which state estimation and features learning are combined within an RO framework. As opposed to [6], the features are learned without any supervision only using the onboard sensor data and the estimator is not required to be differentiable.

Authors in [3] address the problem of uncertainty-driven fault detection in RO. This is an important problem in automotive platforms where discontinuities in observed features can occur when the platform does not move on ideally planar surface, the distinct features become scarce or when motion of objects in the scene causes the features to disappear. The authors aim at providing an introspection capability to the RO from [13] where the correspondence-finding algorithm delivers also its confidence in the matched features which is subsequently used to judge whether to accept it for updating the pose or not. In particular, the authors train a classifier to mark the RO estimate as either good or bad based on the ground-truth labels from GNSS and IMU sensor streams and the input radar data. It is noted that the principal eigenvector components, which are used for retrieving matches within radar scans, are very distinct for the cases where the pose estimates are marked good and bad. This observation allows for training an support vector machines (SVM) classifier predicting whether or not the association between two scans can be used for pose estimation. In [10] the authors show a 45 % improvement in their continuous-time RO framework using gaussian process motion prior by additionally incorporating an IMU sensor.

## 2.2 Radar-Inertial State Estimation Using SoC Radars

One of the expected advantages of small-sized UAVs and UGVs is their ability to be deployed in complex and hostile environments such as disaster zones, areas with adverse weather conditions, or hazardous industrial

zones to perform autonomous missions such as reconnaissance, inspection, search and rescue, and others. In order to operate autonomously in such environments, the localization system of the platform must make use of sensors robust towards phenomena such as fog, smoke or extreme illumination. Since recently, thanks to their physical properties, their miniaturization, and general advances in their technology, radar sensors are being increasingly investigated for their use in navigation of various types of autonomous robots requiring resilience towards unfavorable environment factors. Another key requirement of an onboard localization system on an autonomous mobile robot is the need to execute within the tight limits imposed by the real-time control loop and often on a resource-constrained computing platform.

While information-rich, the bulky and expensive scanning radars are inadequate for use on small-sized UAVs or UGVs mostly due to their size and power consumption. Indeed, we focus more on the application of low-cost and small single-chip FMCW radars on UAV, where the payload is of crucial relevance. SoC radars integrate antennas and all necessary signal processing hardware within a single printed circuit board. 4D SoC automotive radar sensors which are the ones mostly used in the robotics research can broadly be divided into higher-end sensors which are based on the cascaded design and which have much better sensing parameters in terms of point cloud resolution and maximum attainable range (Altos V2, Continental ARS548), and lower-end sensors (Texas Instruments AWR1843). The former are an order of magnitude costlier than the latter ones, while also being heavier and more power-greedy. Within this thesis we focus on the lower-end radar sensors in order to minimize the weight, size and power consumption of the designed localization systems so that they can be used even on small-size UAVs.

Pioneering works in the area of RIO for small autonomous robots using lower-end mmWave FMCW SoC radar (Texas Instruments AWR1843) are introduced in [23, 24, 26, 22] where the authors present a real-time RIO method in which the platform velocity estimated from a single radar scan is fused in a loosely-coupled manner with IMU readings in an EKF framework. In [24] the authors extend the method presented in [23] with online calibration of radar extrinsic parameters which boosts the accuracy and simplifies the usage of the approach. Nonetheless, the barometer sensor is additionally used in order to mitigate the vertical drift of the platform, hence the approach is not a pure RIO using a radar and an IMU only. In [26] the same EKF framework is further augmented with the yaw aiding using Manhattan assumptions on the environment thanks to which the method attains high accuracy with minimal run-time footprint. Higher accuracy is achieved at

the expense on imposing constraints on the environment which is a limiting factor. In [22] still the same method is equipped with GNSS sensor providing a versatile and precise outdoor localization solution, nonetheless at the expense of introducing a dependency on GNSS reception. In all of their approaches the authors of [23, 24, 26, 22] decide not to use any form of 3D radar point cloud matching in their EKF. They incorporate only Doppler radar measurements using random sample consensus (RANSAC) based least-squares estimator. Radar processing and transmission delays are accounted for, in order to make the approach resilient to dynamic motion and usable for online-control, by hardware-triggering radar measurements and stochastically cloning the state corresponding to the triggered measurement which is then used for the ego-motion estimation. The approach to RIO presented in this thesis, in contrast, additionally makes use of the point correspondences between radar scans, which allows to reduce the cumulative drift with respect to Doppler-only methods as also mentioned in [89]. Also, tracking point correspondences in time as done in this thesis enables the potential use of the *persistent features* which can be further used to increase the accuracy of the estimators as explained in chapter 4.

Another early approach exploiting the Texas Instruments AWR1843 radar sensor is shown in [4]. The authors demonstrate a RIO approach on a small indoor UGV, interestingly, only making use of the radar 3D point cloud matching. Their system comprise a point association module and the following scan registration using Normal Distributions Transform (NDT). Relative displacements are subsequently fused with the IMU measurements in an unscented Kalman filter (UKF). The authors test their approach in a small-scale, flat, indoor environment with UGV performing a low-dynamics trajectory, it is therefore an open question how the proposed system would perform in dynamic flights of a UAV as is the focus of this thesis.

In [43] and [42] an optimization-based approach is shown where a sliding window of past radar and IMU measurements is used to estimate the UAV velocity. In the constructed factor graph only Doppler factors are used from the radar output. The Doppler residuals are weighted by the normalized point intensity. The IMU residuals are formulated between two radar measurements only considering orientation, velocity and biases. The approach in [43] attains comparable performance with the vision-based system and even outperforms it in visually degraded settings. Additionally, in [42] the authors add a comparison of their method with a lidar-based approach and propose a method to reduce the noise in the radar point clouds based on Deep Learning. The authors in both [43] and [42] concentrate on estimating the ego-velocity instead of the full 6D pose. Also, both approaches have not

yet been demonstrated in closed-loop flights. The factor graph approach presented in this thesis additionally adds tightly-coupled factors on point correspondences, Doppler velocities and persistent features.

In [38] the authors design a RIO system based on a higher-end automotive Continental ARS548 radar. In their implementation both Doppler velocity and point matches are used in a sliding-window nonlinear optimization backend estimator. Noise in the radar scans is addressed by measurements pre-processing. The latter involves removing points outside of the field of view (FOV), radius filter eliminating points excessively far from other points and IMU-aided outlier removal based on velocity. Apart from making use of the classic residual on Doppler velocity similar to other approaches in which a projection of the ego-velocity on the unit vector pointing towards a detection is used, the presented approach uses point matching guided by the radar cross section (RCS) value of detections, which assumes that big changes in RCS within subsequent scans are inconsequential. Same authors in [87] augment their system from [38] by modeling the radar points uncertainty in polar coordinates and incorporating it in both the frontend and backend of their state estimation framework. This important idea has also been explored in [67] where it has been noted that the uncertainty of detections is greatly influenced by the physics of radar sensing and the modeling in the Cartesian space tends to produce underconfident measurements at close ranges and overconfident measurements at far ranges. Proper physical modeling of the radar sensing uncertainty in [87] allows for fine-grained weighting of radar residuals in the backend, but also for guiding the 3D points association. Real-world experiments show the benefits of including their confidence model of radar measurements on the accuracy in the state estimation. As opposed to the work in this thesis, the above work employs a high-end automotive SoC radar and the tests are carried out using a small UGV.

In [62] the authors present an optimization-based continuous-time RIO method which is particularly well suited for multi-radar setups as the continuous representation of the vehicle trajectory allows sampling it at any given time, thus permitting efficient asynchronous fusion of multiple radars measurements with the IMU. The method in [62] is demonstrated on an automotive platform with high-performance cascaded radars, an order of magnitude costlier, and still of greater size than the single-chip radar used in our work.

In the domain of SLAM for automotive systems using SoC radars, the authors in [72] exploit a setup of two radars giving planar coverage of approximately  $360^\circ$  and are mounted behind the vehicle bumpers. Both radars are used together with an IMU and wheel odometry to build resid-

uals within an optimization problem. Radar residuals are built matching detected landmarks to the stored map. Matching is done by brut-force association of the Hamming distances of landmarks descriptors. RANSAC is used on the matched landmarks to reject outliers. The approach allows for consistent localization error below 1 m over large-scale outdoor (parking lot) trajectories.

One of the best-performing RIO systems using SoC radars has been presented in [90]. As opposed to the methods in this thesis, the presented system is in fact a full SLAM relying on radar and an IMU sensors. Beyond the Doppler velocity, the presented approach uses distribution-to-multi-distribution distance concept to obtain matches between radar scans and submap. Both sources of information are fused within an iterated EKF to obtain the full 3D pose of the platform. The system also contains a loop closure component, effectively reducing the accumulated drift. Rather than using RANSAC as in majority of the aforementioned methods, the iterative reweighted least-squares are used to find the inlier set and consequently calculate the radar velocity. Scan-to-submap matching adopted by the authors ensures higher stability of matching by maintaining a local submap to which new scans are being registered. Sparsity of radar scans is countered within the update step partially by the distribution-to-distribution distance computation in the residual in which the local geometry of the matched point is considered. This is dictated by an assumption that due to the sparsity, of measurements, the points in the current scan will match exactly to the ones in the submap. The method is demonstrated on a small-sized UGV with a high-end automotive ARS548 radar mounted, and exhibits performances close to those of Fast-LIO SLAM [85]. An important observation is made in their work, namely that using the direct approach alone, that is, the Doppler velocity without scan matching is rendering radar-based estimators susceptible to vertical drift, thus evidencing the necessity of also incorporating point correspondences in the state estimation.

In [83] another RIO method is presented exploiting both Doppler velocity as well as point matching as delivered by a high-end automotive SoC radar. The implemented approach consists in ego-velocity computation, feature extraction and scan-to-submap matching. For ego-velocity estimation gaussian filtering is applied followed DBSCAN clustering of both static and dynamic objects. Clustered static objects are then used for ego-velocity estimation using least-squares. Feature extraction is done by dividing the points into voxels whose representative points are being calculated along with covariances. Calculating the Principal Component Analysis (PCA) for all voxels further permits pruning voxels with features having lesser stability. For matching, a sliding window of keyframes is constructed forming

a submap, which after aligning the current scan using the estimated ego-velocity, is used to register current scan based on voxels. The method is shown to perform on-par with vision and lidar-based methods.

In [16] the authors address the problem of state estimation of an UGV using RIO in highly dynamic scenes. Their method relies on the observation that the ground points are ever-present in the common UGV scenarios and can be reliably used for odometry estimation. Due to the instability and sparsity of radar scans the ground detection methods from lidar-based approaches will not work from radar. The authors thus propose an algorithm which jointly estimates radar velocity and detects ground points. Estimated velocity together with the angular velocity from IMU enables planar displacement calculation. On a self-collected dataset the presented method outperforms the methods from [90] (without mapping) and [23].

In [49] the authors present a radar-based SLAM based on pose graph optimization. The primary contribution of the authors is the design of a ego-velocity pre-integration factor and the integration thereof within their pose graph optimization framework. Besides the novel velocity pre-integration factor the authors use factors calculated based on NDT-based scan registration. Loop closure factor is also included to curb the accumulation of the drift. Interestingly, the authors do not use IMU in their implementation, relying only an a high-end ZF FRGen21 automotive 4D Radar.

As can be seen from the mentioned works, approaches to state estimation using radars usually use solely Doppler velocity or a combination of it with some form of scan matching. Interestingly, authors in [45] argue that when industry-grade sensors are used and only odometry is needed, scan matching is no longer needed and the Doppler measurements suffice. This statement is disputed in [38, 87, 90, 89] where the authors claim the vital importance of the point matching in their RIO system despite using automotive-grade radar. At any rate, still in many systems the price, weight and power consumption requirements mandate the use of consumer-grade radar chips as the one we use in the present paper where using point matches boosts estimation accuracy. What can also be seen is that depending on the system constraints, various SoC radar types can be used with broadly varying measurement accuracy and point cloud density. In this thesis we are interested in implementing RIO with only low-end consumer-grade radar which imposes more challenges on the state estimation as compared to systems using high-end SoC radars, yet given the limited weight, size and power consumption permits its use in small-size UAVs.

# CHAPTER 3

---

## The Fundamentals Of Millimeter-Wave FMCW Radar Sensing

This chapter aims at clarifying the sensing principles of millimeter-wave FMCW SoC radar sensors and at explaining the signal processing pipeline which leads from the raw radar data cube (see figure 3.3) to 3D point clouds and Doppler velocities. We begin by outlining the sensing mechanisms behind the millimeter-wave FMCW radar in section 3.1, how the radar data cube is formed and filtered against the noise to obtain radar targets. We also explain some radar terminology needed for understanding the following chapters. In section 3.2, we discuss the signal processing needed to extract higher level measurements such as 3D points and Doppler velocities from low-level radar data. Although the mechanically spinning radar sensors also use the FMCW technology, we limit the content of this chapter to the SoC radar sensors since this is the sensor used within this thesis.

### 3.1 Millimeter-Wave FMCW radar sensing

Millimeter-wave FMCW radar sensors transmit and receive electromagnetic waves of length between 1-10 mm and mostly within the frequency spectrum of 76-81 GHz. They operate at increased frequency spectrum with respect to the previous generation (increase from 25 GHz to above 60 GHz). This increase offers better performance of the sensors in terms of accuracy of measurements and also allows the chip size reduction at the expense of caus-

ing more scattering effects of the reflected waves [78]. FMCW means that the radar transmitter sends out a signal which is modulated in frequency by another signal. The modulating signal is linear in most of the robotic and automotive applications. A single linearly modulated electromagnetic pulse is called a *chirp*. A chirp gets reflected off objects in the environment (sometimes called *scatterers*) and comes back to the receiver. Chirps are characterized by the starting frequency  $f_c$ , duration time  $t_c$ , bandwidth  $B$  and slope  $S$  as shown in the figure 3.1. The reflected and emitted chirp signals are mixed to obtain the so-called *intermediate frequency* (intermediate frequency (IF)). While with IF originating from a single chirp it is possible to determine distances of reflecting objects, a radar typically sends multiple chirps during one cycle as shown in the figure 3.2. Multiple chirps are needed to measure the radial velocity of the reflecting objects using the Doppler shift. Moreover, it is also possible to determine the bearing and azimuth angles of the reflecting objects by properly laying out multiple antennas on the chip. Thus, raw data sensed by the FMCW radar can be thought of as the *radar data cube* as shown in figure 3.3. To form a point cloud from a radar data cube, a radar detector needs to be applied in order to find the reflecting targets within the range-Doppler maps among the background noise. Range-Doppler maps are obtained from the data cube using methods described in the section 3.2. Currently Constant False Alarm Rate (CFAR) (and its flavors [44, 84, 88]) is the most commonly used detector [68]. As input to CFAR the range-Doppler map is used which is the result of averaging all range-Doppler map values across the antennas dimension see figure 3.3).

The objective of CFAR is to identify the valid radar targets from the background noise using an automatically adjusting detection threshold. We briefly explain the basic idea behind CFAR using the CA-CFAR (Cell-Averaging CFAR) variant. Using radar data cube shown in the figure 3.3 we produce a range-Doppler map by applying the fast fourier transform (FFT) operations as explained in the section 3.2. Next, for every cell we average the cell values to produce a single range-Doppler map. Range-Doppler map entries are complex numbers, yet for CFAR we compute a square of the magnitude for each cell. Using a sliding window as shown in the figure 3.4, we estimate the background noise value by first computing the average of cells in the window excluding the Cell-Under-Test as well as the guard cells. Next, we compute the threshold as  $T = \alpha \tilde{P}$ , where  $\tilde{P}$  is the average value computed from the entries in the window, and  $\alpha$  is the threshold scaling factor calculated as  $\alpha = N_r (P_{fa}^{\frac{-1}{N_r}} - 1)$ , where  $N_r$  is the number of cells used for averaging and  $P_{fa}$  is the desired false alarm probability. The decision

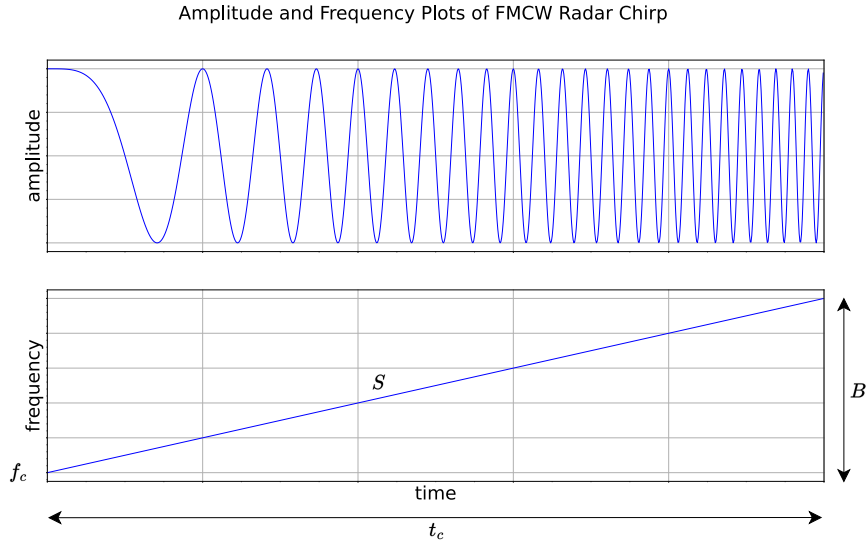


Figure 3.1: Single chirp generated by FMCW radar.

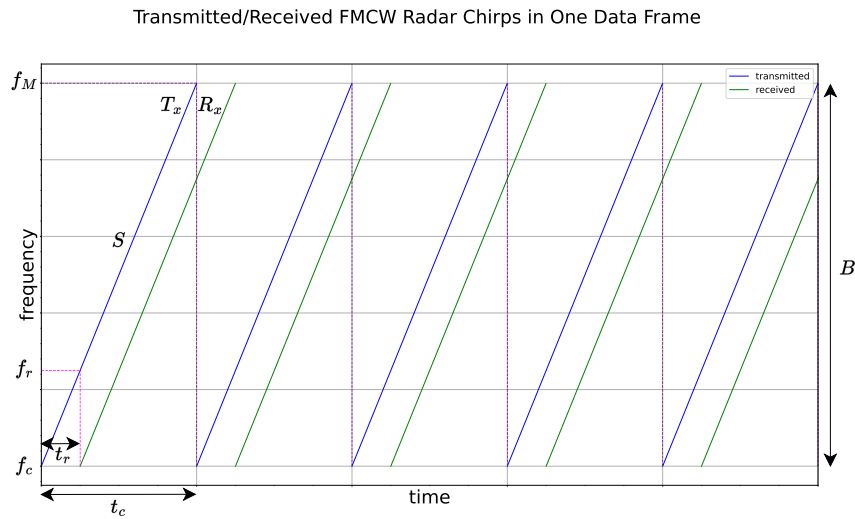


Figure 3.2: Within a single cycle multiple chirps are generated and sent out. Difference between  $f_r$  and  $f_c$  allows determining the  $t_r$  which is the time needed to travel back and forth between the transmitter and the reflected object. Using the phase difference between the chirps we can determine the Doppler velocity of the reflected objects.

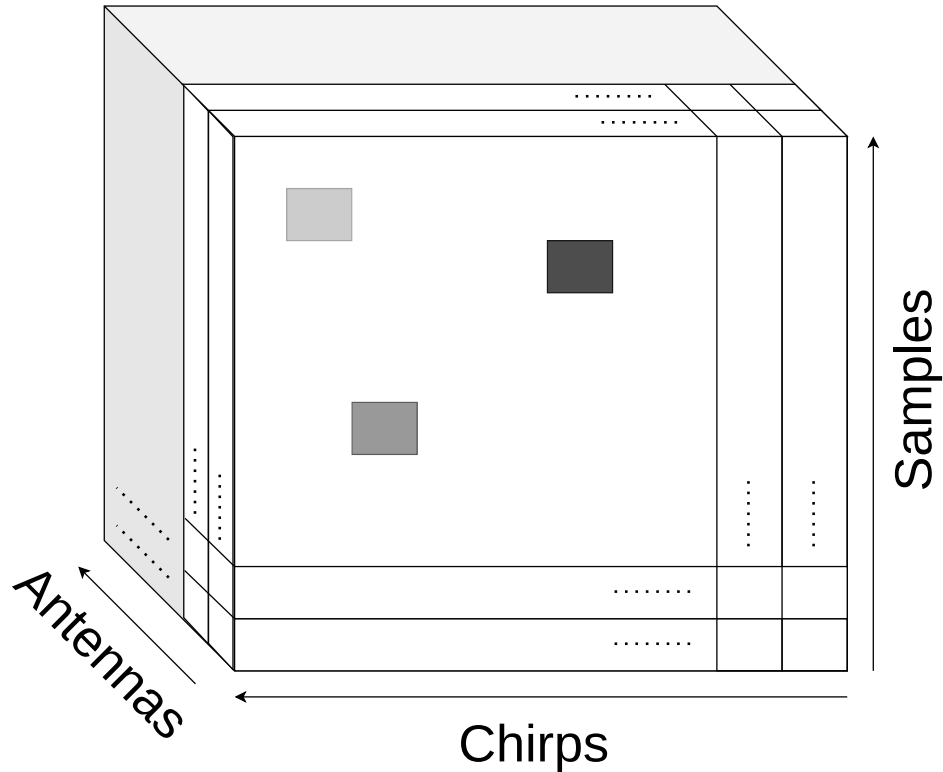


Figure 3.3: Measuring the reflections from multiple chirps at multiple receivers forms the radar data cube. The entries are complex samples of mixed chirps.

whether the Cell-Under-Test is a target is made by comparing its value to the calculated threshold  $T$ .

It is important to note that there exists evidence that CFAR is not very suitable for prevalent cluttered environments where autonomous systems operate nowadays and there is an active ongoing research into alternative methods for generating radar targets [17, 18].

By consecutively applying the FFT across each of the three dimensions of the radar cube shown in the figure 3.3 we can calculate distances, Doppler velocities and both bearing and azimuth angles, depending on the spatial layout of the antennas on the chip.

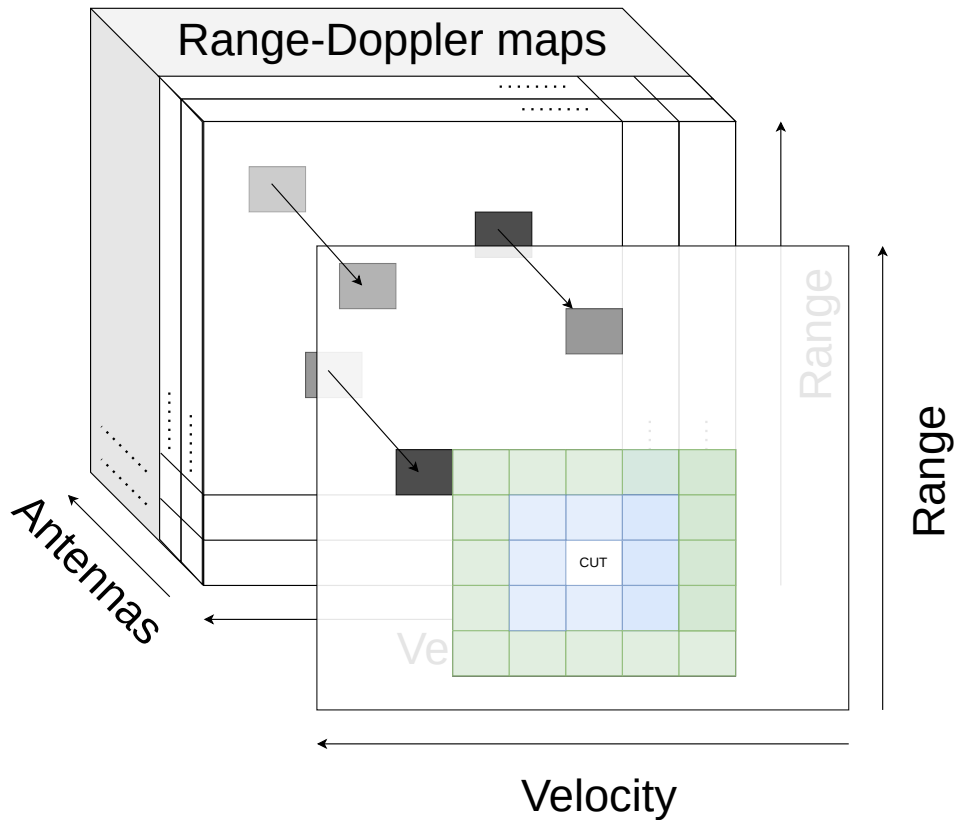


Figure 3.4: Target detection using CFAR proceeds by shifting a 2D window through the range-Doppler map built from averaged values from range-Doppler maps from all the antennas. Values in the green entries within the window are averaged and used to for the comparison threshold. Values in the blue entries are so called *guard cells* and do not participate in the threshold calculation. CUT stands for Cell-Under-Test.

## 3.2 FMCW Radar Signal Processing

Having in mind the sensing model outlined in the previous section we can now delineate the signal processing necessary to obtain the 4D radar point cloud, that is, a 3D point cloud and Doppler velocity associated with each point.

### 3.2.1 Range

In our setting, we use a millimeter wave FMCW radar emitting a linear chirp signal. In such a case, the range to a reflecting object can be determined from the mixed transmitter and receiver signals.

Linear chirp (as seen in the upper subplot in the figure 3.1) can be described in the time domain as (we omit the amplitude for clarity):

$$x(t) = e^{j(\pi St^2 + 2\pi f_c t + \theta)} \quad (3.1)$$

The instantaneous frequency is the time derivative of the argument (phase):

$$f(t) = \frac{d}{dt} \frac{1}{2\pi} (j(\pi St^2 + 2\pi f_c t + \theta)) = St + f_c \quad (3.2)$$

Where  $S = \frac{B}{T_c}$  is the chirp rate (see figure 3.1). Time delay  $t_r$  with which a reflected chirp comes back to the receiver creates a difference in frequency  $f_r$  which is called the *beat frequency* or *intermediate frequency*. Time delay  $t_r$  is proportional to the beat frequency as seen in the equation (3.2). We can see from the plot in the figure 3.2 that  $f_r = St_r = \frac{B}{T_c} t_r$ , which means that  $t_r = \frac{T_c}{B} f_r$  which is the time needed for the reflected chirp to travel to and from the reflecting object. We can also calculate the beat frequency as a result of complex mixing of signals:

$$x(t) = e^{j(\pi S(t-t_r)^2 + 2\pi f_c(t-t_r) + \theta)} e^{-j(\pi St^2 + 2\pi f_c t + \theta)} = e^{j(-2\pi S t_r t + \pi S t_r^2 - 2\pi f_c t_r)} \quad (3.3)$$

Since only the term containing  $t$  determines the frequency of the mixed signals we have that (we can ignore the minus sign since the distance is only positive)  $2\pi f_r = 2\pi S t_r$  and  $f_r = S t_r = \frac{B}{T_c} t_r$ . In order to determine the beat frequency we apply the FFT over the mixed signal and infer from it the time delay subsequently used for calculating the range:

$$d = \frac{f_r c_0}{2S} \quad (3.4)$$

Where  $c_0$  is the speed of light.

Two tones are distinguishable within the spectrum as long as their frequency difference is greater than the inverse of the chirp time ( $\Delta f > \frac{1}{t_c}$ ). The range resolution therefore, that is, the smallest range difference at which two radar targets are still distinguishable one from the other, depends only on the chirp bandwidth and is given by:

$$\Delta_r = \frac{c_0}{2B} \quad (3.5)$$

The maximum range is:

$$r_{max} = \frac{N_s c_0}{4B} \quad (3.6)$$

Where  $N_s$  is the number of samples in the range FFT.

Note that to resolve ranges only the real part of the FFT is necessary since what we need are the magnitudes of the spectrum over the frequency axis. Phase information is not needed.

### 3.2.2 Radial Velocity

In order to calculate the radial velocity of an object we can exploit the rate of change of the phase of chirps. Namely, assuming that the reflected object moved between two chirps with velocity  $v$ , the time delay will increase slightly to  $t_r = t_r + t_d$  where  $t_d$  comes from the objects velocity. Now using this new increased time delay in the equation (3.3) we can calculate the phase change of the object caused by  $t_d$ . Leaving out all negligible small terms we have that the phase change depends significantly only on the time delay caused by the motion of the object between two chirps:

$$\Delta\phi = 2\pi f_c t_d \quad (3.7)$$

Where  $t_d$  is the time delay of the chirp caused by the reflecting object traveling the distance  $d_d$  during one chirp, therefore:

$$\Delta\phi = 2\pi f_c \frac{2d_d}{c_0} = 4\pi \frac{d_d}{\lambda} = 2\pi \frac{2vt_c}{\lambda} \quad (3.8)$$

Where we substituted  $f = \frac{c_0}{\lambda}$ , it follows then that:

$$v = \frac{\lambda\Delta\phi}{4\pi t_c} \quad (3.9)$$

We can then calculate the velocity of objects by tracking the change of phase across chirps. Since the phase evolving in every range bin across all

chirps forms a complex sinusoid, by performing the FFT over range bins across the series of chirps, the relative radial velocity of the object can be retrieved. We call the result of such 2D FFT process a *range-Doppler* map.

The velocity resolution is given by:

$$\Delta_v = \frac{\lambda}{2N_c t_c} \quad (3.10)$$

Where  $N_c$  is the number of chirps within one frame. In words, the longer the frame time ( $t_f = N_c * t_c$ ) the better the velocity resolution.

### 3.2.3 Bearing Angle

When multiple receiver antennas are available, calculation of angular information of reflecting objects is possible. Due to the spatial separation of the receiver antennas, the measured signals at each receiving antenna will be shifted in time:

$$t_a = \frac{d \sin \theta}{c_0} \quad (3.11)$$

Where  $d$  is the separation distance between receiving antennas as seen in the figure 3.5. Exploiting once again the phase shift we can write:

$$\Delta\phi = 2\pi f_c \frac{d \sin \theta}{c_0} = 2\pi \frac{d}{\lambda} \sin \theta \approx 2\pi \frac{d}{\lambda} \theta \quad (3.12)$$

Now, measuring the phase shift using the FFT as in the case of velocities in the previous sub-section, but this time across all antennas we can retrieve the  $\theta$  angle. Based on the antennas geometrical arrangement on the chip, both azimuth and elevation angles of objects with respect to the radar can be determined using the principle outlined in this subsection. To determine the elevation angle there must be receivers placed vertically and for calculating the azimuth angle there must be receivers placed horizontally. The angular resolution of a FMCW radar is mostly limited by the number of receiver antennas on the chip. The greater the number of receivers on the chip, the greater the angular resolution. Nonetheless, every receiver entails a separate processing chain, which increases the chip size. Common solution to this problem is the Multiple-Input-Multiple-Output MIMO radar configuration, in which multiple transceivers are placed on the chip at known distances from each other, thus enabling the reception of phase-shifted signals. Temporal interleaving of transmitted signals leads to *multiplicative* creation of the *virtual* antennas increasing the angular resolution, as in:

$$N_a = N_r \times N_t \quad (3.13)$$

Where  $N_a$  is the number of antennas,  $N_t$  number of transceivers, and  $N_r$  number of receivers.

Although FMCW radars are thus capable of providing a 3D position of a reflecting object along with its relative Doppler velocity, the distance to the object and its relative Doppler velocity are the most precise parts of the information in small, light, and cost-efficient FMCW radars.

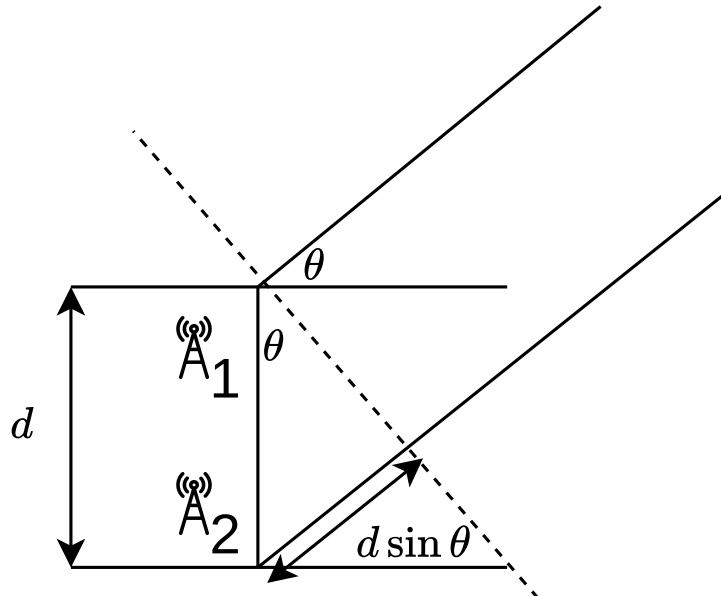


Figure 3.5: Multiple antennas on the chip allows for angle resolution using FMCW radar. The dashed line represents the front of the reflected wave arriving at the two antennas.

Note that the presence of the sine function in the formula makes the relationship between the phase shift and the angle nonlinear, that is to say, that for larger angles the small angle approximation  $\theta \approx \sin \theta$  does not hold anymore.

The angular resolution is:

$$\Delta\theta = \frac{\lambda}{N_a d \cos \theta} \quad (3.14)$$

### 3.2.4 Radar Cross Section

An important notion in radar engineering is that of the RCS. RCS can be defined as a property of an object illuminated by the electromagnetic waves emitted by radar, and quantifying a fictitious area describing its reflectivity back at the radar receiver [76]. For simple objects such as a sphere the RCS can be found analytically, while for more complex objects its value must be determined experimentally. The RCS is defined as:

$$\sigma = 4\pi \lim_{R \rightarrow \infty} R^2 \frac{|E_s|^2}{|E_i|^2} \quad (3.15)$$

Where  $R$  is the distance to the reflecting object, and  $E_s$ ,  $E_i$  are the backscattered, and incident electric fields, respectively. In practice, often what is used to estimate the RCS is the so-called radar equation [73]:

$$\frac{P_R}{P_E} = \frac{c G_E G_R \sigma}{(4\pi)^2 R^4} \quad (3.16)$$

Where  $P_R$  and  $P_E$  are the received and transmitted signals power,  $G_R$  and  $G_E$  are the receiver and transmitter gains,  $c$  is a constant coefficient and  $R$  is the distance to the reflected object.

## 3.3 Summary

In this chapter, we outlined the sensing principles behind millimeter-wave FMCW SoC radars. We explained how the signal processing pipeline based on the successive application of the FFT allows for calculating the range, azimuth and elevation angles as well as the radial velocity which enables the construction of the 4D point clouds (3D points and Doppler velocity of each 3D point). We also defined the RCS as a kind of *visibility* of an object to the radar.

# CHAPTER 4

---

## Radar-Inertial Odometry Using The Extended Kalman Filter

*The present chapter contains results that were peer-reviewed and published in the International Conference on Unmanned Aerial Systems (ICUAS) [56], IEEE/RSJ International Conference on Intelligent Robots and Systems (IROS) [54], IEEE International Conference on Robotics and Automation (ICRA) [53] and the IEEE International Symposium on Safety, Security, and Rescue Robotics (SSRR) [55]*

This chapter introduces three different approaches to estimating the navigation states of an UAV using the IMU and the FMCW radar, all based on the EKF algorithm. In section 4.1 we introduce the first method which, although constrained to the usage of fixed anchors, allowed us to confirm the purposefulness of using the distance measurements from an FMCW radar within the EKF update step. In section 4.2 we expand on the previous approach by introducing the data association between the current and the previous set of the detected 3D points which generalizes the method to unknown environments. Moreover, we formulate the EKF update step so as to additionally include the Doppler velocity besides the distance measurements. In section 4.3 we present the final expansion of the EKF-based RIO which includes persistent features, trails of measurements and past UAV poses as well as self-calibration capabilities. We also show how the final EKF RIO implementation performs in closed-loop flights and in the simulated fog environment. In all our EKF formulations we choose the tightly-coupled fusion which means we do not pre-process the radar measurements before fusing them in the EKF but rather feed them in the estimator as they come delivered by the sensor.

## 4.1 EKF RIO using distance measurements to fixed anchors

In this section, we present a preliminary RIO method which uses a tightly-coupled EKF formulation in which we fuse measurements from an IMU with radar range measurements of known targets in the environment. This approach enables fast and accurate provision of the UAV state estimate even in scenarios where VIO suffers from both low rate (relative to the trajectory agility) correction information and image blur adversely affecting the state estimates. Also, a tightly-coupled formulation allows for state updates having sparse measurements, that is, contrarily to loosely-coupled formulations, ours does not require a prior 3D triangulation step for which distances to at least three features must be measured simultaneously. The method developed in this section can be considered a proof-of-concept for approaches shown later in the chapter (section 4.2 and section 4.3). The work outlined in this section contributes a method for fast and accurate state estimation suitable for a rapidly moving UAV using a single small, lightweight, and low-cost FMCW radar measuring ranges to so-called *corner reflectors* [27] in the environment and an IMU sensor. The approach uses reflectors at known positions and self-calibrates system extrinsics, IMU extrinsics, and estimates the 6DoF pose with 3D velocity. We show that with this method we can outperform VIO when sharp and aggressive motions are executed. Moreover, the presented approach can be used in environmental conditions completely prohibitive for VIO like fog or lack of light. We evaluate our approach experimentally and compare against the state-of-the-art VIO algorithm in [32], using the platform shown in Fig. 4.2.

### 4.1.1 Methodology

#### System Overview

We consider our approach a tightly-coupled one since we use the one-dimensional distance measurement from the onboard radar sensor to a radar target as information for IMU integration correction. We do not pre-process several distance measurements from several target to triangulate first a 3D position to only then use this result as position correction. Compared to the pre-triangulation method, our tightly coupled approach has several advantages: first, a quick non-linear observability analysis shows that all motion states including IMU biases are locally observable if the system is excited in acceleration and angular velocity while observing only one target (intuition to this fact can be gained from [51]). Thus, the radar does not

need to observe all targets at once like in the triangulation pre-processing approach. Note that, at least sequentially, it needs to observe at least two different targets to eliminate any gauge freedom. Second, omitting the pre-processing step from the distance measurement to a 3D position measurement reduces the distortion of the noise characteristics that may otherwise impact the EKF assumptions on Gaussian distributions. Third, we can process measurements as they arrive and do not need any sort of synchronization between the targets. Fourth, the only geometric condition to avoid singularities (in this case to eliminate the gauge freedom in 3D position and yaw) is that at least two targets have different positions in a direction perpendicular to gravity (i.e. in the xy-plane).

Our estimator setup is such that at least two of the targets need to be placed at known location to eliminate said gauge freedom (3D position and yaw), positions of additional targets can seamlessly be integrated in the estimation process. For the initialization of additional targets online, the approach in [8] could be adapted to use initial distance measurements from a newly observed target. That said, in this paper we only focus on the radar-inertial estimation of the motion states as proof-of-concept.

The targets generate a clear signal in the radar receiver. We perform an FFT to extract the distances to each target and then use this information in the EKF framework. The data association is done by matching the measured range closest to the expected range calculated from the current vehicle pose and a given target location. The following sections detail each step further.

## Radar Signal Processing

The radar sensor used to validate the approach presented in this section can be seen in the figure 4.2. This miniature SoC FMCW radar delivers raw signal in the form of the mixture of sinusoids for each chirp. Therefore, in order to retrieve the distance measurements to be used in the EKF an amount of signal pre-processing must be done according to the principles outlined in the chapter 3. As the method described in this section makes use of the radar delivering the raw data (as opposed to the radar sensor we use later on in section 4.2 and section 4.3), the pre-processing also includes convolving the receiver signal with a Hamming window to minimize spectral leakage. Very low and high frequency contributions which are not in the region of interest are filtered out using a bandpass filter. The bandpass filter was designed with cut-off frequencies mapped to ranges  $r_{c,L} = 0.1$  m and  $r_{c,H} = 1.7$  m to suppress frequency peaks caused by noise and multipath reflections taking into account the approximate flight altitude range. After

filtering, the signal is thresholded above an experimentally obtained value of  $c_{\text{noise}} = 0.15$  and the resulting signal is searched for clusters. The frequency value corresponding to the maximum value of each cluster is returned and mapped to a range value (figure 4.1).

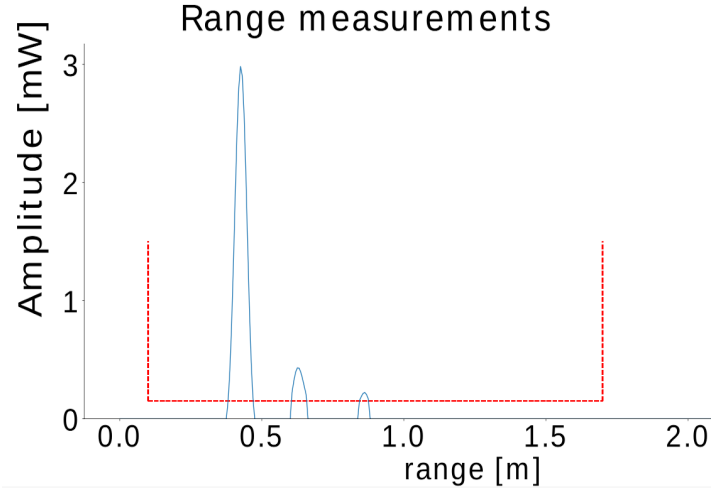


Figure 4.1: Range-amplitude plot after performing FFT of the radar raw signal. The dashed red lines depict thresholds assumed for cropping the radar signal in frequency (mapped to range) and for application of the threshold above which targets are identified.

### Data association

With the output of the processing module, we obtained range values of all targets in the field of view of the radar sensor. Compared to obtaining Doppler velocity information or angular information, the range values only need a single FFT pass for calculation. This enables very fast measurements and subsequent propagation correction in the estimator framework. However, this lightweight data processing comes at the difficulty of data association. Each identified peak (i.e. measurement) in the range-amplitude plot (figure 4.1) needs to be associated with a target in the world to derive the necessary correction in the EKF formulation. For this association, we first compute estimates of the ranges between the current vehicle position and the targets from the information we have at the current time step. Then, a greedy search is minimizing the error of a given measurement with the computed possible range estimates. If the previous radar scan already had a similar range measurement, this information is included as a prior.

Since the radar scans are very fast compared to the vehicle motion, this element helps speeding up the data association process. The matched range measurement with a target forms then an update information pair for the EKF. If a range measurement differs more than 3 cm to any possible target range, then the measurement is discarded.

### Tightly coupled Extended Kalman Filter formulation

The EKF framework uses an IMU for the propagation of the state formulation defined by Eq. (4.1). The states are the position of the IMU/body frame  ${}^G\mathbf{p}_I$  and velocity  ${}^G\mathbf{v}_I$  expressed with respect to the world frame, the orientation of the IMU in the world frame  ${}^G\bar{\mathbf{q}}_I$ , gyroscopic bias  $\mathbf{b}_\omega$  and accelerometer bias  $\mathbf{b}_a$ . The 3D translation between the onboard radar sensor and the IMU is expressed as the calibration state  ${}^I\mathbf{p}_R$  in the IMU frame.  ${}^G\mathbf{p}_A^i$  represents the  $i$ -th corner reflector (i.e. radar target) 3D position in the world frame with  $i = 1, 2, \dots, K$ . Note that at least two such targets need to be known and fixed to eliminate the gauge freedom. The full state vector  $\mathbf{x}$  is then defined as follows:

$$\begin{aligned} \mathbf{x} &= [\mathbf{x}_{\mathcal{N}}; \mathbf{x}_{\mathcal{A}}] \\ &= [[{}^G\mathbf{p}_I; {}^G\bar{\mathbf{q}}_I; {}^G\mathbf{v}_I; \mathbf{b}_a; \mathbf{b}_\omega; {}^I\mathbf{p}_R]; [{}^G\mathbf{p}_A^1; {}^G\mathbf{p}_A^2; \dots; {}^G\mathbf{p}_A^K]] \end{aligned} \quad (4.1)$$

The system dynamics of the core states are defined according to [80]. The dynamics and process noise of the calibration state  ${}^I\mathbf{p}_R$  are assumed to be zero because of the rigid body assumption. In our setup,  ${}^G\mathbf{p}_A^i$  are kept fix as known values. The EKF framework uses a regular error-state (including error quaternion) definition. We use the Hamilton notation for the quaternion representation [75].

An estimated range measurement  $\hat{z}^i$  from the radar sensor to a target  $i$  and the corresponding error using the true measurement  $z^i$  from the data association process can then be defined as

$$\hat{z}^i = \|{}^G\mathbf{p}_A^i - ({}^G\mathbf{p}_I + R\{{}^G\bar{\mathbf{q}}_I\}{}^I\mathbf{p}_R)\| \quad (4.2)$$

$$\tilde{z}^i = z^i - \hat{z}^i \quad (4.3)$$

Where  $R\{{}^G\bar{\mathbf{q}}_I\}$  rotates a vector from the IMU frame to the world frame using the quaternion  ${}^G\bar{\mathbf{q}}_I$ . This renders the update step very efficient for any number of currently visible targets by the radar sensor. With a standard computer, we achieve an update rate of about 90 Hz in our setup described below.

### 4.1.2 Experiments

The above described method enables a simple, yet computationally very efficient radar-inertial state estimation with self-calibration capabilities (IMU intrinsics, radar-IMU extrinsics). In the following, we test our method on real platforms with real data.

#### Experimental setup

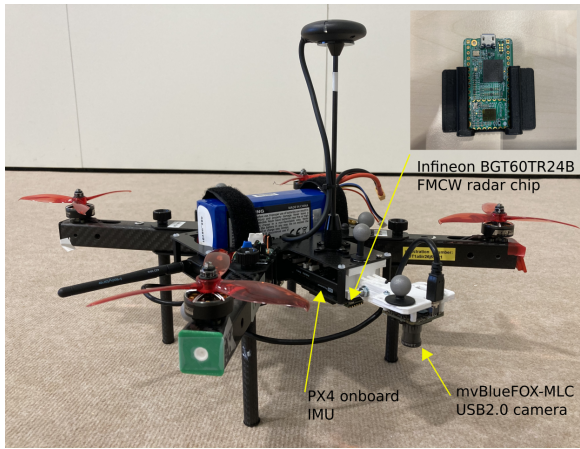


Figure 4.2: Experimental platform used in this work and the FMCW radar sensor mounted in its custom-made housing.



Figure 4.3: Corner reflectors used in our experiments.

The sensor used for the experiments is the lightweight 60 GHz multi-channel FMCW radar transceiver BGT60TR24B from Infineon, shown attached to the UAV in figure 4.2, mounted on the Infineon XMC4500 board

equipped with a USB interface. The frequency spectrum of chirps generated by the radar is between  $f_l = 57$  GHz and  $f_u = 63$  GHz. We set the sampling frequency to  $f_{sr} = 2$  kHz, the number of samples to  $N_s = 200$  and the number of chirps to  $N_c = 20$ . For inertial measurements we use the IMU supplied on the PX4 platform. We set the sampling rate of the IMU to  $f_{si} = 200$  Hz. For comparison with VIO, we use images grabbed by the onboard mvBlueFOX-MLC camera connected over USB. We set the frequency of the camera to  $f_{sc} = 20$  Hz which is a reasonable choice from the potential on-board processing viewpoint. Although VIO can benefit from the stereo-camera setup, we do not make use of it because of the limited payload of the UAV. We set the camera exposure time to  $e = 8$  ms for a typical indoor scene.

We placed three corner reflectors (figure 4.3) as radar targets at the locations  $A_1 = [x = 0.23, y = 0.65, z = 0.36]$  m,  $A_2 = [x = 0.52, y = 0.53, z = 0.48]$  m and  $A_3 = [x = 0.48, y = 0.86, z = 0.59]$  m.

We then acquired two datasets performing highly aggressive hand-held trajectories with the platform in figure 4.2. Each acquisition involved very sharp and aggressive movements (norm of max. angular velocity  $\omega = 12.6 \frac{\text{rad}}{\text{s}}$ , norm of max. linear acceleration  $a = 33.0 \frac{\text{m}}{\text{s}^2}$ ) of the sensor rig such that high motion blur was affecting the camera sensor. Fig. 4.4 depicts the setup from the onboard camera view with motion blur above the well textured area (left) and a sharp image on the low textured area (right). The trajectories were carried out just above the set of three corner reflectors (figure 4.5) allowing the same (visual) feature set to be visible during the entire experiment and thus allowing the VIO to leverage persistent features for locally non-drifting estimation. A sample range-Doppler reading by the radar of such a scene is depicted in figure 4.6. The two acquired datasets are recorded with feature-poor and feature-rich backgrounds in order to see the effect the background has on the VIO performance.

During acquisition, we recorded sensor readings from the camera, IMU, and radar together with the poses of the UAV and corner reflectors streamed by the motion capture system for the ground truthing. Both estimators, our EKF-based radar-inertial state estimator and OpenVins [32] as the state-of-the-art reference VIO are run offline on the recorded sensor data on an Intel core i7 vPRO laptop with 15 GB RAM. For a fair comparison of the proposed methodology with the VIO, we carefully fine tuned the feature tracker (incl. persistent features) of OpenVins to get the best possible result out of the VIO algorithm given the high aggressiveness of the performed movements and the challenging amount of motion blur contained in the camera images.

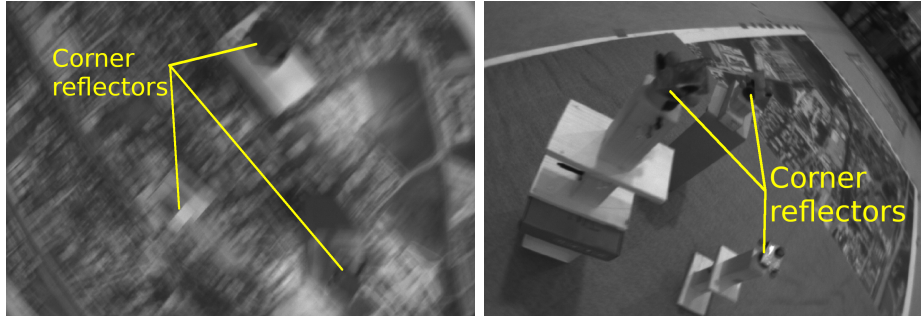


Figure 4.4: Radar target setup shown from the onboard camera view. Left: above well textured area during a high-speed motion causing significant motion blur. Right: still phase above low textured area.

Ground truth trajectory of the UAV and corner reflectors

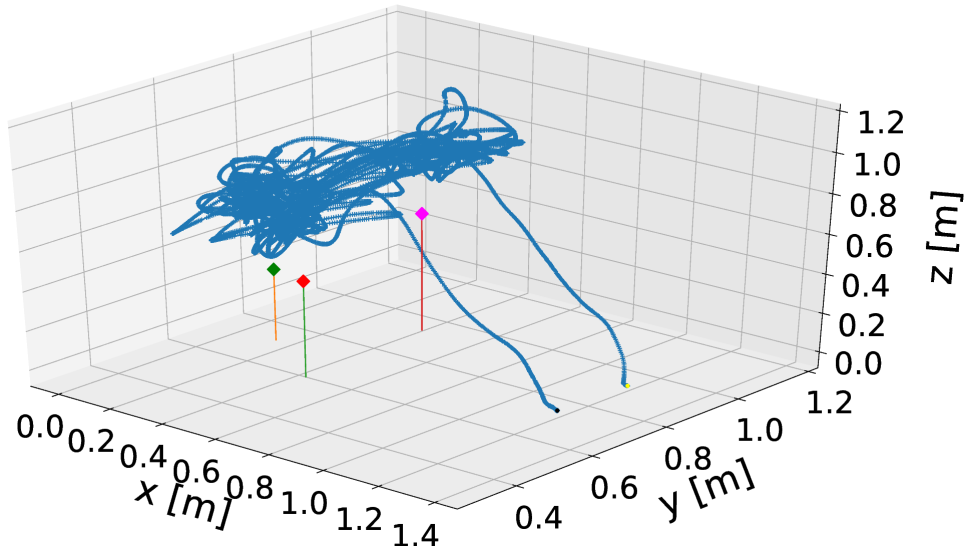


Figure 4.5: Ground truth trajectory of the UAV above the set of three corner reflectors. Trajectory of the UAV is plotted in blue, green, magenta and red diamonds are the corner reflectors placed on the floor, the black and yellow dots are final and initial UAV positions respectively.

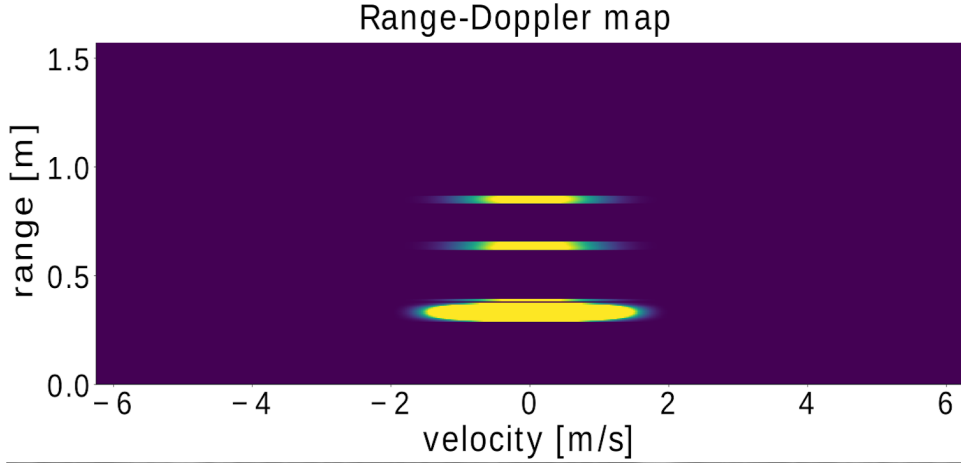


Figure 4.6: Range-Doppler map generated from a typical scene as shown e.g. in figure 4.4 from the three corner reflectors. The ellipses in the velocity dimension are fairly wide which reflects high uncertainty of the Doppler velocity measurement. Thus, and because of the lighter computation, we only use range measurements in our approach.

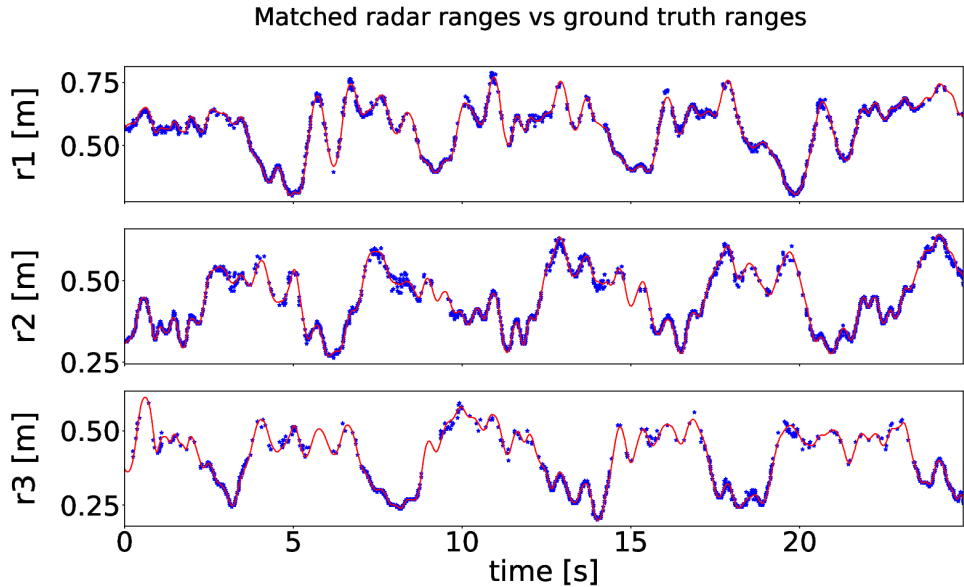


Figure 4.7: Ranges measured with radar matched to the ground truth. Ground truth is plotted in red, matched radar range in blue.

## Evaluation

Firstly, we evaluate if our proposed data association yields adequate results to be used as update information in our EKF estimator framework. For

this, we compare the measured ranges using the approach described in section 4.1.1 to the ground truth range computed from the motion capture measurements of the radar sensor and the corresponding target 3D position. Fig. 4.7 depicts in red the ground truth ranges during a 25 seconds long test and shows in blue the measurements obtained with our method. Note that often, our approach could not clearly associate the measured ranges to a target (gaps between the blue stars). This is due to the noise in the radar reading and our gating approach such that any measurement differing more than 3 cm to any possible target range is directly discarded (see section 4.1.1). That said, our tightly coupled estimator approach is resilient to intermittent target losses as any available measurement is seamlessly used as 1D measurement whenever available. Fig. 4.7 shows this particularly well around  $t=15$  s where only the first target yields measurements. From this data we measured a standard deviation of  $\sigma_m = 1$  cm for the measurements. This noise value was included in the EKF process.

As figure 4.6 shows, Doppler velocity could additionally be extracted from the radar signal. However, it significantly increased computational load for its calculation, as it requires to compute the FFT across all ranges for each chirp, and the fact that velocity is already observable with only range measurements are all factors that do not motivate to use the Doppler velocity as measurement. With our implementation we achieve an average range measurement rate of about 90 Hz.

Secondly, we test the estimator performance when the extracted ranges are fused together with IMU in an EKF framework. We compare this radar-inertial estimation with visual-inertial odometry for highly aggressive maneuvers. Fig. 4.8 and figure 4.9 show the absolute position error plots for our approach (red) and VIO (green) compared to the Optitrack ground truth in well-textured and poorly-textured scenes respectively. With the well tuned VIO, we managed to achieve non-diverging results for the VIO algorithm in both cases. A non-negligible drift (final error divided by overall path length), however, persists for both cases: about 13 % for the well-textured scene, and nearly 20 % for the poorly-textured one (see table 4.1 for details). Fig. 4.10 shows a similar plot for the attitude error in the well-textured test. The unobservable yaw is most affected by the challenging data since the persistent features are lost due to the motion blur. We encourage to not take the figures and table 4.1 as direct comparisons between the two algorithms since this would compare unobservable states in VIO against observable ones in our approach. Rather, they show the behavior of the approaches in challenging situations: for VIO they show an order of magnitude higher drift than usually reported in literature discussing well-behaving scenarios despite dataset specific tuning of the VIO

Table 4.1: Experiments and RMSE after convergence

	pos [m]	roll [°]	pitch [°]	yaw [°]	drift [%]
well textured scene					
Ours	0.0268	0.7861	1.3476	1.2105	7.0985
VIO	0.0894	0.9272	0.6389	3.7205	13.2782
poorly textured scene					
Ours	0.0311	1.1901	1.3047	1.4743	5.1859
VIO	0.2183	1.1429	0.7438	8.9878	19.9222

algorithm. The increase in drift is caused by the VIO not being able to consistently keep the persistent features because the high motion blur. With the lack of their locally non-drifting information, the algorithm thus goes back to the mode in which only odometry information can be used. For our approach, the figures show an root mean square error (RMSE) below 3 cm in position despite the very agile motion and only using sequential 1D range measurements for IMU integration correction.

Third, we evaluated the self-calibration capability of the proposed estimator. Fig. 4.11 shows the evolution of the extrinsic calibration state  ${}^I\mathbf{p}_R$  representing the 3D translation between the onboard IMU and radar sensor. After a wrong initialization, the state converges well.

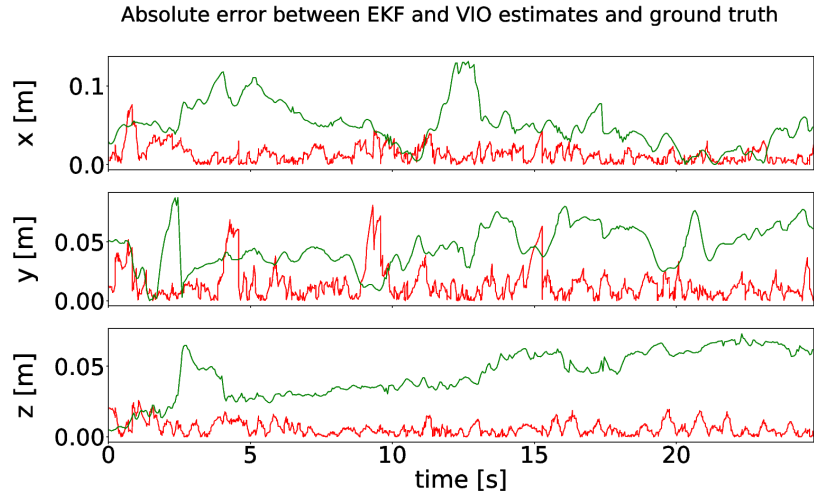


Figure 4.8: Absolute position estimation error for feature-rich scenario. Errors for VIO are plotted in green, for our radar based approach in red. The position drift of the VIO is more than 13 % showing the impact of the challenging data.

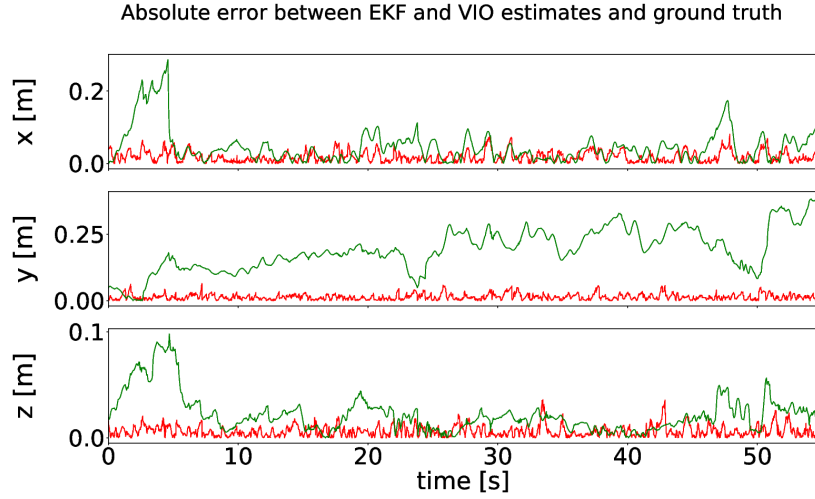


Figure 4.9: Absolute position estimation error for feature-poor scenario. Errors for VIO are plotted in green, for our radar based approach in red. With our best tuning efforts, we managed to get non-diverging results and a position drift of about 20 % for VIO.

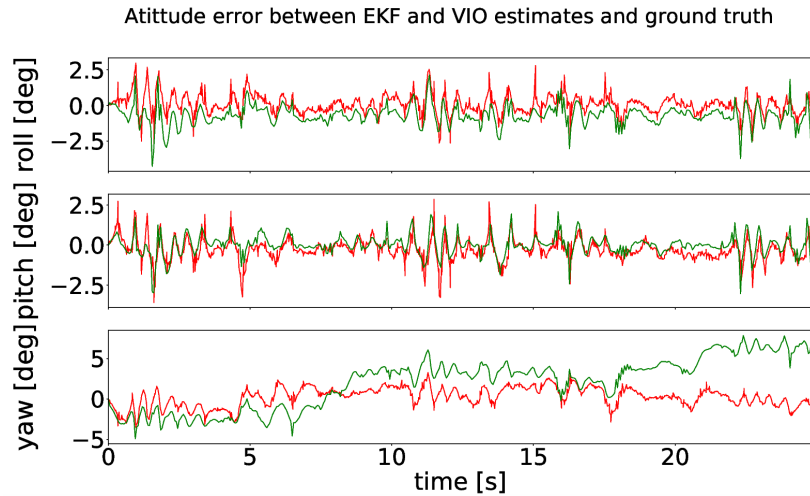


Figure 4.10: Attitude estimation error for the feature-rich scenario. Errors for VIO are plotted in green, for our radar based approach in red. The challenging motion clearly affects the (unobservable) yaw drift of the VIO.

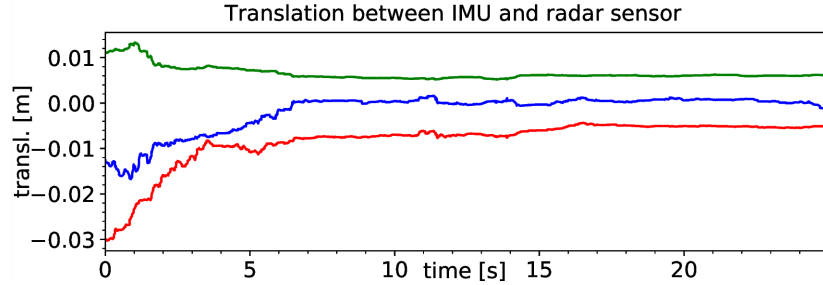


Figure 4.11: Estimated translation  ${}^I\mathbf{p}_R$  between radar and IMU sensors for one of the experiments (feature-rich scenario). x, y and z coordinates are plotted in red, green and blue respectively.

### 4.1.3 Conclusions

In this section, we presented a method which uses a tightly-coupled formulation of an Extended Kalman Filter in which we fuse measurements from an IMU with range measurements from a low-cost and lightweight FMCW radar. We presented a data association method to match targets in the environment with the signals in a radar scan. To eliminate any gauge freedom, we fixed at least two targets defining the gravity aligned world frame and can seamlessly include additional target positions due to the tightly coupled estimator formulation. We showed that this approach enables fast and accurate estimation of the UAV pose even in scenarios where VIO suffers from the image blur adversely affecting its accuracy (despite using persistent features for locally non-drifting information). Our computationally simple approach only extracting range information from the raw radar signals and use them as sequential 1D measurements in an EKF formulation enabled estimator update rates of about 90 Hz. Our EKF formulation is capable of estimating the navigation states, IMU intrinsics, and radar sensor extrinsics. The fast and motion-blur free measurements are particularly relevant for UAVs performing aggressive manoeuvres. As the next steps, moving from this rather area-bound proof-of-concept presented here, we wish to integrate radar sensors with longer range and different measurement profile which will allow us to detect features in the environment and match them between consecutive scans.

## 4.2 RIO EKF using distance and Doppler velocity measurements of 3D points

As shown in the previous section, the FMCW SoC radar can be successfully used to correct the IMU drift within an EKF. Bearing in mind this conclusion, in this section, we show a RIO method which employs a different radar sensor model and is more flexible in that it does not require any prior knowledge of the environment (like reflective anchors positions in the previous chapter). Thus, in this section we present a novel RIO method which employs stochastic cloning [70] to enable matching of the measured 3D points from the previous radar scan to the ones in the current scan. In addition to these relative distance measurements of matched 3D points, we also use Doppler velocity information measured from all features in the current scan. We fuse all measurements in a tightly-coupled formulation in our EKF setup. The tight coupling enables the incorporation of single distance and velocity measurements in the update step. This property relieves us from any constraints on required minimal number of matches (as it is e.g., needed for a prior iterative closest point (ICP) and subsequent loose coupling of the resulting delta-pose in the EKF). This is a particularly strong advantage in view of robustness and accuracy over loosely coupled approaches since, e.g., ICP [7] works poorly on noisy and sparse FMCW radar point clouds. Our RIO method makes no assumptions on the environment and makes use of no other sensors than IMU and a lightweight millimeter-wave FMCW radar.

### 4.2.1 System Overview

In our RIO method we use error-state EKF formulation [52] in which IMU is a core sensor used for the system state propagation. Updates are performed with the FMCW radar measurements, which provide both position and relative radial velocity of reflecting objects. Every time a radar measurement is taken, we augment the state of our EKF estimator with the pose of the robot at which the measurement took place using stochastic cloning. Once a subsequent radar measurement is taken, we use the stored pose together with the current one in order to spatially align the radar scans and match the corresponding points across them. Distances to matches are used to form the residual vector in the EKF. Next, we use projections of the current robot velocity onto normal vectors to all points detected in the current radar scan together with their measured velocities to further augment the residual vector. Residual vectors are then used in the update step

to estimate the mean of the error-state, which is injected into the regular state. The coordinate frames arrangement for measurements in our system is shown in figure 4.12.

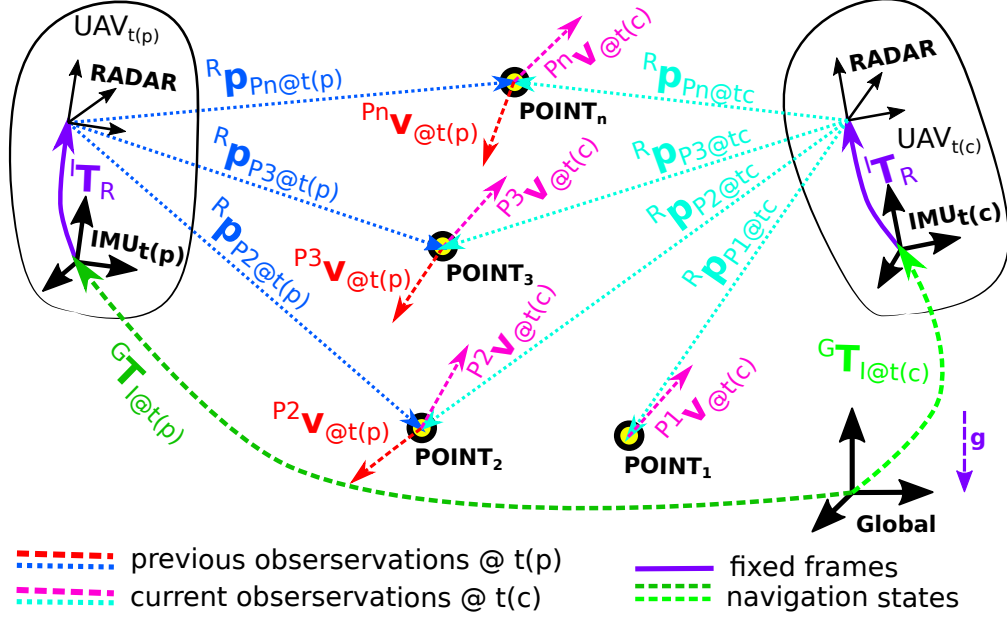


Figure 4.12: Two subsequent UAV poses are used in the distance and velocity measurement models. In the velocity measurement model, only the readings from the current pose are used.

### 4.2.2 Radar-Inertial State Estimation

The state vector  $\mathbf{x}$  in our filter is defined as follows:

$$\begin{aligned} \mathbf{x} &= [\mathbf{x}_N; \mathbf{x}_C] \\ &= [[{}^G\mathbf{p}_I; {}^G\bar{\mathbf{q}}_I; {}^G\mathbf{v}_I; \mathbf{b}_a; \mathbf{b}_\omega]; [{}^G\mathbf{p}_{I_1}; {}^G\bar{\mathbf{q}}_{I_1}]] \end{aligned} \quad (4.4)$$

with the navigation state  $\mathbf{x}_N$  and the stochastic clone state  $\mathbf{x}_C$  of the IMU pose corresponding to the previous radar measurement as described later on in this section. The previous radar measurement is not part of the state vector.  ${}^G\mathbf{p}_I$ ,  ${}^G\mathbf{v}_I$ , and  ${}^G\bar{\mathbf{q}}_I$  are the position, velocity, and orientation of the IMU/body frame  $\{I\}$  with respect to the navigation frame  $\{G\}$ , respectively.  $\mathbf{b}_\omega$  and  $\mathbf{b}_a$  are the measurement biases of the gyroscope and accelerometer, respectively.  ${}^G\mathbf{p}_{I_1}$  and  ${}^G\bar{\mathbf{q}}_{I_1}$  define the pose of the IMU

frame  $\{I_1\}$  corresponding to the last radar measurement with respect to the navigation frame  $\{G\}$ . We will use this frame later on in this section for ad-hoc point correspondence generation such that we do not need to keep 3D points in the state vector in order to use distance based measurements.

The evolution of the state is expressed by the following differential equations:

$$\begin{aligned} {}^G\dot{\mathbf{p}}_I &= {}^G\mathbf{v}_I, \\ {}^G\dot{\mathbf{v}}_I &= {}^G\mathbf{R}_I ({}_I\mathbf{a}^\# - \mathbf{b}_a - \mathbf{n}_a) + {}^G\mathbf{g}, \\ {}^G\dot{\mathbf{R}}_I &= {}^G\mathbf{R}_I [{}_I\boldsymbol{\omega}^\# - \mathbf{b}_\omega - \mathbf{n}_\omega], \\ \dot{\mathbf{b}}_a &= \mathbf{n}_{ba}, \dot{\mathbf{b}}_\omega = \mathbf{n}_{b_\omega}, {}^G\dot{\mathbf{p}}_R = \mathbf{0}, {}^G\dot{\mathbf{R}}_R = \mathbf{0} \end{aligned} \quad (4.5)$$

where  ${}_I\mathbf{a}^\#$  and  ${}_I\boldsymbol{\omega}^\#$  are the accelerometer and gyroscope measurements of the IMU with a white measurement noise  $\mathbf{n}_a$  and  $\mathbf{n}_\omega$ .  $\mathbf{n}_{ba}$  and  $\mathbf{n}_{b_\omega}$  are assumed to be white Gaussian noise to model the bias change over time as a random process. The gravity vector is assumed to be aligned with the z-axis of the navigation frame  ${}^G\mathbf{g} = [0, 0, 9.81]^\top$ .

Since we use an error-state EKF formulation we introduce the following error state vector from the states defined in equation (4.4):

$$\begin{aligned} \tilde{\mathbf{x}} &= [\tilde{\mathbf{x}}_N; \tilde{\mathbf{x}}_C] \\ &= [[{}^G\tilde{\mathbf{p}}_I; {}^G\tilde{\boldsymbol{\theta}}_I; {}^G\tilde{\mathbf{v}}_I; \tilde{\mathbf{b}}_a; \tilde{\mathbf{b}}_\omega]; [{}^G\tilde{\mathbf{p}}_{I_1}; {}^G\tilde{\boldsymbol{\theta}}_{I_1}]]. \end{aligned} \quad (4.6)$$

For translational components, e.g., the position, the error is defined as  ${}^G\tilde{\mathbf{p}}_I = {}^G\hat{\mathbf{p}}_I - {}^G\mathbf{p}_I$ , while for rotations/quaternions it is defined as  $\tilde{\mathbf{q}} = \hat{\mathbf{q}}^{-1} \otimes \bar{\mathbf{q}} = [1; \frac{1}{2}\tilde{\boldsymbol{\theta}}]$ , with  $\otimes$  and  $\tilde{\boldsymbol{\theta}}$  being quaternion product and small angle approximation, respectively.

### Stochastic Cloning

In order to process relative measurements relating to estimates at different time instances, Roumeliotis and Burdick introduce the concept of Stochastic Cloning (SC) in [70]. To appropriately consider the correlations/interdependencies between the estimates from different time instances, an identical copy of the required states and their uncertainties is used to augment the state vector and the corresponding error-state covariance matrix. Given the error-state definition in equation (4.6),  $\tilde{\mathbf{x}}_C$  is defined as the error state of the stochastic clone of the IMU pose state  $\mathbf{x}_I = [{}^G\mathbf{p}_{I_1}; {}^G\mathbf{q}_{I_1}]$  and  $\mathbf{x}_O = [{}^G\mathbf{v}_I; \mathbf{b}_a; \mathbf{b}_\omega]$  are the other states of the navigation state. As cloned state is fully correlated with the IMU pose, it leads to the following stacked/augmented covariance matrix of the corresponding error-state:

$$\tilde{\mathbf{x}} = \begin{bmatrix} \tilde{\mathbf{x}}_{\mathcal{I}} \\ \tilde{\mathbf{x}}_{\mathcal{O}} \\ \tilde{\mathbf{x}}_{\mathcal{C}} \end{bmatrix}, \Sigma = \begin{bmatrix} \Sigma_{\mathcal{I}} & \Sigma_{\mathcal{I}\mathcal{O}} & \Sigma_{\mathcal{I}\mathcal{C}} \\ \Sigma_{\mathcal{O}\mathcal{I}} & \Sigma_{\mathcal{O}} & \Sigma_{\mathcal{O}\mathcal{C}} \\ \Sigma_{\mathcal{C}\mathcal{I}} & \Sigma_{\mathcal{C}\mathcal{O}} & \Sigma_{\mathcal{C}} \end{bmatrix} \quad (4.7)$$

with  $\Sigma_{\mathcal{N}} = \begin{bmatrix} \Sigma_{\mathcal{I}} & \Sigma_{\mathcal{I}\mathcal{O}} \\ \Sigma_{\mathcal{O}\mathcal{I}} & \Sigma_{\mathcal{O}} \end{bmatrix}$  being the  $15 \times 15$  uncertainty of the navigation state  $\tilde{\mathbf{x}}_{\mathcal{N}}$ , and  $\Sigma_{\mathcal{C}} = \Sigma_{\mathcal{I}}$  being the  $6 \times 6$  uncertainty of the cloned IMU pose error state  $\tilde{\mathbf{x}}_{\mathcal{I}}$ .

The cloned pose does not evolve with time, meaning no state transition (i.e.,  $\Phi_{\mathcal{C}}^{k+1|k} = \mathbf{I}$ ) and no process noise (i.e.,  $\mathbf{G}_{\mathcal{C}}^{k+1|k} = \mathbf{0}$ ) is applied, while the original state estimate propagates as usual. From this, the error state propagation can be derived as

$$\begin{aligned} \tilde{\mathbf{x}}^{k+1} &= \Phi^{k+1|k} \tilde{\mathbf{x}}^k + \mathbf{G}^{k+1|k} \mathbf{w}^k, \\ \begin{bmatrix} \tilde{\mathbf{x}}_{\mathcal{N}}^{k+1} \\ \tilde{\mathbf{x}}_{\mathcal{C}}^{k+1} \end{bmatrix} &= \begin{bmatrix} \Phi_{\mathcal{N}}^{k+1|k} & \mathbf{0} \\ \mathbf{0} & \Phi_{\mathcal{C}}^{k+1|k} \end{bmatrix} \begin{bmatrix} \tilde{\mathbf{x}}_{\mathcal{N}}^k \\ \tilde{\mathbf{x}}_{\mathcal{C}}^k \end{bmatrix} + \begin{bmatrix} \mathbf{G}_{\mathcal{N}}^{k+1|k} \\ \mathbf{G}_{\mathcal{C}}^{k+1|k} \end{bmatrix} \mathbf{w}^k \\ &= \begin{bmatrix} \Phi_{\mathcal{N}}^{k+1|k} & \mathbf{0} \\ \mathbf{0} & \mathbf{I} \end{bmatrix} \begin{bmatrix} \tilde{\mathbf{x}}_{\mathcal{N}}^k \\ \tilde{\mathbf{x}}_{\mathcal{C}}^k \end{bmatrix} + \begin{bmatrix} \mathbf{G}_{\mathcal{N}}^{k+1|k} \\ \mathbf{0} \end{bmatrix} \mathbf{w}^k \end{aligned} \quad (4.8)$$

with the linearized state transition matrix  $\Phi$  and the linearized perturbation matrix  $\mathbf{G}$  computed as explained by Weiss in [81] or related work. The full error-state uncertainty of equation (4.7) can then be propagated as

$$\begin{aligned} \Sigma^{k+1} &= \Phi^{k+1|k} \Sigma^k (\Phi^{k+1|k})^T + \mathbf{G}^{k+1|k} \mathbf{Q}^k (\mathbf{G}^{k+1|k})^T \\ &= \begin{bmatrix} \Sigma_{\mathcal{N}}^{k+1} & \Phi_{\mathcal{N}}^{k+1|k} \Sigma_{\mathcal{N}\mathcal{C}}^k \mathbf{I} \\ \mathbf{I} \Sigma_{\mathcal{C}\mathcal{N}}^k (\Phi_{\mathcal{N}}^{k+1|k})^T & \Sigma_{\mathcal{C}}^k \end{bmatrix} \end{aligned} \quad (4.9)$$

with  $\mathbf{I}$  being the identity matrix (since cloned states do not evolve in time),  $\mathbf{Q}$  being the discretized process noise matrix,  $\Sigma_{\mathcal{C}\mathcal{N}}^k = (\Sigma_{\mathcal{N}\mathcal{C}}^k)^T$  the cross-covariance between the navigation error-state and the stochastic clone error-state, and  $\Phi_{\mathcal{N}}^{k+1|k}$  the error-state transition matrix of the navigation error-state  $\tilde{\mathbf{x}}_{\mathcal{N}}$ . This propagation allows us to rigorously reflect the cross-correlations between the cloned state and the evolved state in our error-state formulation. The above described formalism enables us to correctly use the state variables in order to align the previous radar scan to the current one prior to point matching.

### 3D Point Matching

In order to estimate the distance to detected points using our measurement model, we need to perform point matching between the current and the

previous radar scan aligned to the current UAV pose. This is roughly following the idea of [59] in order to avoid tracking 3D points in the state vector. With a single past pose in the state vector, we can find point correspondences in an ad-hoc fashion, as follows.

We base our point matching algorithm on work described in [13] and [4] for 2D ground vehicle setups and extend it to our 3D UAV setting. Having two consecutive radar scans which are aligned using the pose information stored in the state vector, as the first step, we solve the linear sum assignment problem using the Munkres algorithm [60]. We pose the problem as follows:

$$\min \sum_i \sum_j \mathbf{C}_{i,j} \mathbf{X}_{i,j} \quad (4.10)$$

Where  $\mathbf{X}$  is a boolean matrix where  $\mathbf{X}_{i,j} = 1$  iff row  $i$  is assigned to column  $j$ . Constraints of the problem are such that each row is assigned to at most one column and each column to at most one row. Entries of the  $\mathbf{C}$  matrix are computed as Euclidean distances between all points  ${}^R\mathbf{p}_P$  from a previous radar scan at time instance  $t_p$  and from a current radar scan at  $t_c$ :

$$\mathbf{C}_{i,j} = \| {}^R\mathbf{p}_{P_i}^{t_c} - {}^R\mathbf{p}_{P_j}^{t_p} \| \quad (4.11)$$

In the second step, using the proposed potential matches from the previous step, we build a matrix  $\mathbf{S}$  of scores where each entry is computed as:

$$s_{i,j} = \frac{1}{1 + \| {}^R\mathbf{p}_{P_i}^{t_c} - {}^R\mathbf{p}_{P_j}^{t_p} \|} \quad (4.12)$$

unless the value of reflection intensity in the current scan is below a certain threshold or the Euclidean distance is above certain maximum threshold. If either of the two aforementioned conditions holds true, the entry is set to  $s_{i,j} = 0$ . In the third step, a greedy search is performed on the pairs of points whose corresponding entries in  $\mathbf{S}$  are non-zero. If a point in the previous scan has more than one candidate for a match in the current scan, then, from among the candidates, we choose the one which minimizes the following expression:

$$d_{i,j} = \left| \sum_k \| {}^R\mathbf{p}_{P_i}^{t_c} - {}^R\mathbf{p}_{P_k}^{t_c} \| - \sum_k \| {}^R\mathbf{p}_{P_j}^{t_p} - {}^R\mathbf{p}_{P_k}^{t_p} \| \right| \quad (4.13)$$

Where  ${}^R\mathbf{p}_{P_k}^{\{t_c, t_p\}}$  are already matched points in the current and previous scans respectively. This idea has been exploited in [13] and relies on the fact that subsequent radar scans should ideally keep the relative arrangements between the constituting points (see figure 4.13). The result of this 3D point matching part is a set of 3D point correspondences (see figure 4.14) between a previous and the current radar scan. We can then compare the current radar measurements with the estimated distance value computed from the previous radar scan and the estimated state variables as described in the following section.

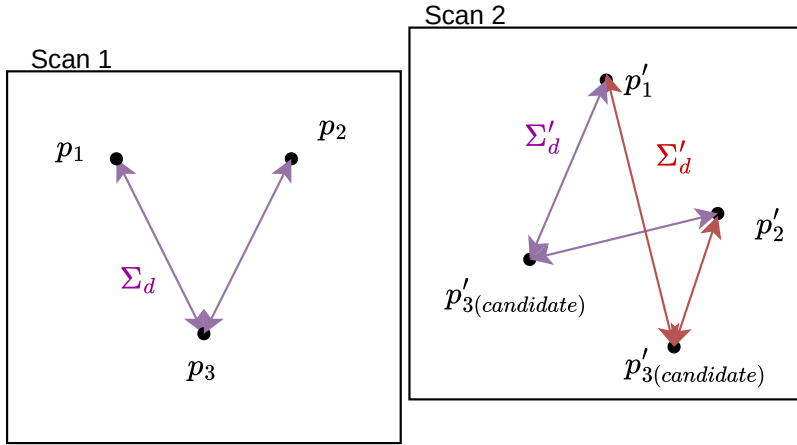


Figure 4.13: Points in subsequent scans should exhibit relative geometrical coherence. We exploit this observation (also used in [13, 36]) to guide the point correspondences search. Intuitively, if there are to candidates for a match, then its distance to some neighboring already matched points in the first scan should be close to the its distance to the matches of those points in the second scan.

### Distance Measurement Model

In order to estimate the distances to the matched 3D points in the current scan, we transform the corresponding 3D matches  ${}^R\mathbf{p}_{P_j}^{t_p}$  from the previous radar scan at time instance  $t_p$  to the current radar reference frame, consid-

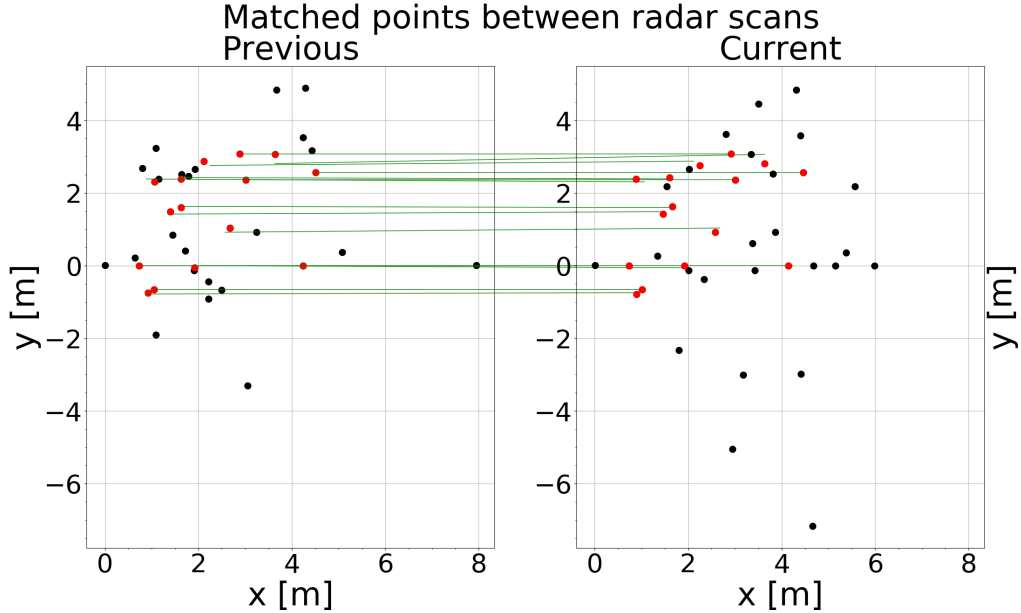


Figure 4.14: Matched points between subsequent scans projected onto the xy plane. Our matching algorithm proves to be robust in the face of outliers and sparse, noisy 3D point clouds.

ering the robot's spatial evolution:

$${}^R \mathbf{p}_{P_j}^{t_p} = {}^I \mathbf{R}_R^\top ( - {}^I \mathbf{p}_R + ({}^G \mathbf{R}_I^{t_c})^\top ( - {}^G \mathbf{p}_I^{t_c} + {}^G \mathbf{p}_I^{t_p} ({}^I \mathbf{p}_R + {}^I \mathbf{R}_R {}^R \mathbf{p}_{P_j}^{t_p}) ) ) \quad (4.14)$$

where  ${}^I \mathbf{R}_R$  and  ${}^I \mathbf{p}_R$  is the constant pose (orientation and position) of the radar frame with respect to the IMU frame.  ${}^G \mathbf{R}_I^{\{t_c, t_p\}}$  and  ${}^G \mathbf{p}_I^{\{t_c, t_p\}}$  are the IMU orientation and position corresponding to the previous and current radar scans at  $t_p$  and  $t_c$ , respectively, with respect to the navigation frame  $\{G\}$ .

Note that, at this point, we could already formulate a measurement for the matched 3D point in the past with the currently measured one. However, as mentioned in chapter 3, low-cost FMCW radars have fairly precise measurements of the object's distance and Doppler velocity, but heavily lack of precision in azimuth and elevation. Thus, we transform the 3D point from Cartesian space to Spherical coordinates and only use the most informative dimension, the distance. Additional measurement formulations for azimuth and elevation could be included with higher measurement uncertainty. The

low information versus added complexity and the non-Gaussian noise distribution in these dimensions are, however, arguments to not include them in our RIO framework.

The estimated distance, which is compared to the current distance measurement, is calculated for each point as the norm of the transformed point from  $t_p$ :

$$d_{P_j} = \left\| {}^R \mathbf{p}'_{P_j}^{t_p} \right\| \quad (4.15)$$

where  $d_{P_j}$  is the distance to a single matched 3D point  ${}^R \mathbf{p}'_{P_j}^{t_p}$  in the previous radar scan at  $t_p$  aligned to the current radar pose at  $t_c$ . Since this measurement relates to states from pastime instances, stochastic cloning is necessary as introduced earlier in this section.

### Velocity Measurement Model

In order to estimate the velocities of the detected radar 3D points  ${}^R \mathbf{v}_{P_i}$  in the current scan at  $t_c$ , we transform the current robot ego-velocity from the IMU frame into the current radar frame and subsequently project it onto the direction vector pointing towards the corresponding 3D point. This is expressed by the following measurement model:

$${}^R \mathbf{v}_{P_i} = \frac{\mathbf{r}^\top}{\|\mathbf{r}\|} \left( {}^I \mathbf{R}_R^T {}^G \mathbf{R}_I^T {}^G \mathbf{v}_I + {}^I \mathbf{R}_R^T ( {}_I \boldsymbol{\omega} \times {}^I \mathbf{p}_R ) \right) \quad (4.16)$$

where  $\mathbf{r} = {}^R \mathbf{p}_{P_i}$  is the 3D point detected in the current scan,  ${}_I \boldsymbol{\omega}$  is the current angular velocity of the IMU in the IMU frame, and  ${}^G \mathbf{v}_I$  is the current linear velocity of the IMU in the navigation frame. In order to reject outliers, we apply a chi-squared test to each measurement's residual, in which we check if the Mahalanobis distance corresponding to the residual is contained within the interval defined by the thresholds associated with a chosen percentile of the  $\chi^2$  distribution.

### Estimator Summary

In summary, our EKF-based RIO approach consists of equation (4.5) and equation (4.9) to propagate the state and its covariance using the IMU measurements. We then use a tightly-coupled formulation to compare the distances of matched features with current radar distance measurements using equation (4.14) and equation (4.15), and also include in a tightly-coupled fashion the velocity information the radar sensor provides

using equation (4.16) to correct IMU integration errors. The inclusion of both the point distance measurements and current point velocity information in a tightly-coupled fashion is key to the improved performance of our approach compared to state-of-the-art methods.

Although used in the position and velocity updates (equation (4.14) and equation (4.16)), we do not keep 3D points in the state vector. This idea is borrowed from [59] where 3D points are triangulated from images on-the-fly without inclusion in the state vector. Our adaptation to RIO and highly simplified implementation of this idea suffers from reduced estimation consistency, but results in less complexity. A thorough analysis of the statistical impact of this simplified implementation can be tackled in future work.

### 4.2.3 Experiments

The above described approach enables a simple, yet computationally efficient RIO method. In the following, we test our method on a real platform with real data.

#### Experimental Setup

The sensor used for the experiments is the lightweight and inexpensive 77 GHz multichannel millimeter-wave FMCW radar transceiver manufactured by Texas Instruments integrated on an evaluation board AWR1843BOOST, shown attached to the UAV in figure 4.15, equipped with a USB interface and powered with 2.5 V. The frequency spectrum of chirps generated by the radar is between  $f_l = 77$  GHz and  $f_u = 81$  GHz. The radio frequency (RF) signals propagate in a FOV of 120° in azimuth and 30° in elevation. Measurements are obtained at the rate of  $f_m = 20$  Hz. The radar is attached to one extremity of the experimental platform facing forward by a tilt of about 45° with respect to the horizontal plane as shown in figure 4.15. This improves the velocity readings compared to nadir view while keeping point measurements on the ground and thus at a reasonable distance. For inertial measurements, we use the IMU of the Pixhawk 4 flight controller unit (FCU) with a sampling rate of  $f_{si} = 200$  Hz. We manually calibrate the transformation between the radar and IMU sensors, which is used as a constant spatial offset in the EKF. The initial navigation states of the filter are set to the ground truth values with a random offset drawn from the states initial uncertainties as listed in table 4.2. The above described platform is moved in a hand-held manner across a spacious room, as shown in figure 4.16, repeatedly performing five times the same

Table 4.2: Initial standard deviation of the navigation states

	${}_G^G \mathbf{p}_I$	${}_G^G \mathbf{v}_I$	${}_G^G \mathbf{q}_I$	${}_I \mathbf{b}_a$	${}_I \mathbf{b}_\omega$
$\sigma^0$	0.32 cm	0.32 cm/s	0.1 rad	0.71 m/s <sup>2</sup>	0.1 rad/s

rectangular-shaped trajectory of approximate dimensions of slightly more than  $[4.5 \text{ m} \times 5.5 \text{ m}]$  traversing the total distance of 116.4 m. The scene was augmented with some arbitrary reflective clutter since the test environment was otherwise a clutter-less clean lab space. No position information from the added objects of any sort was used in our approach other than what the onboard radar sensor perceived by itself.

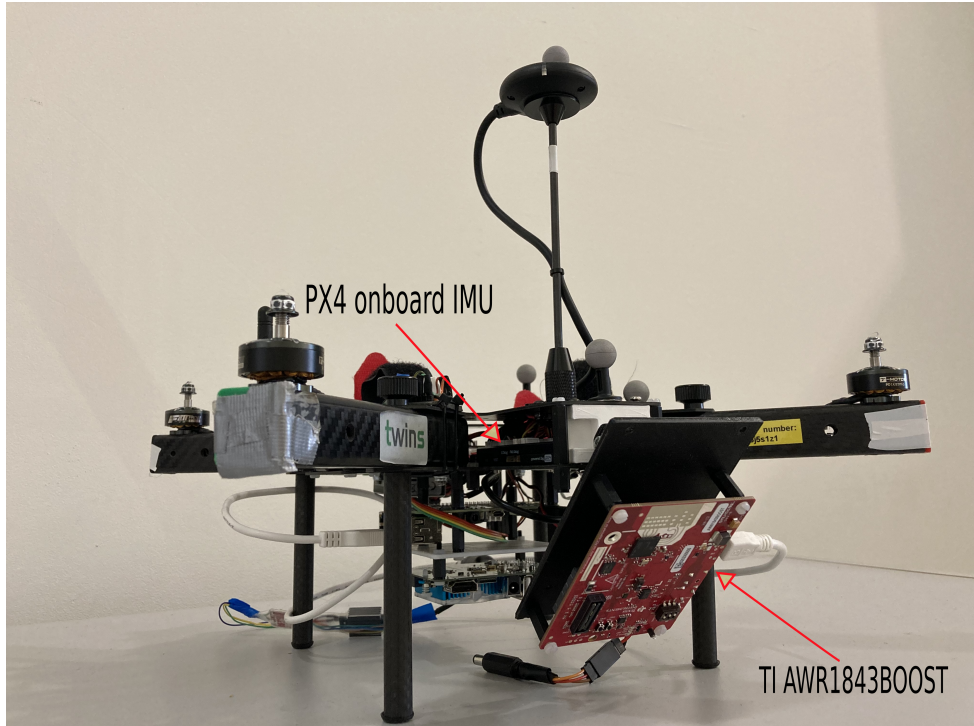


Figure 4.15: Experimental platform used in this work with the FMCW radar sensor mounted in its custom-made housing tilted at 45° angle.

We use a motion capture system to record the ground truth trajectories. During acquisition, we recorded sensor readings from the IMU and radar together with the poses of the UAV streamed by the motion capture system. Our EKF-based RIO is executed offline but at real-time speed on the



Figure 4.16: Indoor space where experiments were performed with reflecting clutter scattered on the scene. The objects were placed randomly and no global position (nor attitude) information of any sort was used in our approach.

recorded sensor data on an Intel Core i7-10850H vPRO laptop with 16 GB RAM in a custom C++ framework.

### Evaluation

We evaluate our RIO approach with the data recorded in an indoor space equipped with a motion capture system. Ground truth trajectories as well as the estimated ones can be seen in figure 4.17 to figure 4.18. On these plots, one can observe drift of the estimate versus the ground truth in position and yaw, since these four dimensions are unobservable in a RIO framework. The amount of drift is a direct measure of quality for a given approach.

Assessment of position, attitude, and velocity tracking is provided on plots figure 4.19, figure 4.20 and figure 4.21 respectively. For the position, one can clearly see the random walk behavior of this unobservable state. On this aspect, note that the provided metrics below are a snapshot of such a random walk (i.e., one of many realizations) – as are the numbers in e.g.,

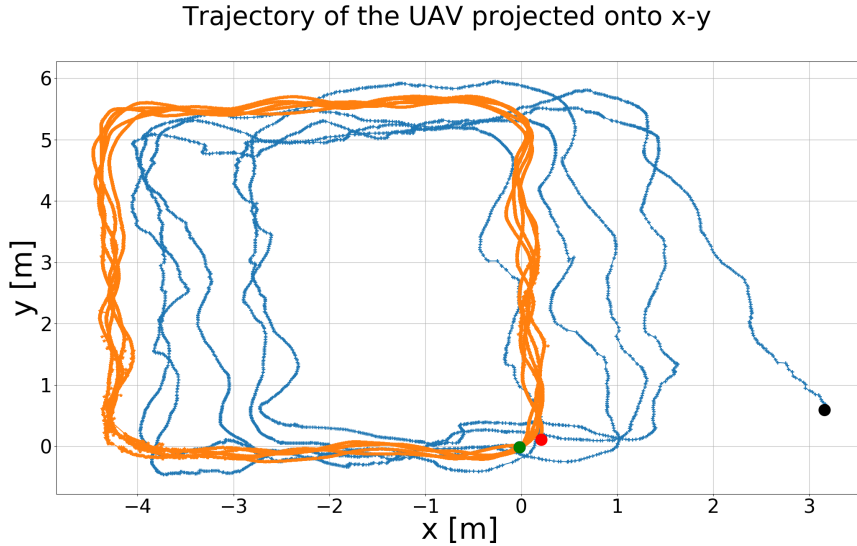


Figure 4.17: Top view of the UAV 3D trajectory. The true trajectory is plotted in orange and the estimated one in blue. The biggest (angular) drift can be noted after the last turn. Note the coloured dots marking the end and the beginning of trajectories.

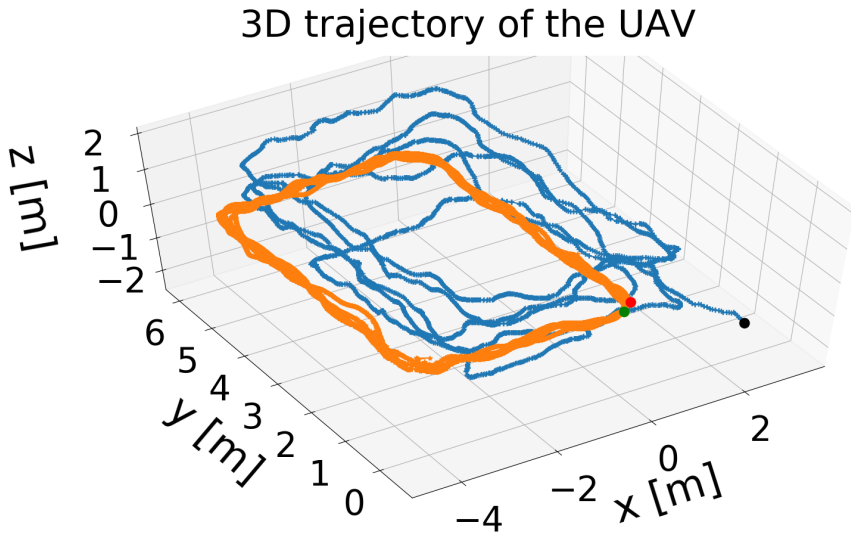


Figure 4.18: Side view of the UAV 3D trajectory. The true trajectory is plotted in orange and the estimated one in blue. The total of 116.4m distance is covered.

[23]. Nevertheless, the vast improvement against state-of-the-art shows that our approach generally has some beneficial aspects.

For the attitude, the drift in yaw is clearly visible. In this dataset we also observe an offset in pitch occurring after the first few seconds and remaining throughout the rest of the run. We assume a slight misalignment of the tracking system reference frame with respect to gravity. This value is observable in a RIO framework and will converge towards a gravity aligned reference frame.

The 3D velocity state is observable and the plot, besides the noticeable jitters also in the ground truth data, does not show a particularly unexpected behavior. The ground truth was computed by numerically differentiating the tracking system's position signal.

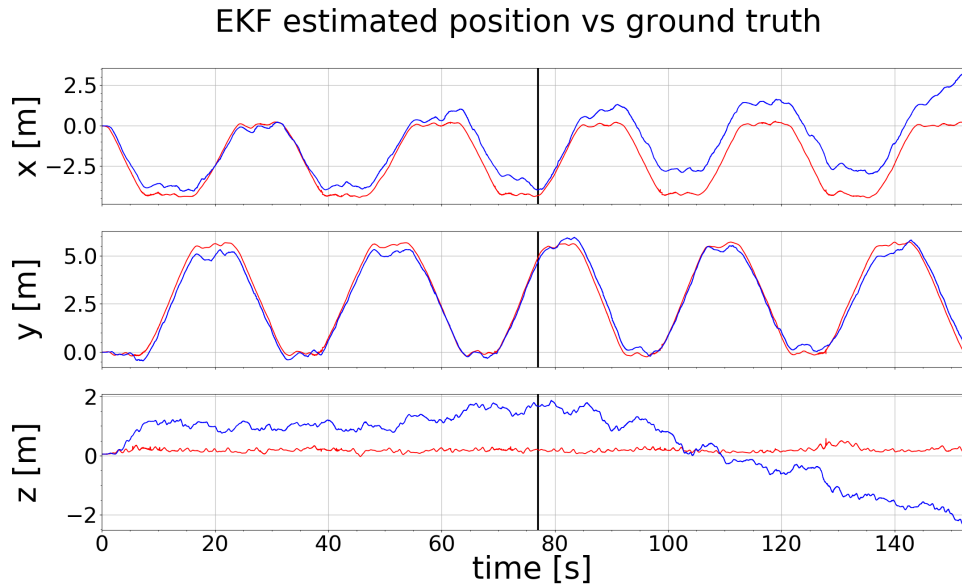


Figure 4.19: Estimated position plotted in blue against ground truth plotted in red. Note the thick black line passing through the time instant at which 60m distance has been traversed (this is for better metrics comparison against state of the art detailed in the text).

On figure 4.22 we plot the drift from the true trajectory as percent of the traveled distance, drift in meters (norm of the position error) and the total traveled distance (TTD).

The first  $t_{init} = 8$  s of the experiment was the initialization period during which agile motions were performed in-place in order to initialize the filter before executing the trajectory. All values are plotted after this initialization phase. We choose to compare our work to the state-of-the-art approach

EKF estimated attitude vs ground truth

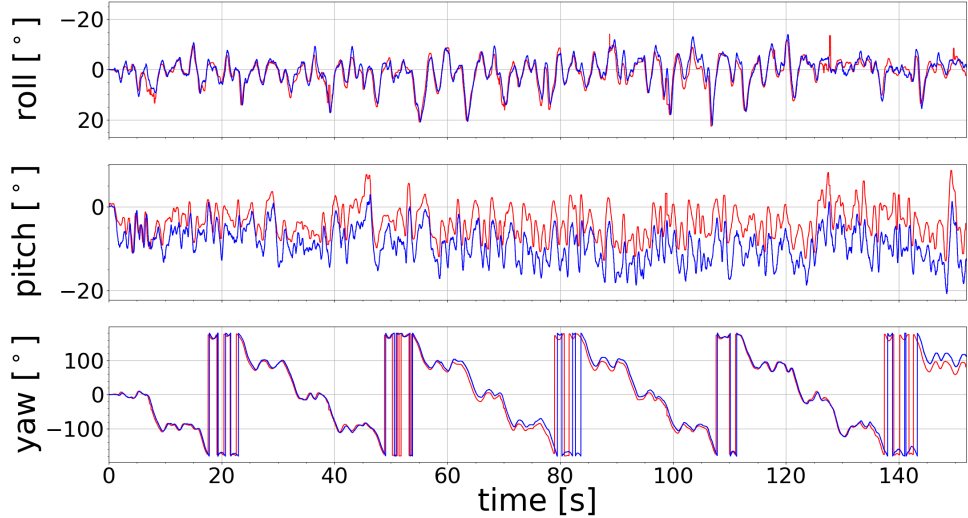


Figure 4.20: Estimated attitude plotted in blue against ground truth plotted in red. The offset in pitch angle is assumed to be caused by a slight misalignment of the motion capture system's reference frame and the gravity.

in [23] in which the authors use the same radar sensor to provide metrics for their loosely coupled radar-velocity based RIO approach using indoor hand-held data. In the following, we show the same metrics underlining the benefit of a) tight coupling and b) use of both distance and velocity information from the radar sensor. Note that in the same work, the authors also included a barometric pressure sensor in their RIO to further reduce drift. This would, however, be a different comparison.

Firstly, we evaluate final drift values. We can note in the figure 4.22 that over the TTD of 116.4 m we achieve a final drift below 4 m. Authors in [23] in their hand-held experiment achieve drift close to 4 m (or about 6.67%) over the trajectory of 60 m, which is roughly half of the distance covered in our experiment. Exact numbers for our approach are 3.86 m (3.32 % for TTD equal to 116.4 m) and 1.54 m (2.56 % for TTD equal to 60 m). Next, we compare the norm of mean absolute error (MAE) of position and velocity for TTD of 60 m. For our approach, these numbers are 1.05 m and  $0.38 \frac{m}{s}$  respectively, against 1.95 m and  $0.14 \frac{m}{s}$  for authors in [23]. At the TTD of 116.4 m the norm of MAE of position equals to 1.36 m and is still lower than the one from [23] at 60 m despite the inherent drift of the unobservable position in RIO approaches. The norm of MAE of velocity for our method at

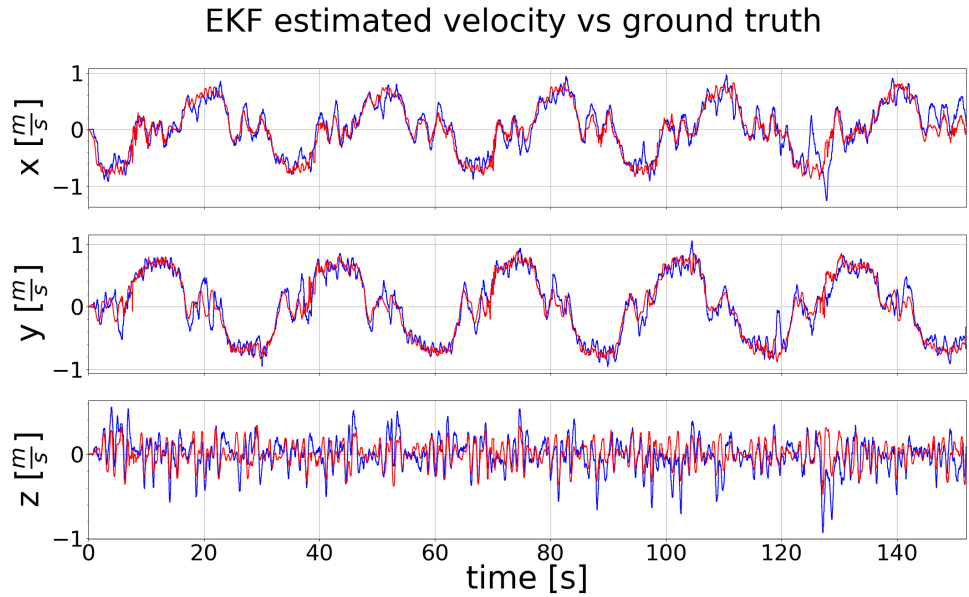


Figure 4.21: Estimated velocity plotted in blue against ground truth plotted in red. We compute the ground truth velocity by numerically differentiating the motion capture system's position.

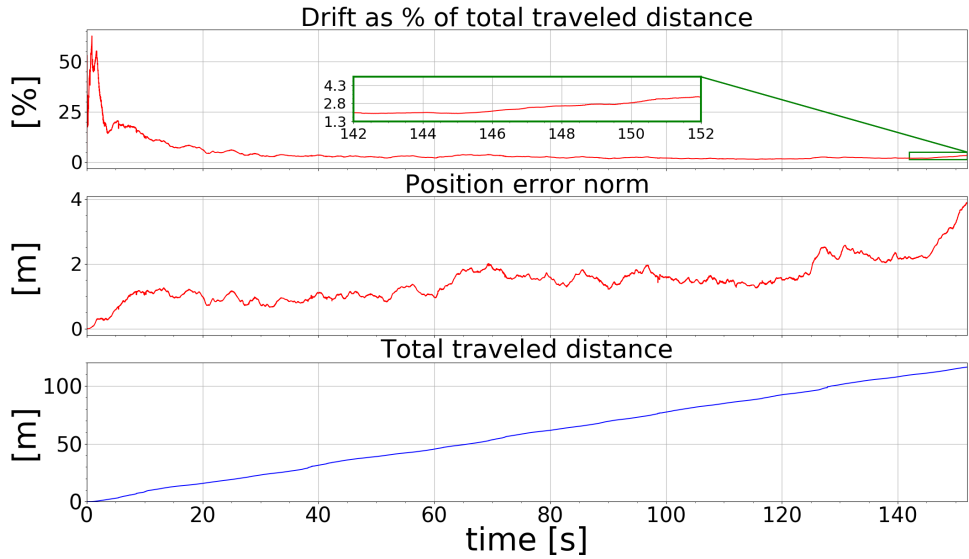


Figure 4.22: Drift as % of the TTD, position error norm and the TTD. The drift (position error norm) remains below 4m throughout the executed trajectory and reaches 3.32 % at the end of the TTD.

TTD of 116.4 m equals to  $0.36 \frac{\text{m}}{\text{s}}$ . The higher MAE in velocity compared to state of the art is an interesting fact: the velocity states are fully observable and should converge well. For ground truth velocity generation, we used the tracking system's position at 100 Hz and used a median filtered, delta-time scaled difference of this signal. This has highly limited precision and may have contributed to the relatively large MAE in velocity.

#### 4.2.4 Conclusions

In this section we presented a tightly-coupled EKF based approach to RIO in which we fuse IMU readings with both velocity and distance measurements to 3D points detected by lightweight and inexpensive FMCW radar. We make use of the past IMU pose and a rigid body assumption such that we can generate several point correspondences between two radar scans in an ad-hoc fashion. This requires only maintaining (through stochastic cloning) a 6DoF past pose in the state vector compared to tracking many 3D point vectors. In this context, we showed that our improved matching method can cope with noisy and sparse radar point clouds and generate reliably point correspondences between two scans. With this, we showed that using both distance and velocity measurements, we accomplish accurate 6D pose and 3D velocity estimation of a mobile platform (in this case a hand-held UAV). In particular, the use of the accurately measured distance information to a point is beneficial as it does not include the point's azimuth and elevation angular information which is generally very poorly measured by low-cost FMCW radar. Moreover, we showed that using our method, we reduce the position drift compared to similar state-of-the-art approach. Last but not least, our method is applicable in a variety of environments where potentially GNSS systems are unavailable and vision sensors, commonly used for UAV navigation, cannot be relied upon.

The approach to RIO shown in this section lends itself to be extended with powerful concepts from the camera-based state estimation, like exploiting multi-state constraints in the update step, as well as tracking the history of the detected 3D points in order to classify the ones consistently observed as persistent features. These aspects will be explored in the following sections.

### 4.3 RIO Multi-State EKF using distance, Doppler velocity measurements of 3D points, and persistent landmarks

Building upon the method developed in the previous section, in this section, we show an approach which significantly reduces the final drift (by a factor of 4 in average) and increases the accuracy (in terms of MAE by a factor of 2) of RIO compared to the single-frame approach described in the previous section (and in [54]) and demonstrate it in real flights. To this end, we employ the stochastic cloning [70] for augmenting the state with a chosen number of past robot poses and corresponding radar scans (3D point clouds) in a first in first out (FIFO) buffer from which measurement trails are constructed. Trails matched consistently over a given amount of time are promoted to persistent landmarks and added to the state vector. In addition to these distance measurements to landmarks and trails, we also use Doppler velocity of points from the current radar scan. We fuse all measurements in a tightly-coupled formulation in our EKF setup. The tight coupling permits the integration of single distance and velocity measurements during update steps. This property obviates any limitations on required minimal number of matches (as it is e.g., needed for a prior ICP and subsequent loose coupling of the resulting delta-pose in the EKF). This is a particularly strong advantage in view of robustness and accuracy over loosely coupled approaches since, e.g., ICP [7] works poorly on noisy and sparse FMCW radar point clouds. Note that our RIO method makes no assumptions on the environment and makes use of no other sensors than IMU and a lightweight millimeter-wave FMCW radar providing sparse and noisy 3D point clouds along with Doppler velocities of the detected points. It is suitable for a UAV and real-time capable.

Note that the leveraged techniques from the vision community [58], the sparse and noisy radar 3D (versus 2D in vision) measurements require important enhancements. This includes a different definition and treatment of 3D instead of 2D trails, a measurement definition along the most precise dimension of the sensor (i.e., radial distance), and the inclusion of Doppler velocity measurements. On the other hand, the multi-state approach for radar inherently handles hovering situations where the 2D vision measurements require special treatment.

### 4.3.1 System Overview

Our RIO method is based on an error-state EKF formulation [52] which uses an IMU as the primary sensor for the state propagation. Updates are performed with the FMCW radar measurements, which consist of sparse and noisy 3D pointclouds and relative radial velocities of detected points. The principle of sensing of the radar we use is explained in chapter 3. Every time a radar measurement is obtained, we augment the state of our EKF filter with the pose of the robot at which the measurement took place using stochastic cloning as described in section 4.3.2. New poses are appended to the buffer of past poses in a FIFO fashion. The maximum number of cloned poses is defined by the parameter  $N$ . From taken measurements, we construct and maintain a set of trails which record the continuous detectability of 3D points by the radar sensor, which have maximum trail length  $N$ . Meaning that, every matched point keeps a history of its detected positions and every element of this history refers to a cloned robot pose at which the detection was taken. Such a point with a history of detections is referred to as a trail and it is kept in memory as long as it is actively matched to a point in the current scan following our sparse radar point cloud matching method described in the section 4.2.1. If it is not matched, it is inactive and thus removed. For 3D point matching, we use the latest detection of each trail along with the robot pose at which it was taken, together with the pose at which the current scan was taken. Specifically, we use these two poses to spatially align the current radar scan with the trails and trigger the matching procedure on such aligned matches. Once matched, the whole trail history is used to form the residual vector in the EKF update.

It is important to note that as opposed to the way the features seen from multiple sensor poses are treated in [58], in our method we can continuously use all matched trails in every update step as long as they are visible, not merely once. That is because the radar sensor directly gives 3D points as measurements, hence no triangulation step is needed, which makes feature position calculations dependent on the state. Also, given the sparse nature of measurements emitted by the SoC FMCW radar sensor employed in our method, it is not necessary to carry out measurement compression with the QR decomposition as in [58].

Next, we use projections of the current robot velocity onto normal vectors to all points detected in the current radar scan together with their measured velocities to further augment the residual vector. The final component of the residual vector comes from using persistent landmarks. Namely, in the case a trail has been continuously seen for  $N$  times, it is removed from the set of trails, added to the state vector as persistent landmark and

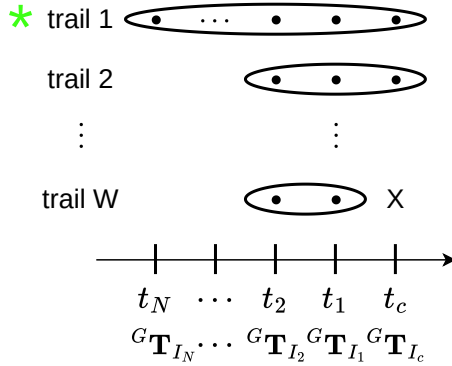


Figure 4.23: Measurement trails used to record a history of detections. The green star marks a trail that was classified as a persistent landmark. X means that the trail W has not been matched to any point in the current scan at  $t_c$  and will thus be deleted. Dot in each trail is a single past detection. As shown below time instant  $t$ , points in the trail have associated cloned robot poses at which the measurements were taken.

matched to the detections. Residual vectors are then used in the update step to estimate the mean of the error-state, which is injected into the regular state. The coordinate frames arrangement for measurements in our system is shown in figure 4.24.

### 4.3.2 Multi-State Radar-Inertial State Estimation With Persistent Landmarks

The state vector  $\mathbf{x}$  in our filter is defined as follows:

$$\mathbf{x} = [\mathbf{x}_I; \mathbf{x}_C; \mathbf{x}_L] = \left[ \left[ {}^G\mathbf{p}_I; {}^G\bar{\mathbf{q}}_I; {}^G\mathbf{v}_I; \mathbf{b}_a; \mathbf{b}_\omega \right]; \left[ {}^G\mathbf{p}_{I_1}; {}^G\bar{\mathbf{q}}_{I_1}; \dots; {}^G\mathbf{p}_{I_N}; {}^G\bar{\mathbf{q}}_{I_N} \right]; \left[ {}^G\mathbf{p}_{L_1}; \dots; {}^G\mathbf{p}_{L_M} \right] \right] \quad (4.17)$$

with the IMU state  $\mathbf{x}_I$ , the stochastically cloned states  $\mathbf{x}_C$  of the IMU poses corresponding to the previous radar measurements as described later on, and the set of persistent landmarks  $\mathbf{x}_L$ . The previous radar measurements (point cloud of reflecting objects and their Doppler velocities) are not part of the state vector.  ${}^G\mathbf{p}_I$ ,  ${}^G\mathbf{v}_I$ , and  ${}^G\bar{\mathbf{q}}_I$  are the position, velocity, and orientation of the IMU/body frame  $\{I\}$  with respect to the navigation frame  $\{G\}$ , respectively.  $\mathbf{b}_\omega$  and  $\mathbf{b}_a$  are the measurement biases of the gyroscope and accelerometer, respectively.  $[{}^G\mathbf{p}_{I_n}, {}^G\bar{\mathbf{q}}_{I_n}]$  with  $n = 1, \dots, N$

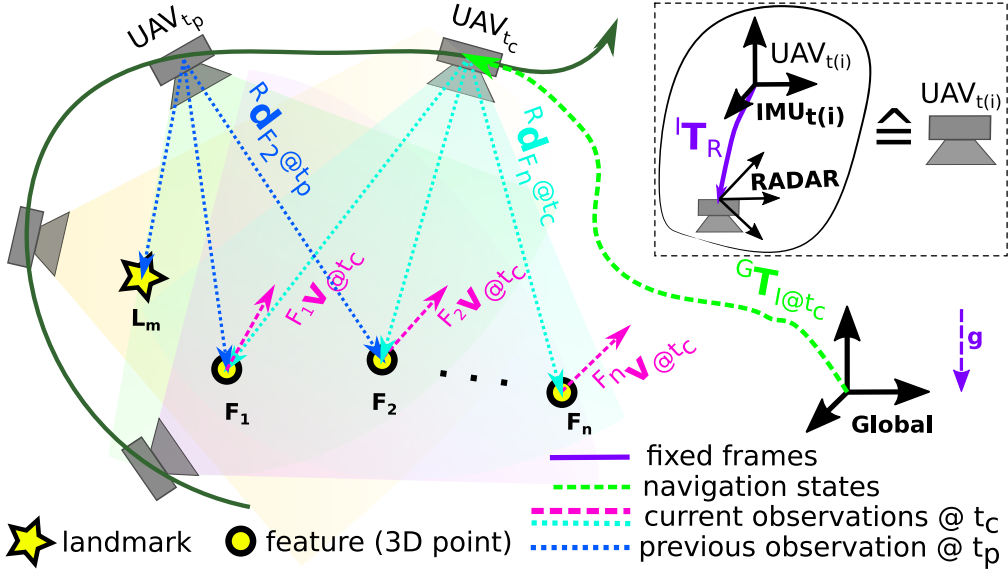


Figure 4.24: Multiple consecutive past UAV poses are used in the distance measurements models employing persistent landmarks and trails of measurements. In the velocity measurement model, only the readings from the current pose are used.

define a set of past IMU poses with respect to the navigation frame  $\{G\}$  at the moments of past radar measurements.  ${}^G\mathbf{p}_{L_m}$  with  $m = 1, \dots, M$  define the position of persistent landmarks  $\mathcal{L}$  with respect to the navigation frame  $\{G\}$ . We use  $[{}^G\mathbf{p}_{I_1}, {}^G\bar{\mathbf{q}}_{I_1}]$  (corresponding to the newest coordinates of the trails) for ad-hoc point correspondence generation such that we do not need to keep 3D points in the state vector in order to use distance based measurements.

The evolution of the state is expressed by the following differential equations:

$$\begin{aligned}
 {}^G\dot{\mathbf{p}}_I &= {}^G\mathbf{v}_I, \\
 {}^G\dot{\mathbf{v}}_I &= {}^G\mathbf{R}_I ({}_I\mathbf{a}^\# - \mathbf{b}_a - \mathbf{n}_a) + {}_G\mathbf{g}, \\
 {}^G\dot{\mathbf{R}}_I &= {}^G\mathbf{R}_I [{}_I\boldsymbol{\omega}^\# - \boldsymbol{b}_\omega - \mathbf{n}_\omega]_x, \\
 \dot{\mathbf{b}}_a &= \mathbf{n}_{b_a}, \dot{\boldsymbol{b}}_\omega = \mathbf{n}_{b_\omega}, {}^G\dot{\mathbf{p}}_{I_n} = \mathbf{0}, {}^G\dot{\mathbf{R}}_{I_n} = \mathbf{0}, \\
 {}^G\dot{\mathbf{p}}_{L_m} &= \mathbf{0}
 \end{aligned} \tag{4.18}$$

where  $n = 1, \dots, N$  refers to the most recent past IMU poses which are not changing in time,  $m = 1, \dots, M$  refer to  $M$  most recent estimated positions

of landmarks,  ${}_I\mathbf{a}^\#$  and  ${}_I\boldsymbol{\omega}^\#$  are the accelerometer and gyroscope measurements of the IMU with a white measurement noise  $\mathbf{n}_a$  and  $\mathbf{n}_\omega$ .  $\mathbf{n}_{b_a}$  and  $\mathbf{n}_{b_\omega}$  are assumed to be white Gaussian noise to model the bias change over time as a random process. The gravity vector is assumed to be aligned with the z-axis of the navigation frame  ${}_G\mathbf{g} = [0, 0, 9.81]^\top$ .

Since we use an error-state EKF formulation we introduce the error state vector from the states defined in equation (4.17):

$$\tilde{\mathbf{x}} = [\tilde{\mathbf{x}}_{\mathcal{I}}; \tilde{\mathbf{x}}_{\mathcal{C}}; \tilde{\mathbf{x}}_{\mathcal{L}}] = \left[ \begin{bmatrix} {}^G\tilde{\mathbf{p}}_I; {}^G\tilde{\boldsymbol{\theta}}_I; {}^G\tilde{\mathbf{v}}_I; \tilde{\mathbf{b}}_a; \tilde{\mathbf{b}}_\omega \\ {}^G\tilde{\mathbf{p}}_{I_1}; {}^G\tilde{\boldsymbol{\theta}}_{I_1}; \dots; {}^G\tilde{\mathbf{p}}_{I_N}; {}^G\tilde{\boldsymbol{\theta}}_{I_N} \end{bmatrix}; \begin{bmatrix} {}^G\tilde{\mathbf{p}}_{L_1}; \dots; {}^G\tilde{\mathbf{p}}_{L_M} \end{bmatrix} \right] \quad (4.19)$$

For translational components, e.g., the position, the error is defined as  ${}^G\tilde{\mathbf{p}}_I = {}^G\hat{\mathbf{p}}_I - {}^G\mathbf{p}_I$ , while for rotations/quaternions it is defined as  $\tilde{\mathbf{q}} = \hat{\mathbf{q}}^{-1} \otimes \bar{\mathbf{q}} = [1; \frac{1}{2}\tilde{\boldsymbol{\theta}}]$ , with  $\otimes$  and  $\tilde{\boldsymbol{\theta}}$  being quaternion product and small angle approximation, respectively.

### State Augmentation

In order to process relative measurements relating to estimates at different time instances, Roumeliotis and Burdick introduce the concept of Stochastic Cloning (SC) in [70]. To appropriately consider the correlations/interdependencies between the estimates from different time instances, an identical copy of the required states and their uncertainties is used to augment the state vector and the corresponding error-state covariance matrix. Given the error-state definition in equation (4.19),  $\tilde{\mathbf{x}}_{\mathcal{C}_i}$  is defined as the error-state of the  $i$ -th stochastic clone of the IMU pose  $[{}^G\mathbf{p}_{I_i}; {}^G\mathbf{q}_{I_i}]$ . As the newest cloned state is fully correlated with the IMU pose and remaining cloned states are correlated with each other, it leads to the following augmented covariance matrix of the corresponding error-state:

$$\tilde{\mathbf{x}} = [\tilde{\mathbf{x}}_{\mathcal{I}}; \tilde{\mathbf{x}}_{\mathcal{C}_1}; \dots; \tilde{\mathbf{x}}_{\mathcal{C}_n}; \tilde{\mathbf{x}}_{\mathcal{L}}], \quad (4.20)$$

$$\Sigma = \begin{bmatrix} \Sigma_{\mathcal{I}} & \Sigma_{\mathcal{I}\mathcal{C}_1} & \dots & \Sigma_{\mathcal{I}\mathcal{C}_n} & \Sigma_{\mathcal{I}\mathcal{L}} \\ \bullet & \Sigma_{\mathcal{C}_1} & \dots & \Sigma_{\mathcal{C}_1\mathcal{C}_n} & \Sigma_{\mathcal{C}_1\mathcal{L}} \\ \bullet & \bullet & \ddots & \vdots & \vdots \\ \bullet & \bullet & \bullet & \Sigma_{\mathcal{C}_n} & \Sigma_{\mathcal{C}_n\mathcal{L}} \\ \bullet & \bullet & \bullet & \bullet & \Sigma_{\mathcal{L}} \end{bmatrix} \quad (4.21)$$

with  $\Sigma_{\mathcal{I}}$  being the  $15 \times 15$  uncertainty of the IMU error-state  $\tilde{\mathbf{x}}_{\mathcal{I}}$ .  $\Sigma_{\mathcal{L}}$  is the  $3M \times 3M$  uncertainty of a set of  $M$  landmark error-states  $\tilde{\mathbf{x}}_{\mathcal{L}} =$

$[\tilde{\mathbf{x}}_{L_1}; \dots; \tilde{\mathbf{x}}_{L_m}]$ .  $\Sigma_{C_1} = \Sigma_{\mathcal{I}_{\{\tilde{\mathbf{p}}, \tilde{\boldsymbol{\theta}}\}}}$  is the  $6 \times 6$  uncertainty of the newly cloned IMU pose error state (which is fully correlated, thus  $\Sigma_{\mathcal{I}C_1} = \Sigma_{\mathcal{I}\mathcal{I}_{\{\tilde{\mathbf{p}}, \tilde{\boldsymbol{\theta}}\}}}$ ). All cross-covariances of the current IMU pose are assigned to the cross-covariances of the newly cloned state:  $\Sigma_{C_1C_i} = \Sigma_{\mathcal{I}_{\{\tilde{\mathbf{p}}, \tilde{\boldsymbol{\theta}}\}}C_i}$  with  $i = 2, \dots, n$  and  $\Sigma_{C_1\mathcal{L}} = \Sigma_{\mathcal{I}_{\{\tilde{\mathbf{p}}, \tilde{\boldsymbol{\theta}}\}}\mathcal{L}}$ .  $\Sigma_{C_n}$  is the  $6 \times 6$  uncertainty of the oldest cloned IMU pose.  $\Sigma_{C_iC_j}$  is the cross-correlation between  $i$ -th and  $j$ -th cloned IMU pose,  $\Sigma_{\mathcal{I}C_i}$  is the cross-correlation between the current IMU state and the  $i$ -th cloned IMU pose, and  $\Sigma_{C_i\mathcal{L}}$  are the cross-correlations between the cloned IMU poses and the landmarks.

The cloned poses and landmarks do not evolve with time, meaning no state transition and no process noise (i.e.,  $\Phi_{C_n}^{k+1|k} = \mathbf{I}$ ,  $\mathbf{G}_{C_n}^{k+1|k} = \mathbf{0}$  with  $n = 1, \dots, N$  and  $\Phi_{L_m}^{k+1|k} = \mathbf{I}$ ,  $\mathbf{G}_{C_n}^{k+1|k} = \mathbf{0}$  with  $m = 1, \dots, M$ ) is applied, while the navigation states evolve with the IMU measurements. The linearized error state propagation can be derived as:

$$\begin{aligned}
 \tilde{\mathbf{x}}^{k+1} &= \Phi^{k+1|k} \tilde{\mathbf{x}}^k + \mathbf{G}^{k+1|k} \mathbf{w}^k, \\
 \begin{bmatrix} \tilde{\mathbf{x}}_{\mathcal{I}}^{k+1} \\ \tilde{\mathbf{x}}_C^{k+1} \\ \tilde{\mathbf{x}}_{\mathcal{L}}^{k+1} \end{bmatrix} &= \begin{bmatrix} \Phi_{\mathcal{I}}^{k+1|k} & \mathbf{0} & \mathbf{0} \\ \mathbf{0} & \Phi_C^{k+1|k} & \mathbf{0} \\ \mathbf{0} & \mathbf{0} & \Phi_{\mathcal{L}}^{k+1|k} \end{bmatrix} \begin{bmatrix} \tilde{\mathbf{x}}_{\mathcal{I}}^k \\ \tilde{\mathbf{x}}_C^k \\ \tilde{\mathbf{x}}_{\mathcal{L}}^k \end{bmatrix} \\
 &\quad + \begin{bmatrix} \mathbf{G}_{\mathcal{I}}^{k+1|k} \\ \mathbf{G}_C^{k+1|k} \\ \mathbf{G}_{\mathcal{L}}^{k+1|k} \end{bmatrix} \mathbf{w}^k \\
 &= \begin{bmatrix} \Phi_{\mathcal{I}}^{k+1|k} & \mathbf{0} & \mathbf{0} \\ \mathbf{0} & \mathbf{I} & \mathbf{0} \\ \mathbf{0} & \mathbf{0} & \mathbf{I} \end{bmatrix} \begin{bmatrix} \tilde{\mathbf{x}}_{\mathcal{I}}^k \\ \tilde{\mathbf{x}}_C^k \\ \tilde{\mathbf{x}}_{\mathcal{L}}^k \end{bmatrix} + \begin{bmatrix} \mathbf{G}_{\mathcal{I}}^{k+1|k} \\ \mathbf{0} \\ \mathbf{0} \end{bmatrix} \mathbf{w}^k
 \end{aligned} \tag{4.22}$$

with the linearized state transition matrix  $\Phi$  and the linearized perturbation matrix  $\mathbf{G}$  computed as explained by Weiss in [81] or related work. The full error-state uncertainty of equation (4.21) can then be propagated as:

$$\begin{aligned}
 \Sigma^{k+1} &= \Phi^{k+1|k} \Sigma^k (\Phi^{k+1|k})^\top + \mathbf{G}^{k+1|k} \mathbf{Q}^k (\mathbf{G}^{k+1|k})^\top \\
 &= \begin{bmatrix} \Sigma_{\mathcal{I}}^{k+1} & \Phi_{\mathcal{I}}^{k+1|k} \Sigma_{\mathcal{I}C}^k \mathbf{I} & \Phi_{\mathcal{I}}^{k+1|k} \Sigma_{\mathcal{I}\mathcal{L}}^k \mathbf{I} \\ \bullet & \Sigma_{\mathcal{C}}^k & \Sigma_{\mathcal{C}\mathcal{L}}^k \\ \bullet & \bullet & \Sigma_{\mathcal{L}}^k \end{bmatrix} \tag{4.23}
 \end{aligned}$$

with  $\mathbf{Q}$  being the discretized process noise matrix and  $\Phi_{\mathcal{I}}^{k+1|k}$  the error-state transition matrix of the IMU error-state  $\tilde{\mathbf{x}}_{\mathcal{I}}$ . This propagation allows us to rigorously reflect the cross-correlations between the landmark, the cloned states, and the evolved IMU states in our error-state formulation. The above described formalism enables us to correctly use the state variables in order to align the trails to the current scan prior to point matching as well as compute residuals during the update.

### Multi-State Update With Measurement Trails

Given a set of matched 3D point-trails as in the figure 4.23, we now want to estimate the distances to the matched points in the current scan across all points contained in the trails history. For a single matched trail, using cloned poses in the buffer, we transform all points  ${}^R\mathbf{p}_{P_j}^{t_p}$  from the trail history at time instance  $t_p$ , where  $p = 1, \dots, V$  and  $V$  is the length of the matched trail, to the current radar reference frame, considering the robot's spatial evolution:

$$\begin{aligned}
 {}^R\mathbf{p}_{P_j}^{t_p} &= {}^I\mathbf{R}_R^\top \left( -{}^I\mathbf{p}_R + ({}^G\mathbf{R}_I^{t_c})^\top \left( -{}^G\mathbf{p}_I^{t_c} + \right. \right. \\
 &\quad \left. \left. {}^G\mathbf{p}_I^{t_p} + {}^G\mathbf{R}_I^{t_p} \left( {}^I\mathbf{p}_R + {}^I\mathbf{R}_R {}^R\mathbf{p}_{P_j}^{t_p} \right) \right) \right) \tag{4.24}
 \end{aligned}$$

where  ${}^I\mathbf{R}_R$  and  ${}^I\mathbf{p}_R$  is the constant pose (orientation and position) of the radar frame with respect to the IMU frame.  ${}^G\mathbf{R}_I^{\{t_c, t_p\}}$  and  ${}^G\mathbf{p}_I^{\{t_c, t_p\}}$  are the IMU orientation and position corresponding to the trail history element at time  $t_p$  and current radar scan at  $t_c$ , with respect to the navigation frame  $\{G\}$ . Similarly to the method described in section 4.2, we transform the 3D point from Cartesian space to Spherical coordinates and only use the most informative dimension, the distance for residual construction.

The estimated distance, which is compared to the current distance measurement, is calculated for each point in the trail history as the norm of the transformed point from  $t_p$ :

$$d_{P_j} = \left\| {}^R\mathbf{p}_{P_j}^{t_p} \right\| \tag{4.25}$$

where  $d_{P_j}$  is the distance to a single point in the matched trail history  ${}^R\mathbf{p}'_{P_j}^{t_p}$  at  $t_p$  aligned to the current radar pose at  $t_c$ . Since this measurement relates to states from past time instances, stochastic cloning is necessary as introduced earlier in this section.

### Update With Persistent Landmarks

When a trail has been continuously matched for a predefined amount of times in the past, it is promoted to a persistent landmark and added as such to the state vector. Specifically, after each update, the set of trails is scanned for elements which have been matched consecutively for  $N$  times. When a trail meets this criterion, it is used to initialize a persistent landmark in the state vector and the covariance matrix is augmented according to [74]. For convenience, we introduce  $\mathbf{x}_{\mathcal{D}} = [\mathbf{x}_{\mathcal{I}}; \mathbf{x}_{\mathcal{C}}]$ . Blocks needed for augmenting the state vector and error-state covariance are shown in the Fig. 4.25 and are computed as:

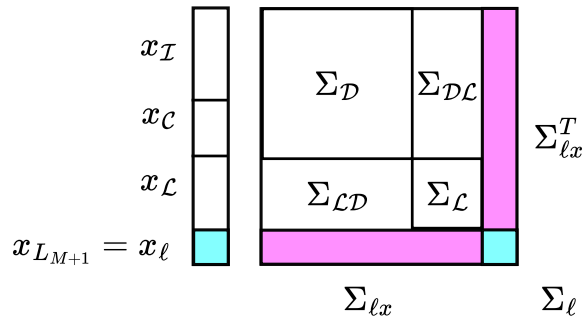


Figure 4.25: Augmented nominal state and error-state covariance after adding a persistent landmark.

$$\Sigma_{\ell} = \mathbf{H}_{\mathcal{D}} \Sigma_{\mathcal{D}} \mathbf{H}_{\mathcal{D}}^T + \mathbf{H}_{\ell} \mathbf{R} \mathbf{H}_{\ell}^T, \quad (4.26)$$

$$\Sigma_{\ell x} = \mathbf{H}_{\mathcal{D}} \Sigma_{\mathcal{D}x} \quad (4.27)$$

with  $\Sigma_{\mathcal{D}x} = [\Sigma_{\mathcal{D}}, \Sigma_{\mathcal{D}\mathcal{L}}]$ , and  $\Sigma_{\mathcal{D}\mathcal{L}}$  being the cross-covariance between the IMU and IMU clones error-state vector segment, and the persistent landmarks.  $\mathbf{R}$  is the covariance matrix of the measurement noise,  $\mathbf{H}_{\mathcal{D}} = \frac{\partial p}{\partial \tilde{\mathbf{x}}_{\mathcal{D}}}$  and  $\mathbf{H}_{\ell} = \frac{\partial p}{\partial \tilde{\mathbf{x}}_{\ell}}$  are the Jacobians of the inverse observation model of a 3D point radar measurement,  $p$  (Eq. 4.28), with respect to the IMU and IMU

clones error-state variables  $\tilde{\mathbf{x}}_D$ , and the error-state variable  $\tilde{\mathbf{x}}_\ell$  of the newly added landmark  $\mathbf{x}_\ell = \mathbf{x}_{L_{M+1}}$ , respectively. The inverse observation model of the 3D radar point in the navigation frame  $\{G\}$  is expressed as:

$${}^G \mathbf{p}_{L_m} = p(\mathbf{x}, \mathbf{z}) = {}^G \mathbf{R}_I ({}^I \mathbf{R}_R {}^R \mathbf{p}_{L_m} + {}^I \mathbf{p}_R) + {}^G \mathbf{p}_I \quad (4.28)$$

with  ${}^I \mathbf{R}_R$  and  ${}^I \mathbf{p}_R$  being the pose between the IMU and radar sensor (which is assumed to be rigid and known a-priori),  ${}^R \mathbf{p}_{L_m}$  is the radar observation of the trail point in the current radar reference frame  $\{R\}$  with which an  $m$ -th landmark will be initialized, and  ${}^G \mathbf{R}_I$  and  ${}^G \mathbf{p}_I$  being the current pose of the IMU in the navigation frame. For readability, the estimate of the  $m$ -th landmark is abbreviated by  $\mathbf{l}_m = {}^G \mathbf{p}_{L_m}$ .

When a persistent landmark does not have a match within the current radar scan, then it is discarded from the state vector and the covariance matrix is shrunk accordingly.

Finally, the estimated distance used for the update is computed according to:

$$\mathbf{l}'_m = {}^R \mathbf{p}_{L_m} = {}^I \mathbf{R}_R^\top ({}^G \mathbf{R}_I^\top (\mathbf{l}_m - {}^G \mathbf{p}_I) - {}^I \mathbf{p}_R), \quad (4.29)$$

$$d_{\mathbf{l}_m} = \|\mathbf{l}'_m\| \quad (4.30)$$

### Estimator Summary

Summarizing, in our RIO method we propagate the state and its covariance according to equation (4.18) and equation (4.23). The update step of our tightly-coupled EKF consists of three components - the first one makes use of distances to points in the history elements of trails compared to current radar measurements (equation (4.24) and equation (4.25)), the second one compares distances of persistent landmarks to current radar measurements (equation (4.29) and equation (4.30)), Finally, the third component employs Doppler velocities as in section 4.2 reduced to the inlier set using 3-point RANSAC as detailed in [23]. For all components, we apply outlier rejection using the chi-squared test.

#### 4.3.3 Experiments

In the following, we outline the setup we used and the experiments we performed to validate our method on a real platform with the data from real flights as well as the results of the evaluation.

## Experimental Setup

The sensor used for the experiments is a lightweight and inexpensive FMCW radar manufactured by Texas Instruments integrated on an evaluation board AWR1843BOOST, shown attached to the UAV in figure 4.15, equipped with a USB interface and powered with 2.5 V. The frequency spectrum of chirps generated by the radar is between  $f_l = 77$  GHz and  $f_u = 81$  GHz. The FOV is  $120^\circ$  in azimuth and  $30^\circ$  in elevation. Measurements are obtained at the rate of  $f_m = 15$  Hz. The radar is affixed to one extremity of the experimental platform facing forward by a tilt of about  $45^\circ$  with respect to the horizontal plane as shown in figure 4.15. This improves the velocity readings compared to nadir view while keeping point measurements on the ground and thus at a reasonable distance. For inertial measurements, we use the IMU of the Pixhawk 4 flight controller unit (FCU) with a sampling rate of  $f_{si} = 200$  Hz. We manually calibrate the transformation between the radar and IMU sensors, which is used as a constant spatial offset in the EKF. The initial navigation states of the filter are set to the ground truth values.  $N$  was set to 7. We placed some arbitrary reflective clutter in the scene since the test environment was otherwise a clutter-less clean lab space. No position information from the added objects of any sort was measured or used in our approach other than what the onboard radar sensor perceived by itself. We use a motion capture system to record the ground truth trajectories. During acquisition, we recorded sensor readings from the IMU and radar together with the poses of the UAV streamed by the motion capture system as ground truth. Our EKF-based RIO is executed offline on the recorded sensor data on an Intel Core i7-10850H vPRO laptop with 16 GB RAM in a custom C++ framework compiled with gcc 9.4.0 at -O3 optimization level. In the case of the closed-loop flight in section 4.3.5, we recorded the pose estimates calculated (and fed to the controller) onboard in real-time by our RIO. Our RIO was executed on a raspberry pi 4 with 4 GB RAM mounted on the platform. Execution timings for the aforementioned machines are shown in table 4.4 and table 4.6, and confirm the real-time capability of the implementation.

## Evaluation

For evaluation of the presented RIO approach, we use the data recorded in an indoor space shown in figure 4.26 during seven manually-controlled UAV flights. The flown trajectories were not pre-planned and included pronounced motions in all three dimensions. One of the executed trajectories can be seen in the figure 4.27. We choose to measure the quality of our esti-

mator using the norm of MAE of position and the final pose drift in percent (without yaw alignment) in order to easily compare against the state-of-the-art. In figure 4.28, one can observe the mean of the  $\|\text{MAE}\|$  across the flown trajectories. The  $\|\text{MAE}\|$  increases steadily with the flown distance as the pose drift builds up as expected. For comparison, we show that the  $\|\text{MAE}\|$  is reduced by a factor of 2 with respect to our previous results presented in section 4.2, and by a factor of 4 with respect to the state-of-the-art shown in [23] where only an FMCW radar and IMU is used and no assumptions on environment are made. The sample based  $1\sigma$  bounds grow to a value of about  $\sigma = 0.25\text{ m}$ . Regarding the final drift, as shown in Tab. 4.3, on average we achieve 0.81% on trajectories ranging from 127.5 m to 175.0 m against 5.0% reported for a 60 m long flown trajectory in [23] for a similar setup as ours consisting of only FMCW radar and IMU. Authors in [23, 24] also report the final drift values for the same setups, yet additionally augmented with a barometer sensor to reduce the vertical drift - even in this case our results with no additional sensor remain comparable - 0.81% (ours) against 0.60% [23] and 0.36% [24]. Interestingly, the minimum value of the final drift in our experiments - 0.17% - is even lower than the lowest value reported in [23, 24] obtained flying the same distance but with additional sensors and much lower excitation in their case. Compared to 3.32% final drift for a hand-held trajectory of 116.4 m with low excitation in section 4.2, our method outperforms it by a factor of 4 in a real IMU flight with high excitation.

Table 4.3: Metrics gathered across all flown trajectories

Trajectory	Length [m]	Norm of MAE at 127 m [m]	Final drift [%]
1	127.5	0.90	<b>0.17</b>
2	150.5	1.10	1.62
3	158.4	0.68	0.80
4	160.4	0.71	0.61
5	166.7	0.59	0.78
6	168.1	0.84	0.91
7	175.0	<b>0.45</b>	0.81
Average		<b>0.75</b>	<b>0.81</b>

Table 4.4: Execution timings for a single trajectory

	Average time [ms]		Duration [s]	Realtime factor
	Propagation	Update		
Trajectory 7	0.08	2.07	436	25.36

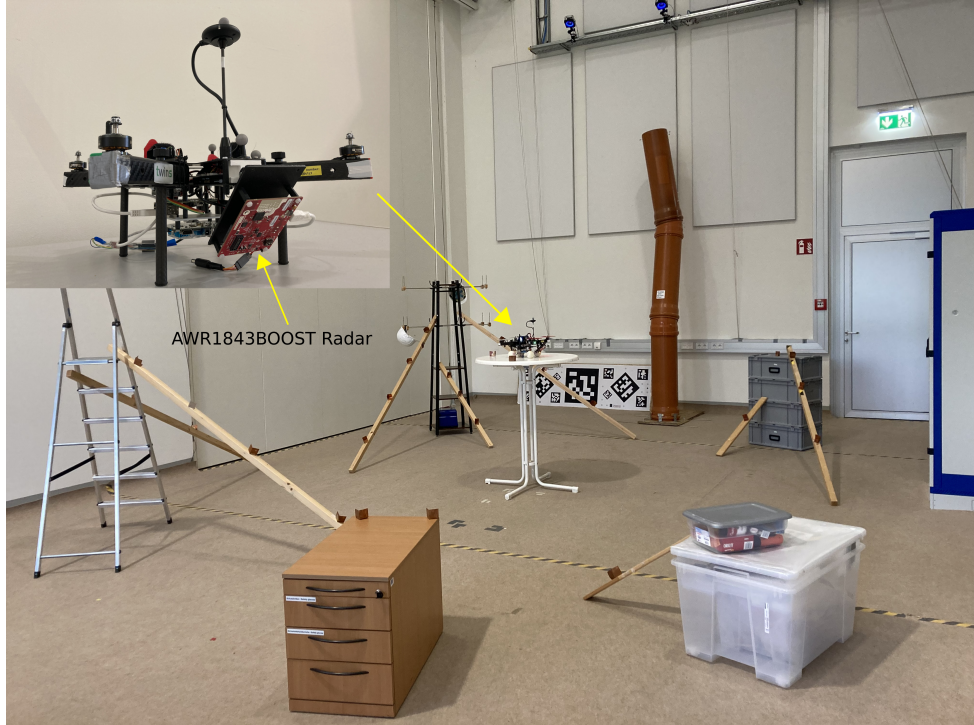


Figure 4.26: Experimental platform used in this work with the FMCW radar sensor and the indoor space where the experiments were conducted. Note the mounting of the sensor tilted at 45° angle. Reflective clutter was scattered randomly on the scene. No global position (nor attitude) information of any sort about scattered objects was used in our approach.

#### 4.3.4 Online Calibration and its Impact on the Accuracy and Consistency of The Multi-State EKF RIO

In this section we introduce the online estimation of the extrinsic calibration parameters and thus simplifying the use of the framework as well as improving its accuracy and consistency. With online extrinsic calibration parameters the state vector looks as follows:

$$\mathbf{x} = [\mathbf{x}_I; \mathbf{x}_R; \mathbf{x}_C; \mathbf{x}_L] = \left[ \begin{bmatrix} {}^G\mathbf{p}_I; {}^G\bar{\mathbf{q}}_I; {}^G\mathbf{v}_I; \mathbf{b}_a; \mathbf{b}_\omega; \right. \right. \\ \left. \left. [{}^I\mathbf{p}_R; {}^I\bar{\mathbf{q}}_R]; [{}^G\mathbf{p}_{I_1}; {}^G\bar{\mathbf{q}}_{I_1}; \dots; {}^G\mathbf{p}_{I_N}; {}^G\bar{\mathbf{q}}_{I_N}]; \right. \right. \\ \left. \left. [{}^G\mathbf{p}_{L_1}; \dots; {}^G\mathbf{p}_{L_M}] \right] \right] \quad (4.31)$$

where the newly added state variables  $[{}^I\mathbf{p}_R; {}^I\bar{\mathbf{q}}_R]$  describe the 3D pose

3D trajectory of the UAV

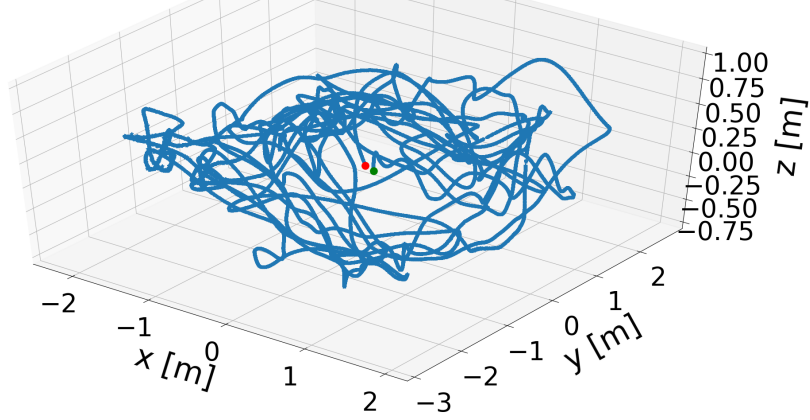


Figure 4.27: One of the executed trajectories. As can be seen, we tried to perform pronounced motions in all three dimensions. Green and red dots represent the take-off and landing positions on the white table seen in the figure 4.26.

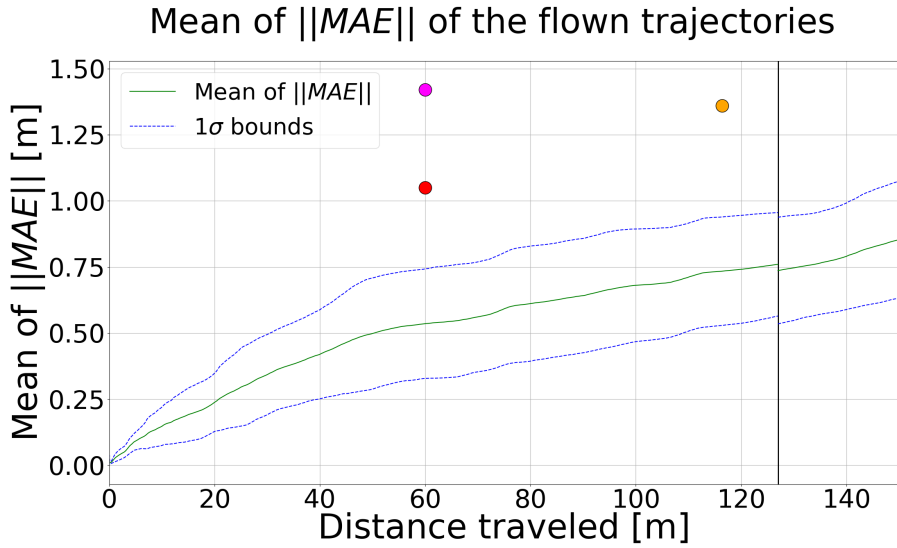


Figure 4.28: Mean of the norm of MAE for all flown trajectories. Up to 127 m the mean of all trajectories is taken. From 127 m to 150 m mean of six trajectories is taken (since trajectory 1 ended). Blue dashed lines are the sample based  $1\sigma$  bounds. For comparison, red and orange dots represent results presented in section 4.2 and the magenta dot represent the state-of-the-art result in [23] for the flown trajectory.

of the radar sensor with respect to the IMU sensor. After the addition of the sensor extrinsic calibration parameters as variables to the state vector the stochastic cloning procedure remains analogous to the one reported in section 4.3, with the only difference being, that the covariance matrix blocks containing the cross-covariance terms copied upon the cloning of a new IMU state are bigger in size. Namely, the increase in size corresponds to the two  $3 \times 3$  blocks which correspond to the cross-covariance values between the state-to-be-cloned and the calibration error states - position and orientation. Naturally, during propagation the calibration states do not evolve in time hence, we add the following equations to equation (4.18):

$$\begin{aligned} {}^I \dot{\mathbf{p}}_R &= \mathbf{0} \\ {}^I \dot{\mathbf{R}}_R &= \mathbf{0} \end{aligned} \quad (4.32)$$

Estimation accuracy is impacted by the precision of the extrinsic calibration parameters of the sensors. Also, as stated in [47], the unmodelled uncertainty of these parameters when treated as static negatively impacts the filter's consistency. Therefore, we propose to estimate these parameters online during the operation of the algorithm. This renders the platform easier to use as the calibration parameters are not needed to be measured manually nor any complex calibration procedure is required. Online calibration estimation also increases the accuracy which can be seen in Fig. 4.29 where we note the reduction of the  $\|MAE\|$  for the same dataset used in section 4.3, but with the here proposed online calibration implemented. Additionally, based on the analysis done in [39] and [40], we know that these parameters are observable for general trajectories.

In the Fig. 4.30 and Fig. 4.31, we can see comparisons of the position estimation errors (with  $\pm 3\sigma$  envelopes) and the position normalized estimation error squared (NEES) respectively for the case of manual and online calibration for one of the trajectories from the above mentioned dataset. In Fig. 4.30, we can observe that our system with online calibration exhibits better characterization of the actual uncertainty as the estimation errors are bounded by the  $\pm 3\sigma$  envelopes across the vast majority of the trajectory and the errors oscillate closer to zero. The bounded segments are less frequent for the case of the manual calibration and the errors are shifted further away from zero. These aspects are also reflected in Fig. 4.31 which depicts the comparison of the NEES for the same data as for the position errors above. The above comparisons indicate much better consistency for the case with the online calibration since the NEES is greatly reduced (Bar-Shalom et al. [5]). In the case of manual calibration, we paid close attention to measuring as accurately as possible the extrinsic parameters

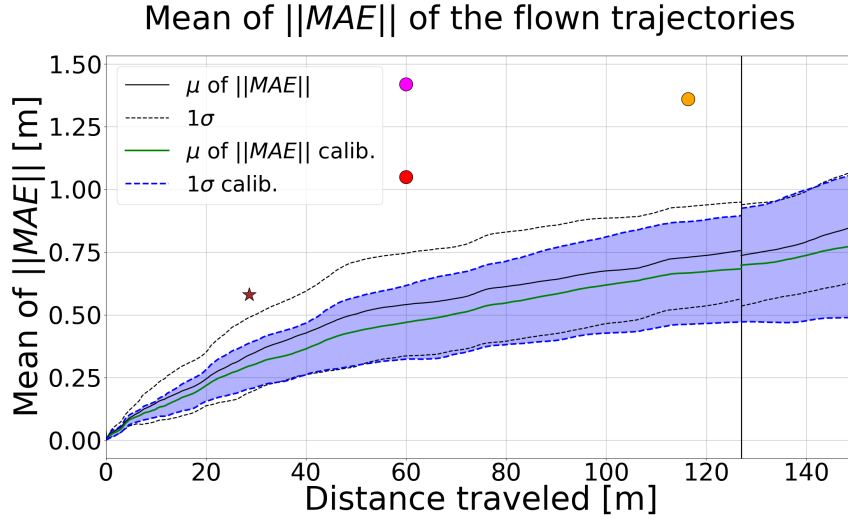


Figure 4.29: Mean of the norm of MAE for the flown dataset of seven trajectories from section 4.3. Black dashed lines are from section 4.3 whereas the coloured lines are the values obtained for the same dataset but with the online calibration implemented. As can be noticed there is an increase in accuracy (mean of  $\|MAE\|$  reduced). Marked with the brown star is the mean value obtained for the closed-loop flights presented in the section 4.3.5 (Tab. 4.5). For comparison, red and orange dots represent results presented in section 4.2 and the magenta dot represent the state-of-the-art result in [23] for the flown trajectory. From 127 m to 150 m six trajectories are used to compute the mean since trajectory 1 ended at 127 m (solid black vertical line).

of the sensors. Manually measured calibration parameters were used as the initial values for the case of online calibration.

In the figure 4.32 and figure 4.33 we plot the convergence of the extrinsic calibration parameters to their measured values for one of the trajectories in the case where the initial extrinsic calibration parameters were initialized with vastly erroneous values, that is,  $\mathbf{c}_{trans}^{init} = [x = -40 \text{ cm}, y = -40 \text{ cm}, z = -40 \text{ cm}]$  in position and  $\mathbf{c}_{rot}^{init} = [roll = 20^\circ, pitch = 20^\circ, yaw = 20^\circ]$  in orientation. Extrinsic calibration parameters which we measured manually with simple tools such as a ruler and a protractor were equal to  $\mathbf{c}_{trans}^{meas} = [7.5 \text{ cm}, -1.0 \text{ cm}, -4.0 \text{ cm}]$  and  $\mathbf{c}_{rot}^{meas} = [0^\circ, 47^\circ, 0^\circ]$ . Given the lack of ground truth for these parameters, we consider the manually measured values the true ones. As observed, our filter successfully recovers from such high initial calibration errors and the parameters converge very close to their

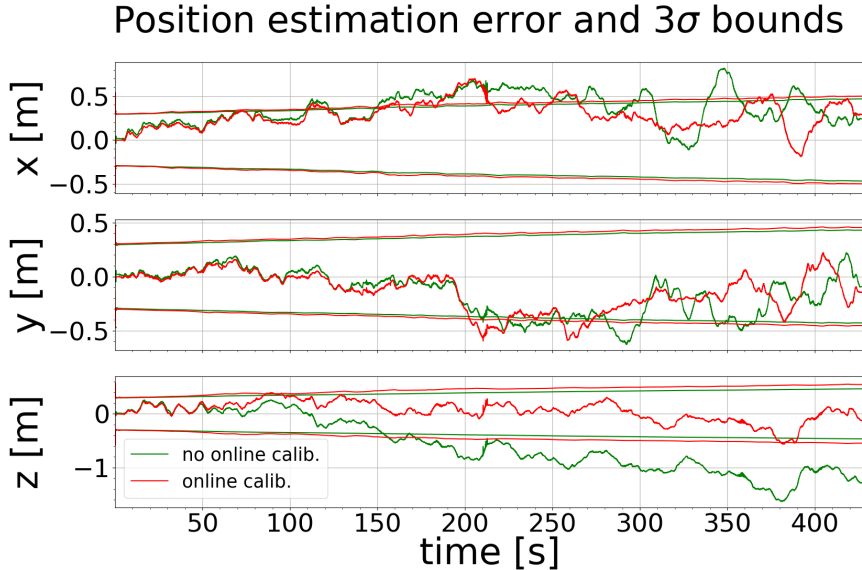


Figure 4.30: Comparison of the position estimation errors and the  $\pm 3\sigma$  uncertainty envelopes for one of the trajectories from the dataset in section 4.3 with the manual and the online calibration (green and red respectively). As can be seen in the case of the online calibration, the errors are more thoroughly bounded by the uncertainty across the trajectory than in the case of the manual calibration. Since the estimator is inherently inconsistent [47], one cannot expect the errors to be bounded 99.7 % of the time.

manually measured values. The difference between measured and estimated values are  $\mathbf{c}_{trans}^{diff} = [6.4 \text{ cm}, 2.6 \text{ cm}, 5.0 \text{ cm}]$  and  $\mathbf{c}_{rot}^{diff} = [0.087^\circ, 2.50^\circ, 3.27^\circ]$  in position and rotation respectively for this particular run which is representative for the majority of the runs. These numbers are comparable to [82] where the authors used synthetic data with a dedicated calibration procedure while we use real data during a regular UAV flight with no dedicated calibration procedure.

Even though the estimated and measured values are similar in the estimator's asymptotic behavior, the previously discussed consistency improvement is noticeable. This stems from the filter's ability to include the calibration states for its energy dissipation rather than being hindered to adapt these states online.

For completeness of the discussion about our estimator consistency, we note that we have not implemented yet the approach suggested in [37]. Thus we expect further consistency improvement by doing so in future work.

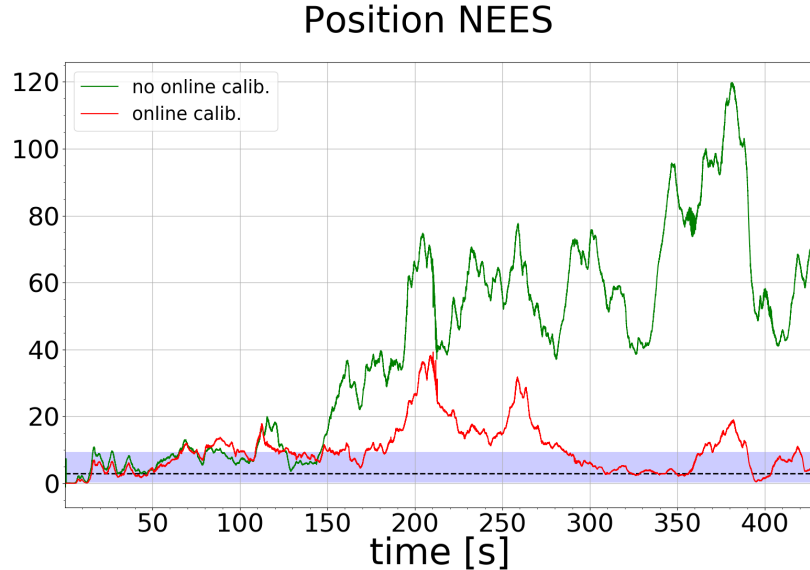


Figure 4.31: Comparison of the position NEES for one of the trajectories with the manual and the online calibration (green and red respectively). The filter consistency is greatly improved with the online calibration which can be seen in the significant reduction of the NEES, which in the case of the online calibration does not continue to grow and more often remains bounded within the two-sided 95 % probability concentration region (shaded blue) than in the case of manual calibration.

### 4.3.5 Multi-State EKF RIO Closed-Loop Flights

For evaluation of the presented RIO approach, we design a 3D trajectory such that the UAV can execute it within the motion capture covered area. The top view of the trajectory can be seen in green in the figure 4.34. The UAV then executes this trajectory twice within a single mission using the state estimates computed by our RIO implementation onboard in real-time. We executed three missions and computed the mean values of the final drift and the norm of MAE for each of them. Our estimator exhibited stable behaviour in all performed flights. Computed mean values are 2.84 % for the final drift and 0.58 m for  $\|MAE\|$  (see table 4.5). The mean traveled distance across trajectories is 28.62 m. As can be seen in the figure 4.29, the accuracy (measured by  $\|MAE\|$ ) obtained in closed-loop flights, marked with a brown star, lies slightly above the mean calculated over the manually flown and subsequently offline processed dataset of seven trajectories collected in indoor space (figure 4.26). We attribute this slim discrepancy

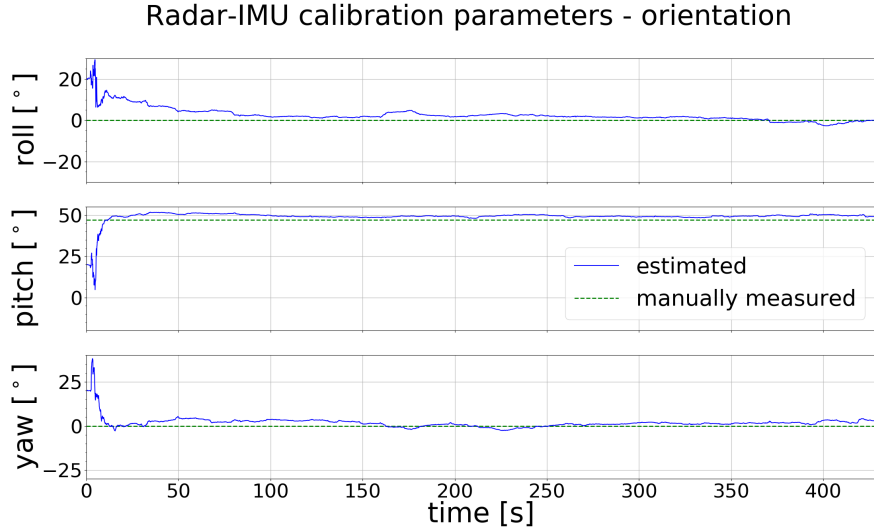


Figure 4.32: Convergence of the rotational extrinsic calibration parameters for the system with extremely high initial calibration errors. Including the extrinsic calibration parameters in the state vector enables the system to recover from extremely inaccurate initial calibration values and eventually converge to the real values reflecting the tilt of the radar of about  $45^\circ$  around the y axis (we manually measured  $47^\circ$ ) around the y-axis. Green dashed lines are used to mark the manually measured extrinsic calibration parameters values which we consider the true values since we do not have a precise ground truth on these quantities.

to the online closed-loop execution of the estimator and controller on a resource-constrained hardware during which some of the measurements are dropped due to CPU load spikes. We note that these are precisely the challenges when demonstrating estimation approaches in closed-loop autonomous flights and that these are important factors our RIO approach is able to mitigate well. In the figure 4.35 we plot the 2D coordinates of the estimated and true position. In table 4.6 we show the average values of the time it takes to execute the entire IMU and radar processing functions on the onboard computer mentioned in section 4.3.3.

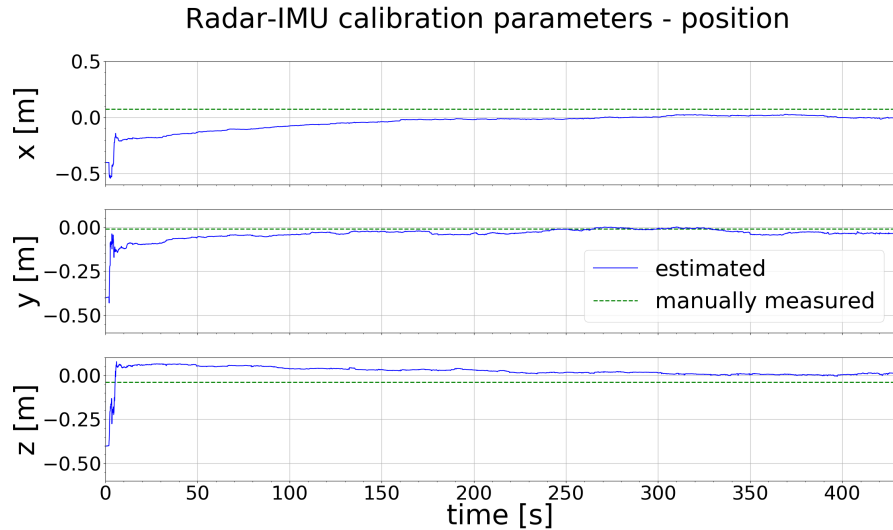


Figure 4.33: Convergence of the translation extrinsic calibration parameters for the system with extremely high initial calibration errors. Green dashed lines are used to mark the manually measured extrinsic calibration parameters values which we consider the ground truth.

Table 4.5: Metrics computed across closed-loop flights

Trajectory	Distance [m]	Norm of MAE at full distance [m]	Final drift [%]
1	28.43	0.64	3.41
2	28.88	0.37	2.05
3	28.55	0.73	3.07
Average	<b>28.62</b>	<b>0.58</b>	<b>2.84</b>

Table 4.6: Onboard execution timings

Average time [ms]	
IMU processing	Radar processing
1.04	16.97

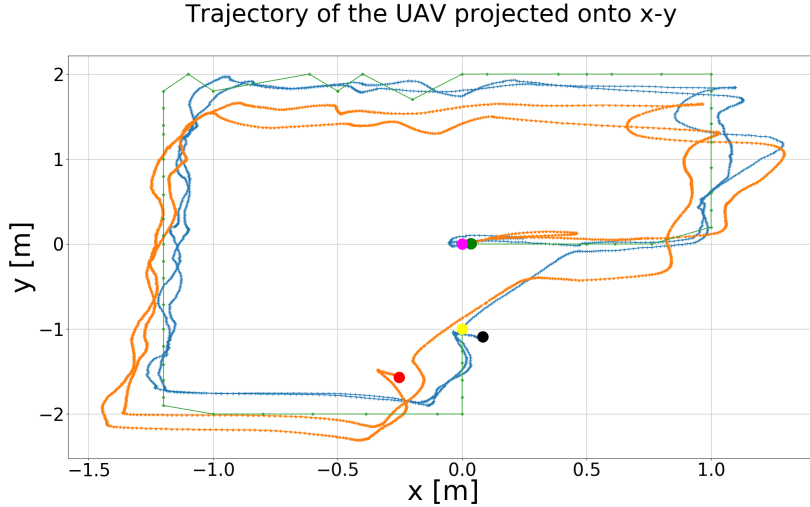


Figure 4.34: Top view of one of the executed closed-loop flights. Marked in blue and orange are the estimated and true trajectories respectively. Plotted in green is the trajectory input to the controller. Coloured dots are the starting and end points. The magenta-coloured dot marks the starting point of the input trajectory, whereas the dots marking the starting points of the ground truth and estimate coincide.

#### 4.3.6 Evaluation of the State Estimation in the Artificial Fog

As depicted in the figure 4.38, we evaluate our estimation framework in dense artificial fog in order to showcase the benefits of the radar-based navigation in visually degraded conditions. To perform the comparison, we moved the UAV seen in the figure 4.38 arbitrarily in a hand-held fashion through a dense artificial fog. We moved the platform manually instead of flying, since as our experiments showed, with the propellers turned on, the amount of the artificial fog we were able to create with the fog machine was quickly dispersed and the evaluation of the impact of the fog became impossible. We further compare the performance of our RIO to a state-of-the-art EKF-based VIO implementation, *OpenVINS* [32]. For VIO, a Matrixvision mvBlueFOX-MLC USB2.0 camera is mounted rigidly next to the radar sensor (seen in the Fig. 4.38) providing images at 20 Hz. For closed-loop computation performance reasons, the VIO is post-processed offline on the desktop hardware described in the section 4.3.3.

Sequence of the results produced by the feature tracker of OpenVINS is shown in figure 4.36. As expected, the tracker struggles to find sufficient

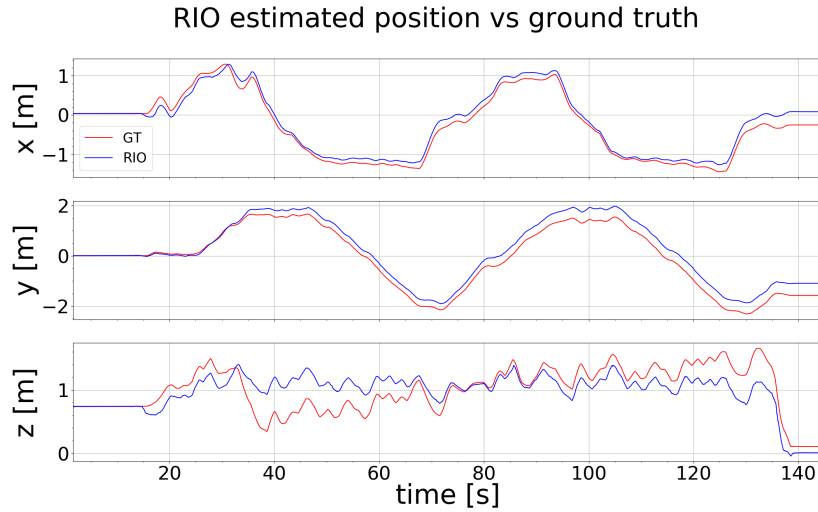


Figure 4.35: Position coordinates of the true and estimated trajectories plotted against time for one of the closed-loop flights. The take-off and landing points were not on the same plane which causes vertical shift in the  $z$  coordinate. Note that no special handling in the filter is needed in the steady initial phase when the robot does not move since no feature triangulation is required but direct depth information is provided by the radar – an important advantage over vision based approaches.

features and to track the few found ones correctly.

The performance of the two approaches is shown in figure 4.37. VIO diverges almost immediately when the vehicle starts moving as it cannot track features correctly in the dense fog. In comparison, our RIO framework successfully continues to estimate the robot pose despite the fog since the radar waves can penetrate it. Thus, in environments such as dense fog, darkness or strong light our RIO approach can be successfully used to estimate the vehicle states correctly and thus be employed to close the feedback control loop in autonomous flights in settings such as disaster zones.

### 4.3.7 Conclusions

In this section we presented a tightly-coupled and real-time capable EKF RIO method which builds upon the approach presented in section 4.2 but effectively leverages multi-state and persistent landmarks aspects from the vision community enhanced for the noisy, inaccurate, and sparse radar signals. In the presented framework, for correcting the drift of the IMU, during the update step we exploit lightweight and inexpensive FMCW radar dis-

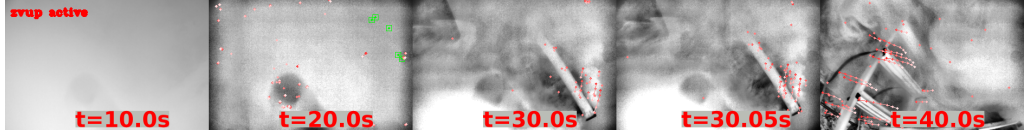


Figure 4.36: Sequence of the images used by the VIO framework OpenVINS for tracking features and state estimation. Due to the fog, features can barely be tracked in the first 30 seconds. Thus, OpenVINS struggles to keep track of persistent features (marked in green) and to perform proper state estimation.

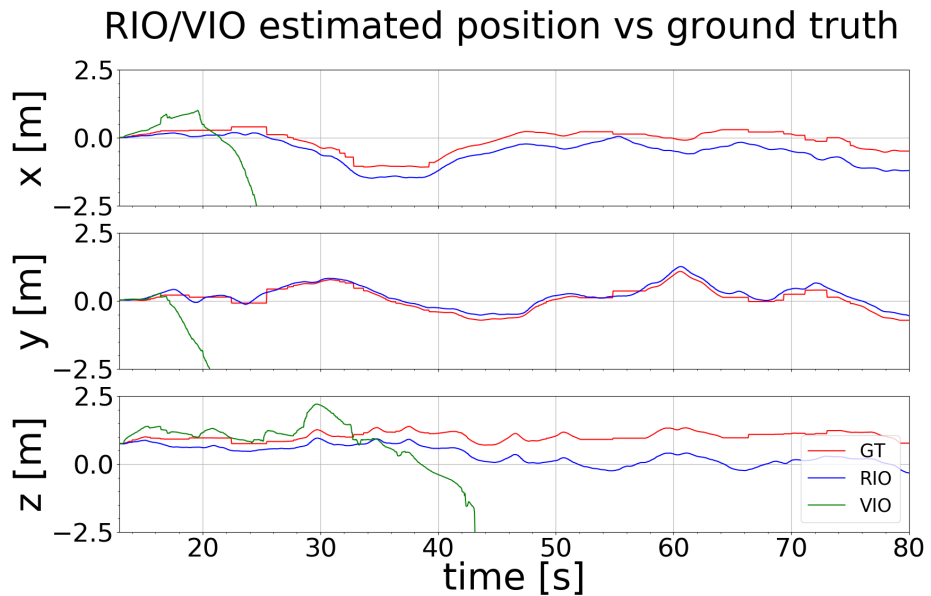


Figure 4.37: Comparison of position estimates of a VIO implementation [32] and our RIO approach. Note the almost immediate divergence of the VIO when faced with the dense artificial fog. As can also be seen, our RIO method proves to be robust against it.



Figure 4.38: Experimental platform used in this work with the FMCW radar and camera sensors placed in the take-off position in dense artificial fog used to simulate a disaster site conditions. Note that the camera has been used only for comparison with VIO in the experiments with the artificial fog (see the section 4.3.6).

tance measurements to 3D points taken at several time instants in the past, distance measurements to persistent landmarks as well as Doppler velocity measurements. It is important to note that in our design we exploit the distance to 3D points to build residuals as opposed to just using 3D point locations, this is dictated by the observation that range (distance) measurements are very accurate in FMCW radars. We showed in real-world flight experiments that our method exhibits solid improvements over state-of-the-art in terms of accuracy and that it has execution times suitable for real time control. Indeed, closed-loop experiments showed that our method scales well towards commonplace issues related to real-time onboard operation of state estimation frameworks on resource-modest platforms such as sporadic measurement losses due to CPU load spikes. We also showed how the online calibration impacts the accuracy and the consistency of our state estimator.

It is to be noted that as opposed to the VIO approaches, in our method the metric scale is directly observable thanks to the radar sensing principles (see chapter 3). Hence, no special initialization involving acceleration excitation is needed as in VIO [66]. This is advantageous since it renders the whole system easier to use.

Moreover, the presented odometry approach makes no assumptions on the environment and can be deployed in GNSS-denied settings. Additionally, given the employed sensor suite it is largely unaffected by conditions deemed challenging for other sensors used in UAV navigation, thus making it promising for applications such as search and rescue operations.

## 4.4 Conclusions

In this chapter we presented our progressive research on EKF-based RIO. We started with a proof-of-concept environment-bound version where strongly reflective anchors whose position in space is known beforehand are used. We progressed towards a two-frame RIO where shifting to more powerful radar sensor allowed us to utilize the 4D radar point clouds to form residuals both on the Doppler velocities as well as feature distances. Finally, inspired by the approach in [58], we added support for several past frames, persistent features and online extrinsic calibration. We demonstrated our final approach in closed-loop flights and also in unfavorable environmental conditions.

The contents presented in this chapter put together into the final multi-state estimator bring the state-of-the-art in RIO close to the state of VIO thanks to the elements like persistent features, multi-state constraints update, and online extrinsic calibration. Remarkably, the achieved accuracy is similar to that obtained with VIO, with the added inherent benefits of the radar sensor in harsh environments which incapacitate cameras. All in all, the presented approach is highly performant and complimentary to VIO.

Since leveraging the features from VIO brings benefits to the RIO EKF framework, it seems purposeful to use the same elements to implement a RIO estimator using the factor graph formalism to still boost the overall performance. This research avenue will be explored in the following chapter.

# CHAPTER 5

---

## Radar-Inertial Odometry Using Factor Graphs

*The present chapter contains results that have been peer-reviewed and published in the IEEE/RSJ International Conference on Intelligent Robots and Systems (IROS) [55].*

In this chapter, we present a novel RIO method based on the nonlinear optimization of factor graphs [20] allowing the estimation of the full 6DoF state of a small UAV using only IMU sensor and a light-weight, inexpensive, low-power Texas Instruments AWR1843BOOST FMCW SoC radar (see figure 5.1) in unknown and unprepared environments. The optimization problem underlying the state estimation task is maintained computationally tractable in real-time by employing a sliding window of states with the partial marginalization of oldest states using the Schur Complement technique. In our formulation we construct tightly-coupled radar factors from the distances to the 3D points matched between subsequent radar scans, instantaneous relative (Doppler) velocities and the distances to persistent landmarks. Tight coupling allows the construction of factors from single measurements, thus bypassing the necessity of computing pose increments from noisy and sparse radar point clouds using a method such as ICP, which in such case is prone to fail [7]. In an attempt to make an exact *one-to-one* comparison with the state-of-the-art multi-state EKF-based RIO approach in section 4.3, we implement both methods in a single custom C++ framework where all front-end features such as point matching, measurement trails construction, velocity-based point pruning based on RANSAC etc. are shared with only estimation back-ends changing. To our knowledge it is the first such comparison of these two common estimation

back-ends in the RIO context.



Figure 5.1: Experimental platforms used in this work. CNS-UAV on the left and DLR's ARDEA-X on the right. The red chip mounted at  $45^\circ$  inclination on each platform is the TI AWR1843BOOST FMCW radar, which outputs highly noisy and sparse 4D pointclouds (3D points and Doppler velocities).

### 5.0.1 Estimator Overview

In our RIO approach at every iteration of the estimator an optimization problem is formulated as a nonlinear factor graph over a sliding window of  $N$  successive IMU states corresponding to time instants at which radar measurements were taken and a set of  $L$  persistent landmarks. We define the state variables of our system as follows:

$$\begin{aligned} \mathbf{x}_{\mathcal{I}} &= \left[ {}^G \mathbf{p}_I; {}^G \bar{\mathbf{q}}_I; {}^G \mathbf{v}_I; \mathbf{b}_a; \mathbf{b}_\omega \right] \\ \mathbf{x}_{\mathcal{L}} &= \left[ {}^G \mathbf{p}_L \right] \\ \mathbf{X} &= \left[ \mathbf{x}_{\mathcal{I}_1}; \dots; \mathbf{x}_{\mathcal{I}_N}; \mathbf{x}_{\mathcal{L}_1}; \dots; \mathbf{x}_{\mathcal{L}_M} \right] \end{aligned} \quad (5.1)$$

with the IMU state  $\mathbf{x}_{\mathcal{I}}$  and a state of a persistent landmark  $\mathbf{x}_{\mathcal{L}}$ .  ${}^G \mathbf{p}_I$ ,  ${}^G \mathbf{v}_I$ , and  ${}^G \bar{\mathbf{q}}_I$  are the position, velocity, and orientation of the IMU/body frame  $\{I\}$  with respect to the navigation frame  $\{G\}$ , respectively.  $\mathbf{b}_\omega$  and  $\mathbf{b}_a$  are the measurement biases of the gyroscope and accelerometer, respectively.  ${}^G \mathbf{p}_L$  define the position of a persistent landmark  $\mathcal{L}$  with respect to the navigation frame  $\{G\}$ .  $\mathbf{X}$  is the set of all states contained within a single sliding window. In order for the optimizer to solve the problem we must compute the jacobians of observation models with respect to the error-state which we define as follows:

$$\begin{aligned}\tilde{\mathbf{x}}_{\mathcal{I}} &= \left[ {}^G\tilde{\mathbf{p}}_I; {}^G\tilde{\boldsymbol{\theta}}_I; {}^G\tilde{\mathbf{v}}_I; \tilde{\mathbf{b}}_a; \tilde{\mathbf{b}}_\omega \right] \\ \tilde{\mathbf{x}}_{\mathcal{L}} &= \left[ {}^G\tilde{\mathbf{p}}_L \right]\end{aligned}\quad (5.2)$$

For translational components, e.g., the position, the error is defined as  ${}^G\tilde{\mathbf{p}}_I = {}^G\hat{\mathbf{p}}_I - {}^G\mathbf{p}_I$ , while for rotations/quaternions it is defined as  $\tilde{\mathbf{q}} = \hat{\mathbf{q}}^{-1} \otimes \bar{\mathbf{q}} = [1; \frac{1}{2}\tilde{\boldsymbol{\theta}}]$ , with  $\otimes$  and  $\tilde{\boldsymbol{\theta}}$  being quaternion product and small angle approximation, respectively.

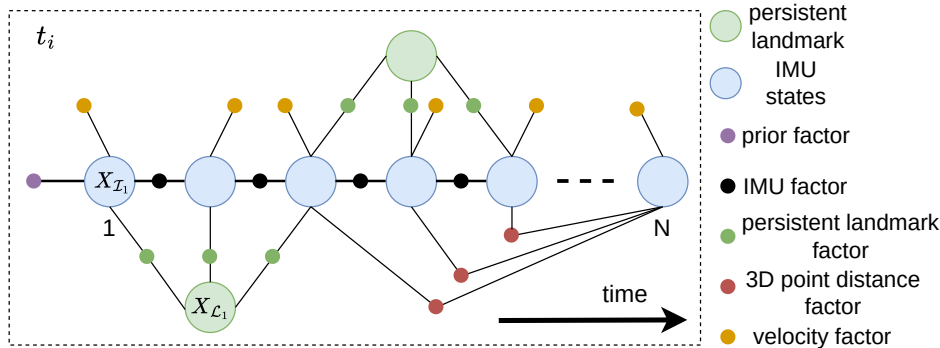


Figure 5.2: Snapshot of the sliding window of states and measurements and the corresponding factor graph. Note the tightly-coupled nature of the graph, in which single measurements corresponding to Doppler velocities of 3D points, matched 3D points between radar scans and matched persisted landmarks are used to construct each factor. The tight coupling allows for maximal exploitation of sensor information. Note that the number of factors in the graph is only illustrative - in a real graph in our system there are many more factors involved.

We depict the representation of a single factor graph corresponding to one sliding window of states in the Fig. 5.2. The edges in the graph represent factors and nodes the estimated states. Each time a new radar measurement is received we form a new graph and solve it to obtain the estimate of  $\mathbf{X}$ . To accommodate the new IMU state in the graph, we first marginalize out the oldest one and use it to form the new prior (see section 5.0.3). We populate the new graph with factors corresponding to the IMU states which remained after the marginalization and the persistent landmarks seen from them. Then, we initialize all states in the window  $\mathbf{X}$  with their previous solutions. The new IMU state in  $\mathbf{X}$  is initialized from the last IMU state in the previous solution by applying the delta-motion from the pre-integrated

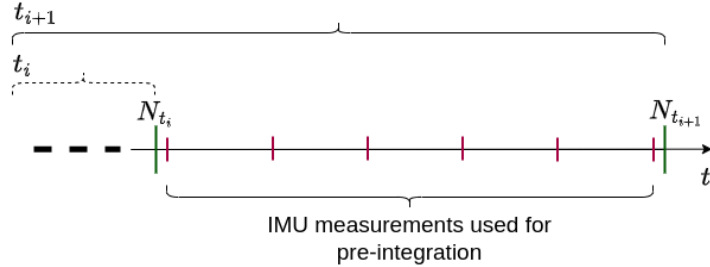


Figure 5.3: Initialization of the newest IMU state in the sliding window. Dashed and solid overbraces mark the sliding window before and after the shift forwards which occurs upon acquiring a new radar measurement (green vertical lines). The new IMU state  $\mathbf{x}_{I_N}(t_{i+1})$  in the window will be initialized with the prediction from the previous solution  $\mathbf{x}_{I_N}(t_i)$  using the pre-integrated new IMU measurements (marked with red vertical lines) between the time instants of the previous and the current radar measurements.

IMU measurements from the timespan between the previous measurement (corresponding to the last estimated state) and the current one (see figure 5.3). We solve the graph using Levenberg-Marquardt algorithm with the GTSAM package [19].

The overall cost function for the proposed factor graph is as follows:

$$\mathbf{X}^* = \underset{\mathbf{X}}{\operatorname{argmin}} e_I + e_P + e_D + e_V + e_L \quad (5.3)$$

where,  $e_I$ ,  $e_P$ ,  $e_D$ ,  $e_V$ ,  $e_L$  are the cost contributions from all of the IMU pre-integration, prior, radar 3D distance, velocity, persistent landmarks factors present in the graph, respectively.

### 5.0.2 Factors

In factor graph formulations, factors represent probabilistic constraints on the variables involved in the estimation and are obtained from measurements or prior knowledge. To define a factor we typically define a probabilistic measurement model constraining a subset of the state variables and upon creation, supply the corresponding measurement. Moreover, for solvers using the "*lift-solve-retract*" paradigm [30] we must provide a jacobian of the model with respect to the error-state defined in the tangent space of the state manifold. In figure 5.2, we show all types of factors included in our factor graph approach. IMU pre-integration factor constrains two estimated IMU states and we construct it from all the IMU measurements obtained between the two constrained states. Using IMU pre-integration

factor is necessary since the IMU measurements come at high frequency and not pre-integrating them would lead to a huge number of variables in the optimization. We use the factor formulated in [30].

Our tightly-coupled relative velocity factor is a unary factor, which means that it introduces constraints on the subset of the variables in only one IMU state. Hence, in the figure 5.2 these factors have connections only to one node representing the state at which the velocity measurements were taken. As seen in the equation (5.4), the constrained state variables are  ${}^G\bar{\mathbf{q}}_I$  and  ${}^G\mathbf{v}_I$ . The factor expresses the projection of the current robot ego-velocity transformed into the radar frame onto the direction vector pointing towards the corresponding 3D point:

$${}^R\mathbf{v}_{P_i} = -\frac{\mathbf{r}^\top}{\|\mathbf{r}\|} \left( {}^I\mathbf{R}_R^\top {}^G\mathbf{R}_I^\top {}^G\mathbf{v}_I + {}^I\mathbf{R}_R^\top ({}^I\boldsymbol{\omega} \times {}^I\mathbf{p}_R) \right) \quad (5.4)$$

where  $\mathbf{r} = {}^R\mathbf{p}_{P_i}$  is the 3D point detected in the current scan,  ${}^I\boldsymbol{\omega}$  is the current angular velocity of the IMU in the IMU frame, and  ${}^G\mathbf{v}_I$  is the current linear velocity of the IMU in the navigation frame. In order to reject outliers, we use dynamic covariance scaling (DCS) robust kernel function [1] in this factor.

In order to further constrain the graph variables and make maximal use of the rich information provided by the radar, we build tightly-coupled factors for persistent landmarks and 3D point distance measurements organized in measurements trails. As we aim at an exact *one-to-one* comparison with the method in section 4.3, we use the exact same code for 3D point matching, obtaining measurement trails and persistent landmarks as in the chapter chapter 4.

We construct 3D point distance factors from a set of point trails which contain a history of continuous detections of the same 3D points (see section 4.3 for details). For all points in a trail we use the IMU states to transform all points  ${}^R\mathbf{p}_{P_j}^{t_p}$  from the trail history at time instance  $t_p$ , where  $p = 1, \dots, V$  and  $V$  is the length of the matched trail, to the current radar reference frame:

$${}^R\mathbf{p}_{P_j}^{t_p} = {}^I\mathbf{R}_R^\top \left( -{}^I\mathbf{p}_R + ({}^G\mathbf{R}_I^{t_c})^\top \left( -{}^G\mathbf{p}_I^{t_c} + {}^G\mathbf{p}_I^{t_p} + {}^G\mathbf{R}_I^{t_p} ({}^I\mathbf{p}_R + {}^I\mathbf{R}_R {}^R\mathbf{p}_{P_j}^{t_p}) \right) \right) \quad (5.5)$$

where  ${}^I\mathbf{R}_R$  and  ${}^I\mathbf{p}_R$  is the constant pose (orientation and position) of the radar frame with respect to the IMU frame.  ${}^G\mathbf{R}_I^{\{t_c, t_p\}}$  and  ${}^G\mathbf{p}_I^{\{t_c, t_p\}}$  are the IMU orientation and position corresponding to the trail history element

at time  $t_p$  and current radar scan at  $t_c$ , with respect to the navigation frame  $\{G\}$ . For factor construction we use the distance to the transformed matched point:

$$d_{P_j} = \left\| {}^R \mathbf{p}_{P_j}^{t_p} \right\| \quad (5.6)$$

where  $d_{P_j}$  is the distance to a single point  $j$  in the matched trail history  ${}^R \mathbf{p}_{P_j}^{t_p}$  at  $t_p$  aligned to the current radar pose at  $t_c$ .

We also use persistent landmarks to build factors which introduce constraints between the landmarks and the IMU states from which these landmarks have been seen (figure 5.2). Promotion of trails with sufficiently long history detection to persistent landmarks is described in details in section 4.3. Measurement model used in the factor is:

$$\mathbf{l}'_m = {}^R \mathbf{p}_{L_m} = {}^I \mathbf{R}_R^\top ({}^G \mathbf{R}_I^\top (\mathbf{l}_m - {}^G \mathbf{p}_I) - {}^I \mathbf{p}_R), \quad (5.7)$$

$$d_{\mathbf{l}_m} = \left\| \mathbf{l}'_m \right\| \quad (5.8)$$

As for the velocity factor, for both 3D points and persistent landmark factors, we use DCS for outlier rejection. Compared to the chi-squared-based outlier rejection in section 4.3, using the DCS does not remove the factors judged as out-of-distribution based on their residuals, only down-weigh them.

All 3D points delivered by radar and used for constructing factors are pruned for outliers using RANSAC similarly to [23].

### 5.0.3 Partial Marginalization

As the robot evolves in its environment, new IMU states and persistent landmarks are being added to the state vector. Nonetheless, to keep the state estimation task computationally feasible, we must bound the number of variables in the underlying optimization problem. Hence, upon the addition of new states we must remove the oldest ones by marginalizing them out. In our system we achieve marginalization with the Schur Complement technique (see figure 5.4). Namely, when forming a new graph upon obtaining a new radar measurement, due to conditional independence [46], we consider a sub-graph containing only the states to be marginalized out and the states connected to these states (sometimes called *Markov blanket*). We linearize the resulting sub-graph around the previous solution (current estimate) to obtain its hessian matrix and gradient vector:

$$\begin{bmatrix} \mathbf{H}_{\mu\mu} & \mathbf{H}_{\mu\lambda} \\ \mathbf{H}_{\lambda\mu} & \mathbf{H}_{\lambda\lambda} \end{bmatrix} \begin{bmatrix} \tilde{\mathbf{x}}_\mu \\ \tilde{\mathbf{x}}_\lambda \end{bmatrix} = \begin{bmatrix} \mathbf{b}_\mu \\ \mathbf{b}_\lambda \end{bmatrix} \quad (5.9)$$

Where  $\mu$  and  $\lambda$  denote the sets of states to marginalize out and states connected to those states, respectively. We calculate the Schur Complement of the states to marginalize out in the hessian and the corresponding gradient:

$$\begin{aligned} \mathbf{H}_{\lambda\lambda}^* &= \mathbf{H}_{\lambda\lambda} - \mathbf{H}_{\lambda\mu} \mathbf{H}_{\mu\mu}^{-1} \mathbf{H}_{\mu\lambda} \\ \mathbf{b}_\lambda^* &= \mathbf{b}_\lambda - \mathbf{H}_{\lambda\mu} \mathbf{H}_{\mu\mu}^{-1} \mathbf{b}_\mu \end{aligned} \quad (5.10)$$

and use the resulting matrix and vector to form the new prior factor.

It is important to note that the marginalization allows for retaining the information from residuals that depend on the removed variables, nevertheless during optimization the linearization points of the marginalized out variables are not updated. Similarly, variables within the Markov blanket do not get their linearization points updated in order not to destroy the nullspaces of the respective Jacobian matrices which would otherwise introduce inconsistencies [21]. As noted in [66] early fixing of the linearization points may result in suboptimal estimates. Since the current marginalization prior will be utilized to calculate the subsequent prior, the linearization points of the marginalized out variables will remain in the prior for the time the estimator operates, as opposed to filtering approaches, which are able to perfectly marginalize out old variables.

## 5.1 Results

### 5.1.1 Experimental Setups

We perform real-world experiments with two different platforms (figure 5.1) to demonstrate our RIO method on different systems. One of the platforms (CNS-UAV) is described thoroughly in section 4.3. The other one is the ARDEA-X UAV designed and built from ground up at the German Aerospace Center's (DLR) Institute of Robotics and Mechatronics. The system was designed for autonomous exploration of unknown regions in the context of planetary space robotics. An Intel NUC for higher-level and a Pixhawk for lower-level tasks make up ARDEA's two primary navigational components. The radar module is connected to the Intel NUC. The IMU data is obtained from the Pixhawk. On both platforms the same SoC FMCW radar chip is mounted (Texas Instruments AWR1843) and configured in the same way (as in section 4.3). We gather datasets with each

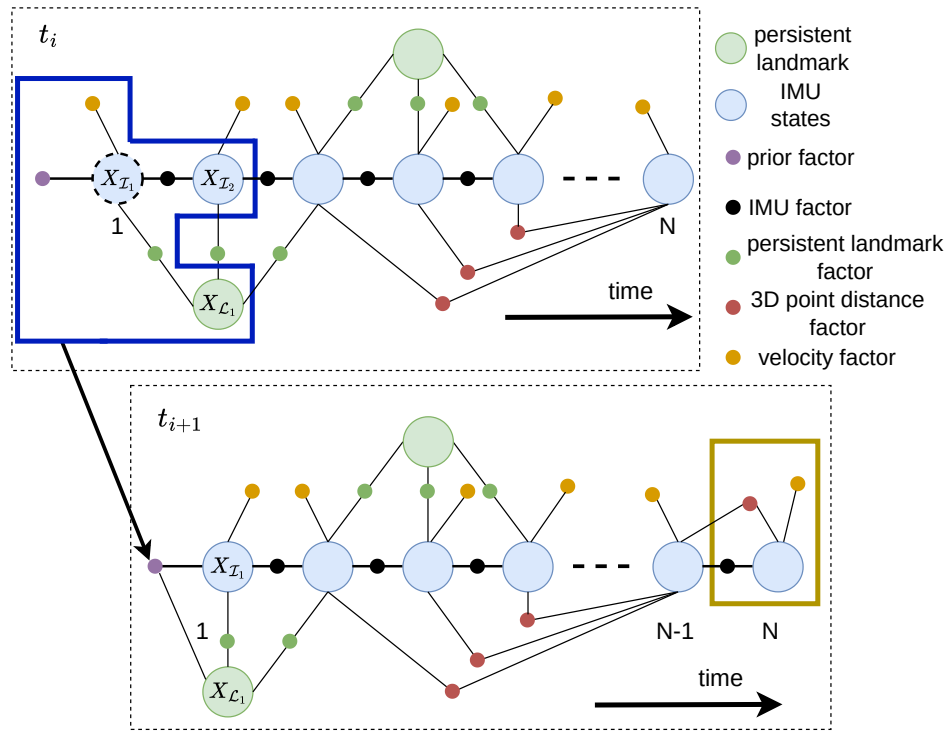


Figure 5.4: Depiction of the marginalization of the oldest IMU state (circle with dashed black line). Sub-graph (marked with the blue rectangle) is formed from the state to marginalize out and the states it is connected to (*Markov blanket*). We linearize the sub-graph and in the obtained Gauss-Newton system of equations we apply the Schur Complement to the marginalized out variables to form the new prior factor. Newly added states and factors are marked with the yellow rectangle. Note that the indices adjust in the window from time  $t_i$  to  $t_{i+1}$  (e.g.,  $\mathbf{x}_{I_k}(t_i)$  becomes  $\mathbf{x}_{I_{k-1}}(t_{i+1})$ ) as we only keep a maximum of  $N$  IMU states.

platform in which we record the ground truth trajectories using motion capture system and sensor readings from the IMU and radar. In the case of ARDEA-X we record the EKF RIO estimates computed onboard. For CNS-UAV both factor graph and EKF are executed offline on the recorded sensor data on an Intel Core i7-10850H vPRO laptop with 16 GB RAM in a custom C++ framework compiled with gcc 9.4.0 at -O3 optimization level. In the case of CNS-UAV, for both factor graph and EKF RIO we manually calibrate the extrinsic parameters between the IMU and the radar. In the case of the ARDEA-X, for EKF RIO these parameters are estimated online. Both estimators use exactly same front-end parameters and in both cases the sliding window size is set to  $N = 10$ . Execution time for our factor graph RIO on the above mentioned desktop PC is 16.15 ms on average which proves its real-time capability. Compared with 2.15 ms (propagation and update) for the EKF RIO in section 4.3 the latter is (as expected) performing better.

### 5.1.2 Evaluation

We use the data recorded with the two platforms described in section 5.1.1 for evaluation of our factor graph RIO approach and for comparison with the EKF RIO method from section 4.3. With each of the platforms we create a dataset of several flown trajectories (five in case of ARDEA-X and three in case of CNS-UAV). Within the CNS-UAV dataset the trajectories are not pre-planned, manually flown, are between 150 m - 175 m long and include pronounced motions in all three dimensions. ARDEA-X dataset contains two pre-planned waypoint-based and three not pre-planned manually flown shorter trajectories. Sample trajectories from each dataset can be seen in the figure 5.5. For every flight in each dataset we compute the norm of the RMSE of position together with the mean and standard deviation of the RMSE values (see table 5.1). Our comparison shows that both methods perform similarly on average as seen in the table 5.1. This is perhaps a counter-intuitive conclusion since the optimization of factor graphs is often considered to provide superior accuracy thanks to successive linearizations performed during the optimization. Nevertheless, in the case where the linearization point is well-determined, this advantage turns out not to be the crucial factor in determining the accuracy. Indeed, in the case of our experiments, the system is either initialized with the knowledge of the ground truth, or with its initial pose being the frame of reference for the estimator. Such settings leave very little room for any transient behaviours of the estimator. Thus, diminishing the value added from possible multiple linearizations.

Table 5.1: Norm of RMSE values of position across flights performed with ARDEA-X and CNS-UAV for both methods

ARDEA-X dataset		
Nr	RMSE Norm EKF	RMSE Norm FG
1	0.136	0.213
2	0.083	0.153
3	0.377	0.446
4	0.698	0.711
5	0.265	0.279
Average	<b>0.312</b>	<b>0.360</b>
Std. dev.	<b>0.218</b>	<b>0.200</b>
CNS-UAV dataset		
1	1.417	0.625
2	0.877	1.660
3	1.077	1.008
Average	<b>1.124</b>	<b>1.098</b>
Std. dev.	<b>0.223</b>	<b>0.426</b>

To demonstrate the benefits of iterative linearizations in the factor graphs during transient phases, we initialize both the EKF and the factor graph-based estimators with wrong initial velocity set to  $[2.0, 2.0, 0.0] \frac{m}{s}$  (whereas the true one is equal to  $[0.0, 0.0, 0.0] \frac{m}{s}$ ). In the Fig. 5.9 we show that in both cases when we do, and do not account for the wrong velocity initialization in the initial covariance, the factor graph-based approach always outperforms the EKF.

In our comparison we note the importance of the front-end in any state estimation system. While both RIO methods perform similarly on average, it turns out that there are qualitative differences between the estimation results of particular UAV trajectories (See figures 5.6 to 5.8). These discrepancies are attributed to different outlier rejection strategies between the EKF and the factor graph-based RIO.

## 5.2 Conclusions

In this chapter we presented a novel tightly-coupled RIO method based on the nonlinear optimization of factor graphs in a sliding window of states and measurements. The used sensor suite is light-weight, inexpensive, low-

3D trajectory of the UAV

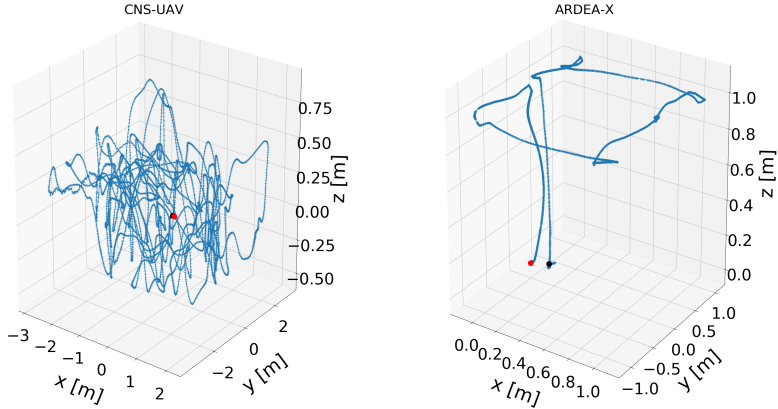


Figure 5.5: Sample trajectories from each dataset with the take-off and landing points marked in red and black respectively. Trajectories collected with the CNS-UAV are not pre-planned, longer and in general more challenging in terms of dynamics.

power and consumer-grade, hence widely accessible. The presented approach is rendered real-time capable thanks to the application of the partial marginalization of oldest states in order to bound the state vector size and form an informative prior for the estimator. We performed a *one-to-one* comparison with a state-of-the-art multi-state EKF RIO method on the in-house datasets collected with two different UAV platforms in order to demonstrate the soundness of our framework. Comparing the two methods reveals that they perform on-par in terms of accuracy when the linearization point is not far from the true state. In terms of CPU load the comparison shows that the EKF RIO is less resource-demanding. We demonstrated the advantages that successive linearizations in the factor graph-based method bring to the convergence of the estimator in transient phases (when the linearization point is far from the true state). We provided this demonstration in both the case when the wrong initialization is, and when it is not reflected in the uncertainty of the initial state (which is often the case in practice). The whole comparison was performed in such way that both EKF and factor graph back-ends were implemented in the same software framework, effectively sharing exactly the same front-end features and parameters. We make the software framework and datasets used in the present

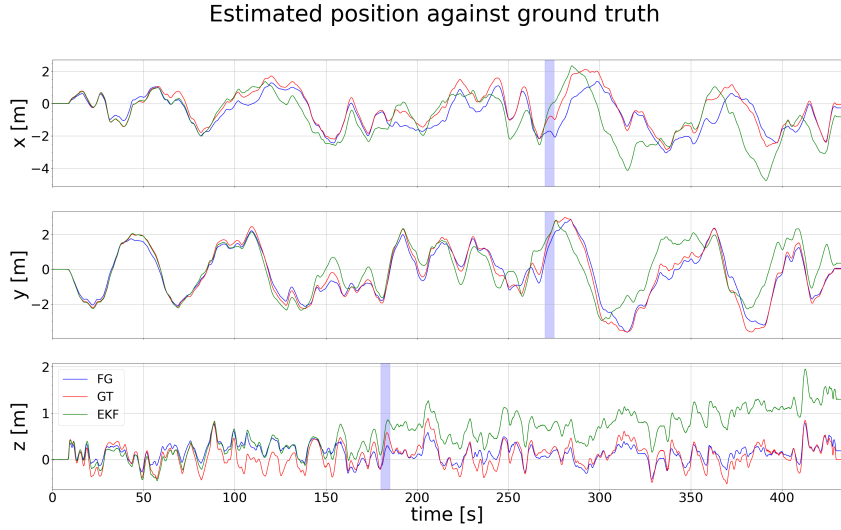


Figure 5.6: Estimated position of the UAV using both methods for the first trajectory from the CNS-UAV dataset. The factor graph-based method performs visibly better with the norm of RMSE less than the half of the corresponding RMSE value for the EKF-based method. The thin shaded regions mark points in time where the EKF-based estimator started acquiring very heavy drift due to outliers.

paper open-source in order to facilitate further research and comparisons.

The results in this chapter and in the recent research in [15] lead to an important question. Namely, *do we need iterations in state estimators?* The accuracy comparison shows that on average, in nominal conditions, that is, when the linearization point is not far from the true state, the iterations within the factor graph bring no added value and are rather a waste of computational resources, since the accuracy attained with factor graph is comparable to non-iterated EKF. The picture changes when disturbances from the true state are introduced, in which case the iterations allow faster convergence. It is to be noted that there exists a growing body of research within the area of equivariant filters which exhibit remarkable convergence properties without iterations [28].

Another interesting open research question appears when comparing the uncertainty representation in both EKF and factor graph formulation and its potential impact on the accuracy on consistency of the estimation. Namely, when calculating the prior factor using the Schur complement technique, as far as the cross-correlations between the IMU poses in the sliding

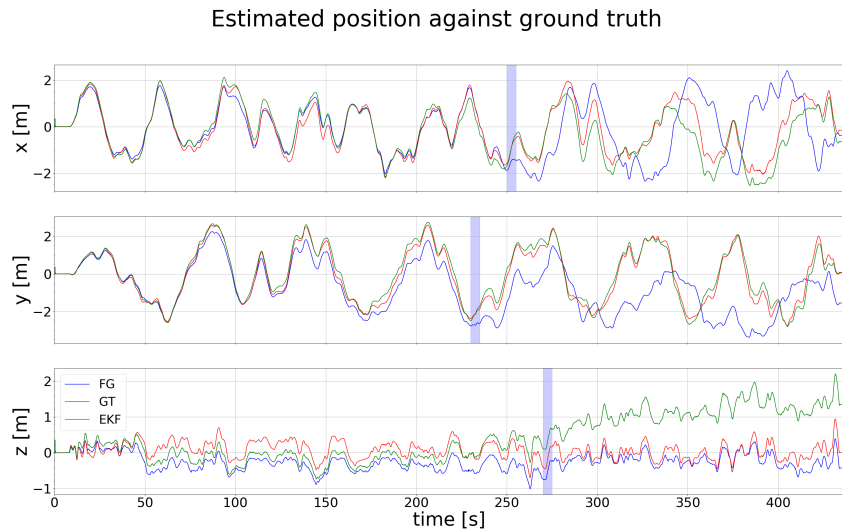


Figure 5.7: Estimation results for the position of the UAV using both methods for the second trajectory from the CNS-UAV dataset. Thin shaded regions are marked as areas where the estimators failed to reject outliers. This resulted in major degradation of the accuracy. We see that in the first two sub-plots factor-graph based method acquires very strong yaw drift (x and y axes seem swapped) from which it does not recover. For the EKF the concentration of the outliers in the marked region in the third sub-plot results in a strong vertical drift.

window are concerned, from one optimization run to another, only cross-terms between the marginalized pose and the one next to it are considered in the prior Hessian matrix. All other poses have no cross-terms unless a landmark seen from them has been marginalized out. This is strikingly different from the multi-state filter approach where stochastic cloning introduces cross-terms in the covariance matrix between the IMU poses within the maintained estimation window.

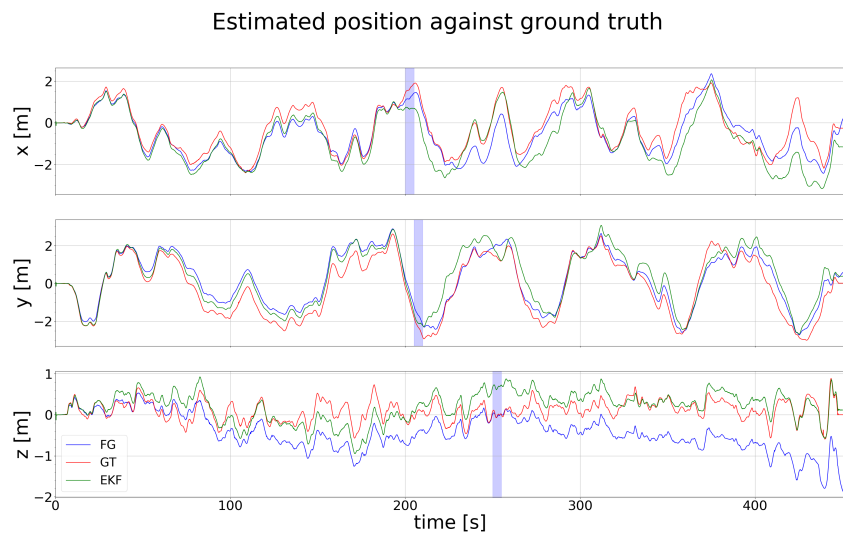


Figure 5.8: Plot of the estimates of position of the UAV using both methods for the third trajectory from the CNS-UAV dataset. In this case both estimators perform on-par in terms of RMSE with the outliers affecting the vertical drift for the factor graph-based estimator and  $x, y$  coordinates for the EKF-based one.

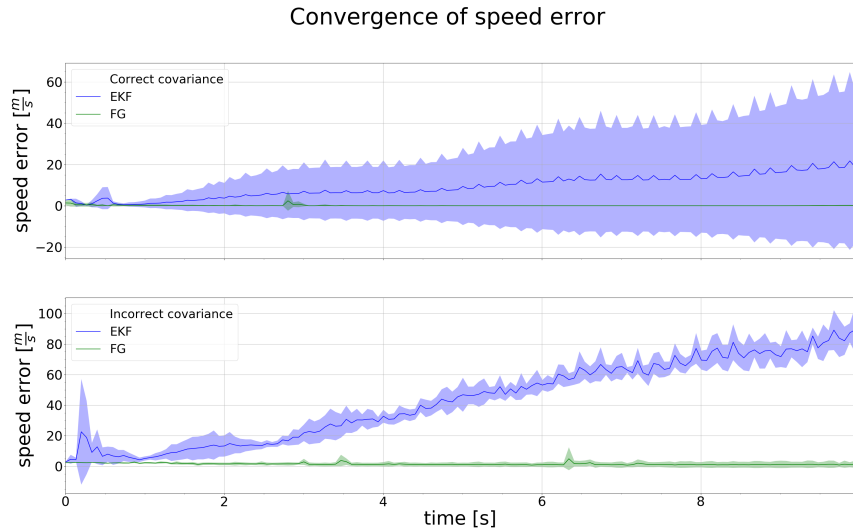


Figure 5.9: Plot of convergence of the mean of errors in speed (norm of the velocity) in the case of incorrect velocity initialization for both methods. The mean is taken across the whole ARDEA-X dataset during the first 10 s of the data recording when the UAV stands still on the ground before the take-off. In the upper sub-plot, we initialize incorrectly the velocity, yet we account for this uncertainty by setting accordingly large corresponding covariance entries. The factor graph approach is unaffected and converges quickly to the correct value ( $0 \frac{m}{s}$ ), whereas the EKF never reaches convergence. In the lower sub-plot, for the same wrong initialization, we do not adjust the covariance settings, effectively misleading the estimator into believing it is initialized correctly. In this case the EKF diverges catastrophically, while factor graph approach still converges although to a slightly offset value. Shaded regions denote the  $1\sigma$  bounds of the plotted means.

# CHAPTER 6

---

## Sparse And Noisy 3D Radar Point Cloud Matching Using Deep Learning

*The present chapter contains results that have been peer-reviewed and accepted to the IEEE/RSJ International Conference on Intelligent Robots and Systems (IROS) in Hangzhou, China (2025) [57].*

As demonstrated in the previous chapters, using 3D point correspondences is vital for state estimation using RIO systems. There exist well-established method for this task yet they prove unsuitable when the quality of the point clouds drops, as is the case of many FMCW radar sensors. In this chapter we present a novel learning framework for predicting robust point correspondences between FMCW SoC radar 3D point clouds in RIO estimation. Our framework is inspired by recent advances in deep learning for dense 3D point clouds processing in [33, 79] and tailored for the sparse and noisy radar measurements.

### 6.1 Learning 3D Point Correspondences In Radar 3D Point Clouds

We base our network architecture on the one defined in [79] for registration of dense and noiseless 3D point clouds of shapes, and adapt it to our setting of learning correspondences in variable-length, sparse and noisy SoC radar 3D point clouds. In particular, our framework consists of the following steps (figure 6.1):

1. Calculate the input embeddings in a *per-point* manner for each of the two consecutive input point clouds using the *PointNet* architecture [14].
2. Use two transformer [77] sub-networks to predict a matrix whose rows and columns correspond to the points in the first and second input point clouds, respectively, and whose entries express the degree of likelihood that the corresponding row and column form a match.
3. Solve the linear sum assignment (LSA) optimization problem on the predicted matrix to find the set of point correspondences, where each item contains the index into the first (row) and second (column) point cloud.
4. During training, cast the problem into a multi-label classification setting by considering the column index from the LSA solution the class label of a point in the second point cloud, which allows leveraging the cross-entropy loss function.
5. During inference, apply acceptance and FOV thresholds to the set of matches found in step 3 to form the output.

We train and test our network on a real-world, self-collected dataset consisting of 13 manually and autonomously flown UAV trajectories from which we select 8 for training and 5 for testing. To make the validation more thorough and comparable, we also test our approach with the public Coloradar dataset [41]. Evaluation of our method in an open-source state-of-the-art EKF-based RIO framework from section 4.3 (which does not use a learning-based matching algorithm to find 3D point matches) shows an increase in estimation accuracy by over 14 % for the self-collected dataset and by 19 % for the Coloradar dataset, in terms of position RMSE norm. We also note that, when deactivating the Doppler information and only keeping the 3D point matches as correction information for the IMU integration in RIO, we note a difference in accuracy of more than 70 % when using our method on the self-collected dataset. To our knowledge, this is the first framework for learning point correspondences in sparse and noisy 3D point clouds as available from inexpensive SoC radar sensors.

### 6.1.1 Network Architecture

As seen in figure 6.1, the first step in our network applies the *PointNet* sub-network to two consecutive input point clouds to embed them in a

higher-dimensional space. We obtain the input point clouds by finding the length  $N$  of the longest point cloud in our whole dataset and padding all point clouds to that length with zero vectors of size  $1 \times 3$ . We also append a zero vector to the beginning of each point cloud which is necessary to train our network as a multi-label classifier (see section 6.1.2). That way, each of the resulting input point clouds has the shape  $(N + 1) \times 3$ . We apply the embedding sub-network on a *per-point* basis, which means that for a single point in the input represented by three coordinates  $\{x, y, z\}$  we obtain an embedding vector of size  $1 \times E$ , where  $E$  is the chosen embeddings size. *PointNet* parameters are learned and shared among all points in the input. In the next step, we forward the embedded points in each point cloud to two transformer sub-networks. The role of each of the transformers is to compute new embeddings of each point cloud using the contextual information of both point clouds jointly. That way, the network can leverage the attention mechanism on both point clouds together which permits finding the embeddings tailored to the specific kind of point clouds, thus making the embeddings task-specific [79]. Specifically, in each transformer block apart from passing to the decoder the output embeddings of the encoder, we also pass in the other point cloud input embeddings. The final embeddings are calculated by summing the transformer output, which encodes the mutual information about the point clouds, with the initial embeddings. The output of the network is obtained by calculating the dot product of the final embeddings of each point in the first point cloud with the final embeddings of each point in the second point cloud. This operation yields an output matrix of shape  $(N + 1) \times (N + 1)$ . Entries in the output matrix express the affinity between points in each input point cloud, that is, the likelihood that a pair of points form a correspondence.

### 6.1.2 Network Training And Inference

In the case of noisy, sparse and variable-length SoC radar point clouds, we cannot conveniently train the network on the odometry error using the SVD as in [6] and [79]. We thus propose a different approach to calculating the loss in our network. Namely, we treat the index of every point in the point cloud as its class label and reserve the class label (and the index) "0" for any non-matched points. The output matrix of the network is structured as follows,

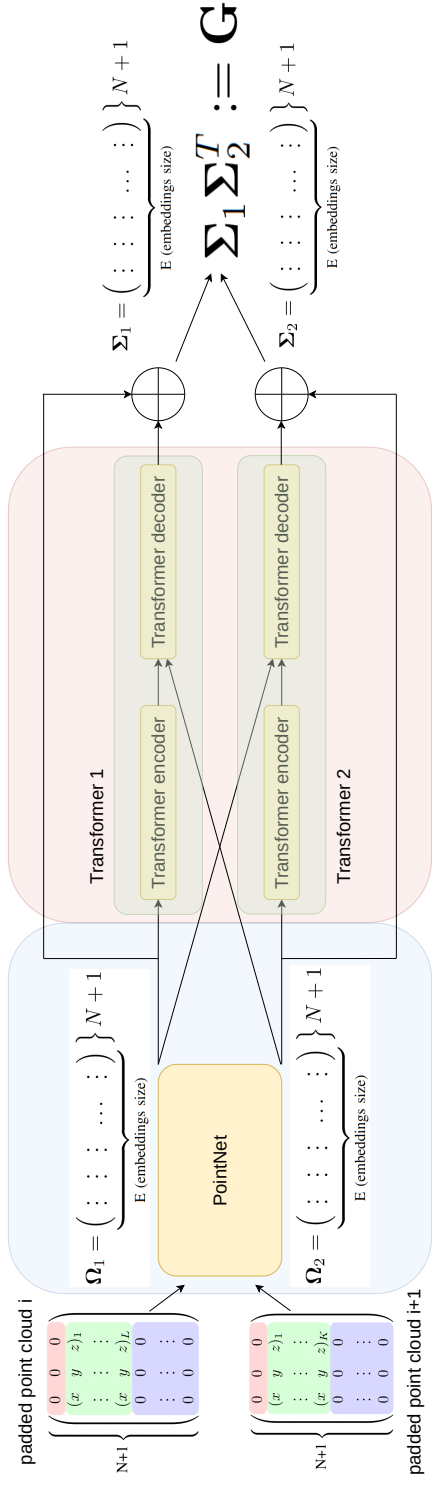


Figure 6.1: Our learning framework is based on the architecture proposed in [79] for dense and structured point clouds registration. We adapted it to our scenario with highly noisy and sparse consumer-grade SoC radar 3D point clouds. Note the zero padding of the input point clouds (section 6.1.2) and the pre-pended "0", which account for the variable-length input and the class label attributed to any point with no match, respectively. Input point clouds are passed to the embedding *PointNet* sub-network (light blue block). Individual embeddings enter the transformer sub-networks (light red block) where the self and the reciprocal attention is computed for each point cloud. Output matrix  $\mathbf{G}$  representing the mutual affinity between points in the input point clouds is obtained by calculating the dot product of the final embeddings. Within the output we search for the set of matches by solving the LSA (see section 6.1.2).

$$\mathbf{G} = \underbrace{\left( \begin{array}{cccccc|cc} \bullet & \bullet & \cdots & \cdots & \cdots & & \bullet & \bullet \\ \bullet & c_{11} & c_{12} & \cdots & c_{1K} & & \cdots & \bullet \\ \vdots & c_{21} & c_{22} & \cdots & c_{2K} & & \cdots & \vdots \\ \vdots & \vdots & \vdots & \ddots & \vdots & & \cdots & \vdots \\ \vdots & c_{L1} & c_{L2} & \cdots & c_{LK} & & \cdots & \vdots \\ \bullet & \vdots & \vdots & \vdots & \vdots & & \ddots & \bullet \\ \bullet & \bullet & \cdots & \cdots & \cdots & & \bullet & \bullet \end{array} \right)}_{N+1} \quad (6.1)$$

and is obtained by taking the dot product of the final embeddings  $\Sigma_1$  and  $\Sigma_2$  of the two consecutive input point clouds as shown in the Fig. 6.1. Entries in row  $i$  express the likelihood that point  $i$  in the first input point cloud is a correspondence to point  $j$  in the second input point cloud, where  $i = 1 \dots L$ ,  $j = 1 \dots K$  and  $L, K$  are lengths of the respective point clouds. Only the green sub-matrix in the output matrix in equation (6.1) carries useful information. All other elements result from adding the "0" (non-matched) class label and from padding the point clouds to equal length with zeros. In particular, appending the zero vector at the beginning of each input point cloud creates the 0-th row and column in  $\mathbf{G}$ . This is crucial during training, since we assign a "0" class (0-th index) in the ground-truth for every point in the first point cloud which does not have a match in the second point cloud.

During inference, since point clouds are usually of different lengths, we solve the LSA problem on the green sub-matrix to find the optimal assignment,

$$\min \sum_{i=1}^L \sum_{j=1}^K \mathbf{C}_{i,j} \mathbf{X}_{i,j} \quad (6.2)$$

Where  $\mathbf{X}$  is a boolean matrix where  $\mathbf{X}_{i,j} = 1$  iff row  $i$  is assigned to column  $j$  and  $L, K$  are lengths of the input point clouds.  $\mathbf{C}$  is the green sub-matrix from equation (6.1). Constraints of the problem are such that each row is assigned to at most one column and each column to at most one row. For each entry in the solution we apply an experimentally chosen threshold to decide whether it is a match or not. LSA is usually solved using Munkres algorithm [60].

During training, the structuring of the network output shown in equation (6.1) allows us to compute the cross-entropy loss between each row

(the index of which is the index of a point in the first point cloud) and the ground-truth label (index of the matched point in the second point cloud or the "0" index for a non-match), as follows,

$$l_n = -\frac{1}{M} \sum_{i=1}^M \log \left( \frac{\exp(\mathbf{G}(p_i, q_i))}{\sum_{j=1}^{N+1} \exp(\mathbf{G}(p_i, q_j))} \right) \quad (6.3)$$

where  $n = 1 \dots B$  and  $B$  is the mini-batch size, and  $(p_i, q_i)$ ,  $i = 1 \dots M$  are the indices of the ground-truth matches in the first and second point cloud, respectively.  $N+1$  is the length of each row (and column) of the  $\mathbf{G}$  matrix.

Preparing the input data and ground-truth labels for training requires pre-processing. In order to generate the ground-truth point correspondences, we use the spatial transformation from the motion capture system between radar frames of every two consecutive radar measurements. Using the spatial information, we transform the 3D points from the first point cloud to the frame of the second point cloud and perform geometric matching by solving the LSA optimization problem as in equation (6.1) but this time on a matrix whose entries are euclidean distances between points in both point clouds expressed in the second point cloud frame, as in,

$$\mathbf{C}_{i,j} = \left\| {}^{R_c} \mathbf{p}_{P_i}^c - \left( {}^{R_c} \mathbf{R}_{R_p} {}^{R_p} \mathbf{p}_{P_j}^p + {}^{R_c} \mathbf{p}_{R_p} \right) \right\| \quad (6.4)$$

where  ${}^{R_{\{p,c\}}} \mathbf{p}_{\{p,c\}}^{\{p,c\}}$  are all points from the previous radar scan at time instance  $t_p$  and from the current radar scan at  $t_c$ , in the previous and current radar frames, respectively.  ${}^{R_c} \mathbf{R}_{R_p}$  and  ${}^{R_c} \mathbf{p}_{R_p}$  are rotation and translation parts of the spatial transform between the current and previous radar frames obtained from the motion capture system. That way, we obtain the ground-truth class labels (indices of matched points in each point cloud). We shift the obtained labels by one to account for the "0" class for every non-matched point. Pre-processing the input radar data consists only of removing the points outside of the FOV of the sensor and aforementioned zero padding.

## 6.2 Results

### 6.2.1 Experiments

In order to train and validate our learning framework, we collect a dataset consisting of 13 UAV trajectories with two different platforms (ARDEA-X and CNS-UAV) described in chapter 5 (see figure 6.3). Both platforms

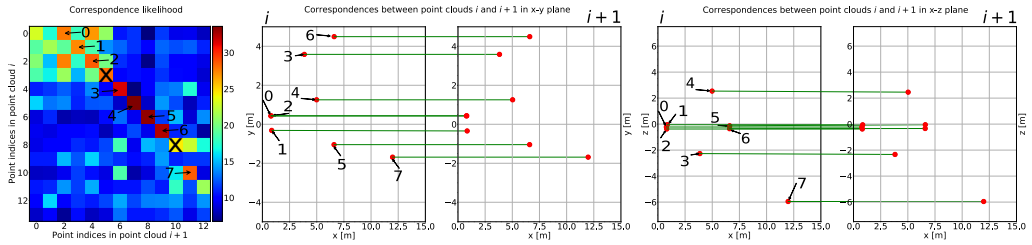


Figure 6.2: Leftmost part of the figure shows the correspondence likelihood matrix (the green part of the  $\mathbf{G}$  matrix in the equation (6.1)) inferred from the learned proposed model for two consecutive point clouds  $i$  and  $i + 1$ . Rightmost and the middle parts show the resulting 3D point correspondences for the same point clouds. Correspondences are shown on  $xy$  (middle sub-plot) and  $xz$  (right sub-plot) planes. Numbers marking the entries in the matrix are consistent with the indices of the matches in sub-plots. During inference, we prune the matches outside the FOV of the radar and with correspondence likelihoods below the empirically found acceptance threshold (shown as "x" in the leftmost plot). Thus, some entries in the matrix have no corresponding matches despite having relatively hot values. Only matched points are shown to not clutter the figure.

use the same consumer-grade TI AWR1843BOOST FMCW SoC radar chip mounted and configured in the same way, as well as the same pixhawk IMU sensor. We record radar and IMU sensor measurements as well as the ground truth pose of the UAV using a motion capture system. We divide this dataset into 8 training and 5 validation trajectories. The training dataset contains trajectories between 150 m - 180 m in length flown manually. The validation dataset contains shorter trajectories between 11 m - 38 m, among which some are manually flown while others are pre-planned, executed using specified waypoints. We also validate our method on five sequences from the public open-source Coloradar dataset [41]. Coloradar sequences are collected using hand-held sensor rig containing the same TI radar chip as ARDEA-X and CNS-UAV platforms. Coloradar sequences contain much more aggressive motion than the self-collected dataset, thus being more challenging. While in three sequences a motion capture system is used as the ground-truth, the other two contain high-precision LIO data. We train our network using PyTorch open-source package. We assess our 3D point matching framework qualitatively in an indirect way by plugging it into an open-source RIO framework from section 4.3 and comparing the accuracy of the obtained estimates to the case when the default (non-learning)

matching algorithm is used. Between executions of the RIO estimator, we only exchange the matching algorithm, all other parameters and settings remain the same. The RIO which we use for validation is EKF-based and in the update step uses three sources of information: 3D point matches, Doppler velocities and persistent features. For the self-collected dataset, we execute the RIO in two configurations: in the default configuration with both Doppler and point matches, and with only point matches enabled in the update step. For the Coloradar we only use default configuration (point matches and Doppler). In all cases, we compile the RIO framework without persistent features in the update. In the case of our learning-based framework, we execute the inference on the learned model in a Python node before feeding it to the RIO. The inference with a non-optimized model takes on average 0.0273 s, which means the optimized implementation would lend itself to real-time use. The non-learning matching algorithm is implemented within the RIO estimator as its default matching algorithm and described in section 4.2. Both RIO and inference node are executed offline on the recorded sensor data on an Intel Core i7-10850H vPRO laptop with 16 GB RAM.

### 6.2.2 Evaluation

For each trajectory from both validation datasets (self-collected and Coloradar), we compute the norm of RMSE of the position and attitude estimates along with the mean and the standard deviation of the obtained values when switching the matching algorithm inside the RIO estimator (see table 6.1 and table 6.2). In the case of the self-collected dataset, we compute the norm of RMSE values in the case when both point matches and Doppler are used, and additionally, when only point matches residuals are used in the update step of the EKF in the RIO. Our comparisons show that when only point matches are used in the update step, which is the most direct way of assessing the performance of our learning-based matching framework, we obtain a striking 70.38 % improvement in the position estimate accuracy on average. When compared to the state-of-the-art configuration of the RIO, that is, with both Doppler and point matches residuals enabled, we obtain a 14.28 % improvement in position accuracy on average. With the Coloradar dataset, we only execute the full configuration containing both Doppler and point matches residuals and obtain 19.01 % improvement in position accuracy on average. The motion in the Coloradar dataset is too aggressive for the configuration using only point matches to work properly (for both learning and non-learning). For our recorded dataset, as can be seen in figure 6.5, when point matches are

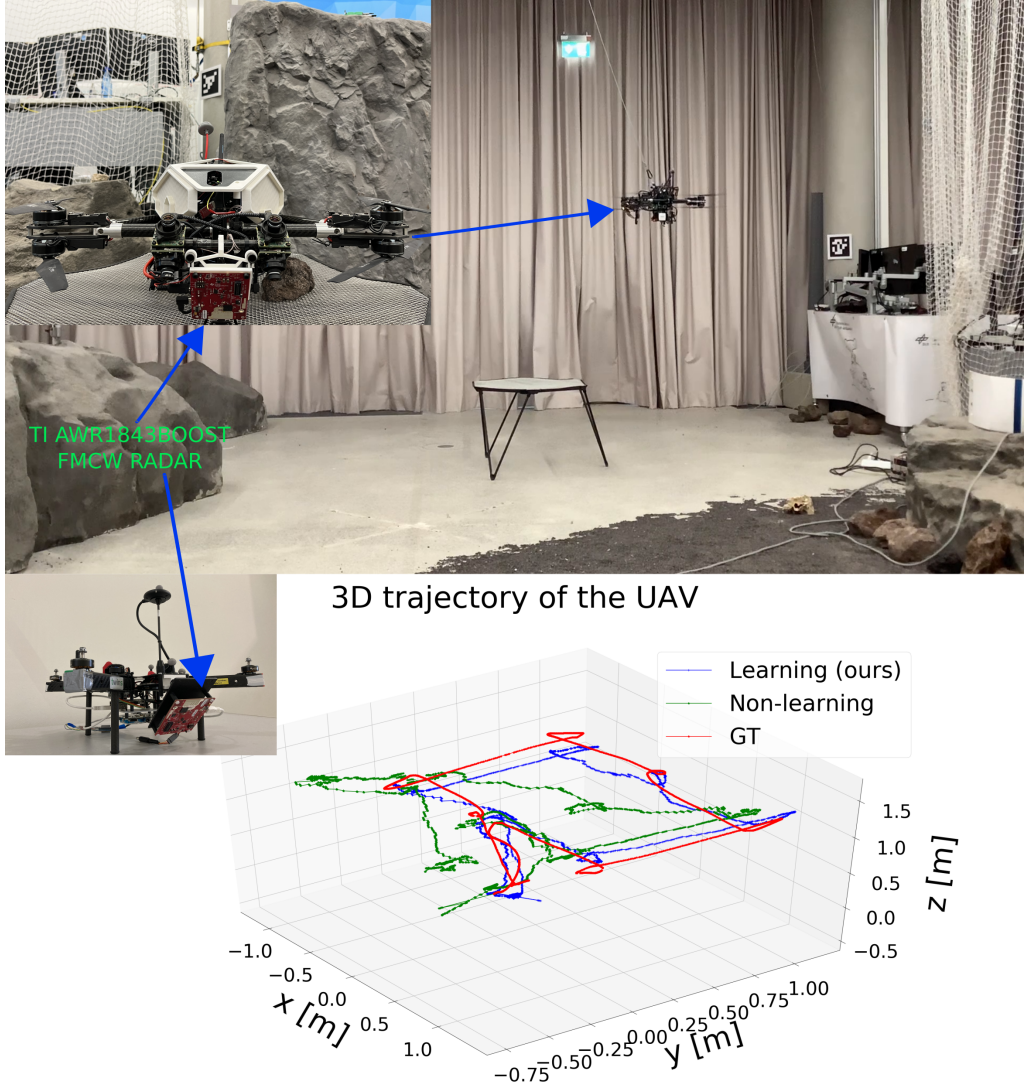


Figure 6.3: ARDEA-X [50] and CNS-UAV platforms used in this work with the mounted consumer-grade FMCW SoC radar sensor. The radar chip that we use outputs highly noisy and sparse 4D point clouds (3D points and Doppler velocities). In the lower part of the figure we plot the estimated position for one of the validation flights using the EKF-based RIO framework from section 4.3 when switching between matching methods and using *solely* 3D point matches in the update step. Note how the proposed method allows tracking the position of the UAV making *no* use of the Doppler information, while the non-learning approach drifts considerably.

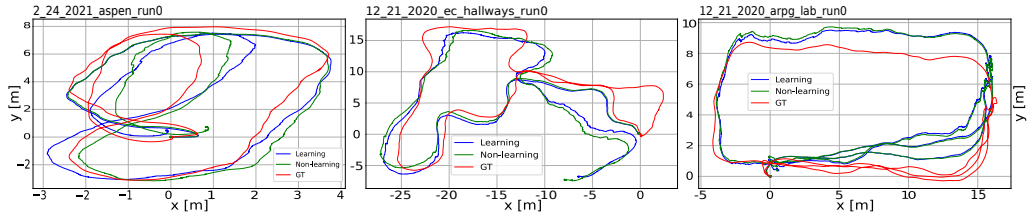


Figure 6.4: Three illustrative sequences (also used in [87]) out of five chosen from the Coloradar dataset for evaluation. From left to right: "2\_24\_2021\_aspen\_run0", "12\_21\_2020\_ec\_hallways\_run0", "12\_21\_2020\_arpg\_lab\_run0". In red we mark the ground-truth, and in green the non-learning and in blue the learning (proposed) approaches, respectively. Across all used Coloradar sequences, using our learning-based matching method results in a decrease of the norm of position RMSE by 19 %.

used as the sole source of information for measurement updates in the EKF RIO, the presented method allows for much more accurate estimation than the non-learning approach and when combined with the Doppler velocity measurements, greatly reduces the final error.

In figure 6.2, we can see how the trained network infers the correspondences. Note how matches 0 and 2 lie very close geometrically and hence points involved in them have all high mutual affinities, nevertheless, the network still makes correct distinction between them. Points involved in match 1, which also lie close to points involved in matches 0 and 2, do not have high affinity with points in 0, 2. This can be explained by looking at the middle plot and observing that on the  $xy$ -plane, points in match 1 are offset from points in 0 and 2. For points in matches 5 and 6, despite all of them being close on the  $xz$ -plane, our network correctly assigns the mutual affinities, since on the  $xy$ -plane, the points are clearly separated resulting in unambiguous matches. Points in matches 3, 4, 7 are significantly spaced in both planes, thus all have strong unambiguous mutual affinity values. Points (3, 5) are not considered a match despite their high mutual affinity because at least one of them is outside of the FOV. Similarly, the points (8, 10) are not counted as a match since their correspondence likelihood value is below the empirically determined acceptance threshold.

In figure 6.4 we plot the estimation results for three out of chosen five Coloradar sequences for both used matching methods. From the five sequences, "12\_21\_2020\_ec\_hallways\_run0", "2\_24\_2021\_aspen\_run0" and "12\_21\_2020\_arpg\_lab\_run0" are also chosen in the latest state-

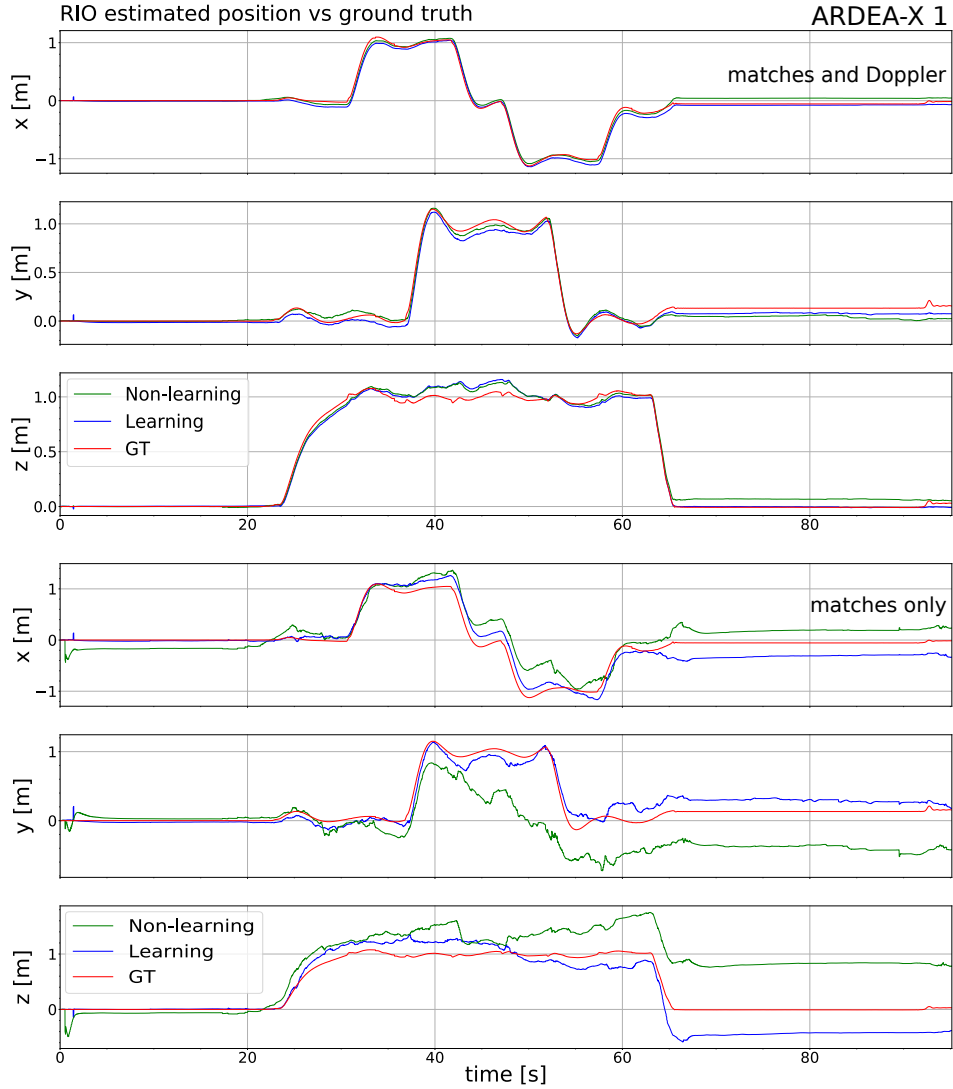


Figure 6.5: Estimated position of the ARDEA-X UAV for the flight 1 from the table 6.2 and table 6.1. We plot the  $x, y, z$  coordinates of the estimate against the ground-truth for the configuration with matches and Doppler, and only matches used in the update step of the EKF RIO framework used for validation. Each configuration is executed with the proposed learning-based and the default non-learning matching algorithm. In red the ground-truth, in green and blue non-learning and learning approaches, respectively.

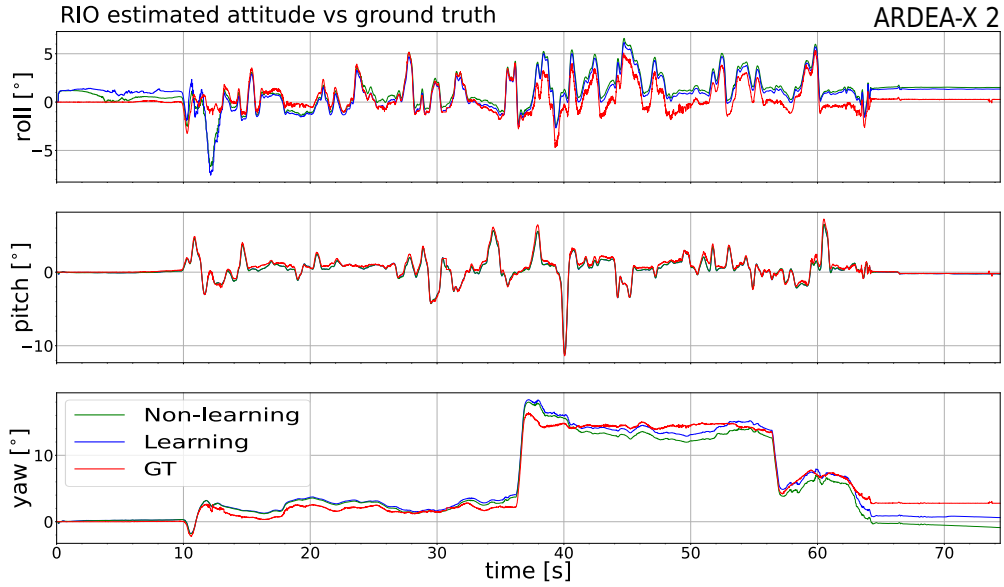


Figure 6.6: Estimated attitude of the ARDEA-X UAV for the flight 2 from the table 6.2 and table 6.1. We plot the roll, pitch and yaw angles of the estimate against the ground-truth for the configuration with matches and Doppler used in the update step of the EKF in RIO framework used for validation, when executed with the proposed learning-based (in blue) and the default non-learning matching algorithm (in green). In red we plot the ground-truth attitude.

of-the-art work on RIO presented in [87] where the authors also provide the norm of RMSE of position and attitude estimate for their method. This allows us to note that for sequences "2\_24\_2021\_aspen\_run0" and "12\_21\_2020\_arpq\_lab\_run0" our method outperforms [87] 3.044 m (ours) to 3.820 m and 5.388 m (ours) to 6.101 m, respectively in position and 13.372° (ours) to 30.905°, and 8.287° (ours) to 12.640°, respectively in attitude. For the sequence "12\_21\_2020\_ec\_hallways\_run0" our method performs worse, 9.927 m (ours) to 5.223 m in position as well as in attitude 18.357° (ours) to 16.070°.

Note, however, that in [87] the underlying estimator is different to the one we use here. Thus, we compare in table 6.1 and table 6.2 more rigorously the specific benefit of the learning-based matching. For this, we implement the RIO framework of section 4.3 with Doppler and point matches as well as only point matches from our learning based approach and with the orig-

inal non-learning approach. table 6.1 clearly shows that our learning based approach improves the performance in the position estimation in almost all runs. When using both Doppler and point matches, the improvement using our approach is in average over 14 % or a bit over 5 cm on our own datasets, and 19 % or 8 cm on the Coloradar datasets. With a standard deviation much higher than the improvements, these results have limited statistical relevance. However, when using only point matches, the improvement is much higher with over 70 % or nearly 1.5 m on our datasets. With a standard deviation of a bit over 18 cm, this clearly underlines the estimation improvement due to our approach. The Coloradar dataset trajectories are too agile for the estimator to work properly when not including Doppler information, hence the 'x' in the lower right part of the table.

The benefit of our approach regarding the attitude estimation is less clear. Using both Doppler and point matches we observe in average a decrease in performance of 5 % or roughly half a degree on both our and the Coloradar datasets. When only using point matches, we observe in average a bit more than 9 % or nearly 1 degree performance drop on our datasets. Note, however, that these differences are barely statistically relevant since the standard deviation in all cases is higher than 5 degrees for our approach. Thus, we can conclude that while our method has a clearly positive impact on the position estimate, the attitude barely benefits from the new approach. The root cause of the reduced benefit in attitude is to be investigated further – we assume a connection to the bad angular resolution and high angular noise that comes with this type of sensors. We plot the attitude estimates for one of the trajectories from the self-collected dataset in the Fig. 6.6.

### 6.3 Conclusions

In this paper, we presented a novel self-supervised learning framework for finding 3D point correspondences in sparse and noisy point clouds from a SoC FMCW radar. To our knowledge, this is the first learning approach addressing the problem of data association in the challenging setting of 3D point cloud measurements from low-cost, low-power, lightweight, consumer-grade radar chips. In our framework, we leverage the *PointNet* architecture to compute individual point embeddings in each of the two consecutive input point clouds. Subsequently, using transformer architecture and its attention mechanism, we augment the initial embeddings with the reciprocal information from both inputs, to finally form the matching likelihood matrix by calculating the dot product of the augmented embeddings. We

Table 6.1: RMSE norm values of position estimate for both matching methods across self-collected UAV flights and sequences from open-source Colordar dataset.

Nr	Self-collected dataset   RMSE   of position [m]			
	Doppler and matches		Matches only	
	Learning (ours)	Non learning	Learning (ours)	Non learning
1	<b>0.083</b>	0.101	<b>0.351</b>	0.748
2	<b>0.212</b>	0.272	<b>0.793</b>	1.795
3	0.714	<b>0.704</b>	<b>0.745</b>	1.608
4	0.380	<b>0.338</b>	<b>0.431</b>	1.074
5	<b>0.230</b>	0.473	<b>0.736</b>	5.088
Average	0.324	0.378	0.611	2.063
Std. dev.	0.217	0.202	0.183	1.558
Sequence	Colordar dataset   RMSE   of position [m]			
	aspen_run0	<b>3.044</b>	5.327	x x
arpg_lab_run0	<b>5.388</b>	6.080	x x	x
ec_hallways_run0	<b>9.927</b>	11.523	x x	x
aspen_run4	<b>5.315</b>	6.296	x x	x
aspen_run5	<b>3.466</b>	4.280	x x	x
Average	5.428	6.701	x x	x
Std. dev.	2.728	2.808	x x	x

provide a self-supervision method using set-based multi-label classification cross-entropy loss, where the ground-truth set of matches is calculated by solving the LSA optimization problem. Employing multi-label classification cross-entropy loss enables directly using correspondences in training. This is crucial since training on odometry error using e.g. SVD, as used in methods for scanning radars or dense point clouds, is not feasible with the sparse and noisy measurements from the SoC radar sensor that we use in this work. We applied our framework to the task of RIO estimation on a small-sized UAV and showed that it outperforms the default non-learning 3D point matching method. In particular, in an open-source state-of-the-art RIO framework we switched the 3D point matching algorithm from the

Table 6.2: RMSE norm values of attitude estimate for both matching methods across self-collected UAV flights and sequences from open-source Colordar dataset.

Nr	Self-collected dataset   RMSE   of attitude [°]			
	Matches and Doppler		Matches only	
	Learning (ours)	Non learning	Learning (ours)	Non learning
1	3.996	<b>3.203</b>	<b>0.966</b>	6.689
2	<b>1.642</b>	2.036	4.730	<b>3.597</b>
3	17.068	<b>16.945</b>	17.198	<b>17.067</b>
4	10.058	<b>9.712</b>	8.547	<b>6.234</b>
5	18.158	<b>16.551</b>	21.108	<b>14.305</b>
Average	10.184	9.689	10.510	9.578
Std. dev.	7.453	7.077	8.446	5.782
Sequence	Colordar dataset   RMSE   of attitude [°]			
	aspen_run0	13.372	<b>9.389</b>	x
arpg_lab_run0	8.287	<b>7.506</b>	x	x
ec_hallways_run0	<b>18.357</b>	21.666	x	x
aspen_run4	<b>7.776</b>	8.117	x	x
aspen_run5	9.363	<b>7.947</b>	x	x
Average	11.431	10.925	x	x
Std. dev.	6.045	4.451	x	x

default non-learning one to the one presented in this paper while keeping all other settings and parameters unchanged. The reduction in the norm of RMSE of position estimate calculated over the whole real-world validation dataset in both cases when only matches, and matches with Doppler velocity are used in the estimator reveals that our learning-based method surpasses the non-learning one. We make both our framework and the datasets open-source for the benefit of the research community.

# 7

## CHAPTER

---

# Discussion and Conclusions

## 7.1 Discussion

As SLAM technologies get more and more mature, a pertinent challenge which appears, is that of being able to deploy them in various environmental conditions including difficult outdoor as well as indoor scenarios. Those might entail limited visibility due to air obscurants such as fog, smoke or fine particles in the air. Recent advances in millimeter-wave FMCW radar technologies gave rise to a body of research directed at investigating localization methods utilizing small-sized SoC FMCW radar sensors as a way to mitigate the impact of the harsh environmental conditions on the autonomous systems. This dissertation and the findings therein aim at advancing this research specifically in the direction of the applicability on small-size UAVs. To that end, we limited our work to lightweight, consumer-grade sensors having negligible payload as it is crucial for hardware onboard small-size UAVs.

The proof-of-concept method presented in section 4.1 allowed us to conclude the suitability of radar sensors and their accurate distance measurements for UAV state estimation when fused with the IMU data. Motivated by our findings in this constrained environment context, we switched to a radar sensor providing 4D point clouds. This in turn allowed us to design a novel state-of-the-art RIO in which all 4D measurements are used to form residuals in the EKF update step. Extending the proposed novel EKF-based estimator by adding a buffer with several past radar poses along with their observed measurements enabled further accuracy improvement. Implementing online calibration capabilities significantly simplified the usage of the system while also reducing the RMSE and improving the consis-

tency. Efficient software implementation made open-source permitted us to test our EKF-based RIO in closed-loop flights and also in visually challenging conditions. Radar-based localization systems, as opposed to VIO, have no special requirements on initialization procedures since they provide directly metric scale measurements.

In chapter 5 we turned our attention to another state estimation paradigm, that is, the factor graph optimization in order to compare it in a *one-to-one* fashion with the EKF-based algorithm. Based on the undertaken analysis we could draw conclusions that on average both approaches perform similarly in terms of position RMSE. The difference between the two estimators becomes starker when we induce initialization errors which bring the linearization points away from the true state values. In these conditions we observe the benefits of the iterations in the form of faster convergence of the factor graph approach. Nevertheless, it is not to be concluded that the factor graph optimization methods are univocally superior to filters. While exhibiting more resilience towards wrong initialization, they suffer from errors introduced by marginalization. Also, the emerging equivariant filter paradigm is poised to significantly improve the convergence properties of non-iterative filters [29].

Identifying the front-end robustness in RIO systems as of crucial importance, we dedicate the chapter 6 to research into improving the 3D point correspondence finding within sparse and noisy FMCW radar point clouds. To that end, we resort to the deep learning and the transformer architecture which lends itself to finding mutual affinities of points in subsequent 3D radar scans thanks to its attention mechanism.

All in all, we make a step forward on a path towards AI-backed RIO estimators with online calibration capabilities and deployable onboard in closed-loop flights in computationally constrained hardware, thus offering UAV localization system with strong environmental resilience using only consumer-grade sensors.

## 7.2 Conclusions

In conclusion, this dissertation offers successful research advancements in the area of RIO applied to small-sized UAVs using consumer-grade, lightweight and commonly available sensors and computing hardware. Several RIO estimator formulations presented therein together with their successful deployment on real-world platforms, insights into their respective strengths and weaknesses, as well as the application of deep learning methods to im-

prove their front-end processing offer significant progress on the way to the utilization of radar sensors in the area of UAV perception.

---

## Bibliography

- [1] Pratik Agarwal, Gian Diego Tipaldi, Luciano Spinello, Cyrill Stachniss, and Wolfram Burgard. Robust map optimization using dynamic covariance scaling. In *2013 IEEE International Conference on Robotics and Automation*, pages 62–69, 2013.
- [2] Roberto Aldera, Matthew Gadd, Daniele De Martini, and Paul Newman. What goes around: Leveraging a constant-curvature motion constraint in radar odometry. *IEEE Robotics and Automation Letters*, 7(3):7865–7872, 2022.
- [3] Roberto Aldera, Daniele De Martini, Matthew Gadd, and Paul Newman. What could go wrong? introspective radar odometry in challenging environments. In *2019 IEEE Intelligent Transportation Systems Conference (ITSC)*, pages 2835–2842, 2019.
- [4] Yasin Almalioglu, Mehmet Turan, Chris Xiaoxuan Lu, Niki Trigoni, and Andrew Markham. Milli-rio: Ego-motion estimation with low-cost millimetre-wave radar. *IEEE Sensors Journal*, 21(3):3314–3323, 2020.
- [5] Yaakov bar shalom, X.-Rong Li, and Thia Kirubarajan. *Estimation with Applications to Tracking and Navigation: Theory, Algorithms and Software*. 01 2004.
- [6] Dan Barnes and Ingmar Posner. Under the radar: Learning to predict robust keypoints for odometry estimation and metric localisation in radar. In *2020 IEEE International Conference on Robotics and Automation (ICRA)*, pages 9484–9490. IEEE, 2020.

- [7] P.J. Besl and Neil D. McKay. A method for registration of 3-d shapes. *IEEE Transactions on Pattern Analysis and Machine Intelligence*, 14(2):239–256, 1992.
- [8] Julian Blueml, Alessandro Fornasier, and Stephan Weiss. Bias compensated uwb anchor initialization using information-theoretic supported triangulation points. In *2021 IEEE International Conference on Robotics and Automation (ICRA)*. IEEE, 2021.
- [9] Keenan Burnett, Angela P. Schoellig, and Timothy D. Barfoot. Do we need to compensate for motion distortion and doppler effects in spinning radar navigation? *IEEE Robotics and Automation Letters*, 6(2):771–778, 2021.
- [10] Keenan Burnett, Angela P. Schoellig, and Timothy D. Barfoot. Continuous-time radar-inertial and lidar-inertial odometry using a gaussian process motion prior. *IEEE Transactions on Robotics*, 41:1059–1076, 2025.
- [11] Keenan Burnett, David J Yoon, Angela P Schoellig, and Timothy D Barfoot. Radar odometry combining probabilistic estimation and unsupervised feature learning. *arXiv preprint arXiv:2105.14152*, 2021.
- [12] Keenan Burnett, David J. Yoon, Angela P. Schoellig, and Timothy D. Barfoot. Radar odometry combining probabilistic estimation and unsupervised feature learning. *CoRR*, abs/2105.14152, 2021.
- [13] Sarah H Cen and Paul Newman. Precise ego-motion estimation with millimeter-wave radar under diverse and challenging conditions. In *2018 IEEE International Conference on Robotics and Automation (ICRA)*, pages 6045–6052. IEEE, 2018.
- [14] R. Qi Charles, Hao Su, Mo Kaichun, and Leonidas J. Guibas. Pointnet: Deep learning on point sets for 3d classification and segmentation. In *2017 IEEE Conference on Computer Vision and Pattern Recognition (CVPR)*, pages 77–85, 2017.
- [15] Chuchu Chen, Yuxiang Peng, and Guoquan Huang. Is iteration worth it? revisit its impact in sliding-window vio. In *2025 IEEE International Conference on Robotics and Automation (ICRA)*, pages 1060–1066, 2025.
- [16] Hongyu Chen, Yimin Liu, and Yuwei Cheng. Drio: Robust radar-inertial odometry in dynamic environments. *IEEE Robotics and Automation Letters*, 8(9):5918–5925, 2023.

- [17] Yuwei Cheng, Jingran Su, Mengxin Jiang, and Yimin Liu. A novel radar point cloud generation method for robot environment perception. *IEEE Transactions on Robotics*, 38(6):3754–3773, 2022.
- [18] Angelo Coluccia, Alessio Fascista, and Giuseppe Ricci. Cfar feature plane: A novel framework for the analysis and design of radar detectors. *IEEE Transactions on Signal Processing*, 68:3903–3916, 2020.
- [19] Frank Dellaert and GTSAM Contributors. borglab/gtsam, May 2022.
- [20] Frank Dellaert, Michael Kaess, et al. Factor graphs for robot perception. *Foundations and Trends® in Robotics*, 6(1-2):1–139, 2017.
- [21] Nikolaus Demmel, David Schubert, Christiane Sommer, Daniel Cremers, and Vladyslav Usenko. Square Root Marginalization for Sliding-Window Bundle Adjustment . In *2021 IEEE/CVF International Conference on Computer Vision (ICCV)*, pages 13240–13248, Los Alamitos, CA, USA, October 2021. IEEE Computer Society.
- [22] Christopher Doer, Jamal Atman, and Gert F. Trnmmer. Gnss aided radar inertial odometry for uas flights in challenging conditions. In *2022 IEEE Aerospace Conference (AERO)*, pages 1–10, 2022.
- [23] Christopher Doer and Gert F Trommer. An ekf based approach to radar inertial odometry. In *2020 IEEE International Conference on Multisensor Fusion and Integration for Intelligent Systems (MFI)*, pages 152–159. IEEE, 2020.
- [24] Christopher Doer and Gert F Trommer. Radar inertial odometry with online calibration. In *2020 European Navigation Conference (ENC)*, pages 1–10. IEEE, 2020.
- [25] Christopher Doer and Gert F. Trommer. Yaw aided radar inertial odometry using manhattan world assumptions. In *2021 28th Saint Petersburg International Conference on Integrated Navigation Systems (ICINS)*, pages 1–9, 2021.
- [26] Christopher Doer and Gert F. Trommer. Yaw aided radar inertial odometry using manhattan world assumptions. In *2021 28th Saint Petersburg International Conference on Integrated Navigation Systems (ICINS)*, pages 1–9, 2021.
- [27] Armin Walter Doerry. Reflectors for sar performance testing. Technical report, Sandia National Laboratories, 2008.

- [28] Alessandro Fornasier, Yonhon Ng, Robert Mahony, and Stephan Weiss. Equivariant filter design for inertial navigation systems with input measurement biases. In *2022 International Conference on Robotics and Automation (ICRA)*, pages 4333–4339, 2022.
- [29] Alessandro Fornasier, Pieter van Goor, Eren Allak, Robert Mahony, and Stephan Weiss. Msceqf: A multi state constraint equivariant filter for vision-aided inertial navigation. *IEEE Robotics and Automation Letters*, 9(1):731–738, 2024.
- [30] Christian Forster, Luca Carlone, Frank Dellaert, and Davide Scaramuzza. On-manifold preintegration for real-time visual–inertial odometry. *IEEE Transactions on Robotics*, 33(1):1–21, 2016.
- [31] Pengen Gao, Shengkai Zhang, Wei Wang, and Chris Xiaoxuan Lu. Dc-loc: Accurate automotive radar based metric localization with explicit doppler compensation. In *2022 International Conference on Robotics and Automation (ICRA)*, pages 4128–4134, 2022.
- [32] Patrick Geneva, Kevin Eckenhoff, Woosik Lee, Yulin Yang, and Guoquan Huang. Openvins: A research platform for visual-inertial estimation. In *2020 IEEE International Conference on Robotics and Automation (ICRA)*, pages 4666–4672. IEEE, 2020.
- [33] Meng-Hao Guo, Jun-Xiong Cai, Zheng-Ning Liu, Tai-Jiang Mu, Ralph R. Martin, and Shi-Min Hu. Pct: Point cloud transformer. *Computational Visual Media*, 7(2):187–199, April 2021.
- [34] Kyle Harlow, Hyesu Jang, Timothy D. Barfoot, Ayoung Kim, and Christoffer Heckman. A new wave in robotics: Survey on recent mmwave radar applications in robotics. *IEEE Transactions on Robotics*, 40:4544–4560, 2024.
- [35] Jürgen Hasch, Eray Topak, Raik Schnabel, Thomas Zwick, Robert Weigel, and Christian Waldschmidt. Millimeter-wave technology for automotive radar sensors in the 77 ghz frequency band. *IEEE Transactions on Microwave Theory and Techniques*, 60(3):845–860, 2012.
- [36] Ziyang Hong, Yvan Petillot, and Sen Wang. Radarslam: Radar based large-scale slam in all weathers. In *2020 IEEE/RSJ International Conference on Intelligent Robots and Systems (IROS)*, pages 5164–5170, 2020.

- [37] Guoquan Huang, Michael Kaess, and John J. Leonard. Towards consistent visual-inertial navigation. In *2014 IEEE International Conference on Robotics and Automation (ICRA)*, pages 4926–4933, 2014.
- [38] Qiucan Huang, Yuchen Liang, Zhijian Qiao, Shaojie Shen, and Huan Yin. Less is more: Physical-enhanced radar-inertial odometry. In *2024 IEEE International Conference on Robotics and Automation (ICRA)*, pages 15966–15972, 2024.
- [39] Eagle Jones and Stefano Soatto. Visual-inertial navigation, mapping and localization: A scalable real-time causal approach. *I. J. Robotic Res.*, 30:407–430, 12 2011.
- [40] Jonathan Kelly and Gaurav Sukhatme. Visual-inertial sensor fusion: Localization, mapping and sensor-to-sensor self-calibration. *I. J. Robotic Res.*, 30:56–79, 01 2011.
- [41] Andrew Kramer, Kyle Harlow, Christopher Williams, and Christoffer Heckman. Coloradar: The direct 3d millimeter wave radar dataset. *The International Journal of Robotics Research*, 41(4):351–360, 2022.
- [42] Andrew Kramer and Christoffer Heckman. *Radar-Inertial State Estimation and Obstacle Detection for Micro-Aerial Vehicles in Dense Fog*, pages 3–16. 03 2021.
- [43] Andrew Kramer, Carl Stahoviak, Angel Santamaria-Navarro, Ali-Akbar Agha-Mohammadi, and Christoffer Heckman. Radar-inertial ego-velocity estimation for visually degraded environments. In *2020 IEEE International Conference on Robotics and Automation (ICRA)*, pages 5739–5746. IEEE, 2020.
- [44] Matthias Kronauge and Hermann Rohling. Fast two-dimensional cfar procedure. *IEEE Transactions on Aerospace and Electronic Systems*, 49(3):1817–1823, 2013.
- [45] Vladimír Kubelka, Emil Fritz, and Martin Magnusson. Do we need scan-matching in radar odometry? In *2024 IEEE International Conference on Robotics and Automation (ICRA)*, pages 13710–13716, 2024.
- [46] Stefan Leutenegger, Simon Lynen, Michael Bosse, Roland Siegwart, and Paul Furgale. Keyframe-based visual–inertial odometry using non-linear optimization. *The International Journal of Robotics Research*, 34(3):314–334, 2015.

- [47] Mingyang Li and Anastasios Mourikis. High-precision, consistent ekf-based visual–inertial odometry. *The International Journal of Robotics Research*, 32:690–711, 05 2013.
- [48] Xingyi Li, Han Zhang, and Weidong Chen. 4d radar-based pose graph slam with ego-velocity pre-integration factor. *IEEE Robotics and Automation Letters*, 8(8):5124–5131, 2023.
- [49] Xingyi Li, Han Zhang, and Weidong Chen. 4d radar-based pose graph slam with ego-velocity pre-integration factor. *IEEE Robotics and Automation Letters*, 8(8):5124–5131, 2023.
- [50] Philipp Lutz, Marcus G. Müller, Moritz Maier, Samantha Stoneman, Teodor Tomić, Ingo von Bargen, Martin J. Schuster, Florian Steidle, Armin Wedler, Wolfgang Stürzl, and Rudolph Triebel. Ardea—an mav with skills for future planetary missions. *Journal of Field Robotics*, 37(4):515–551, 2020.
- [51] A Martinelli. Visual-inertial structure from motion: observability and resolvability, iros 2013. *Tokyo, Japan*.
- [52] P.S. Maybeck. *Stochastic Models, Estimation and Control*. Number pt. 1 in Mathematics in science and engineering. Academic Press, 1979.
- [53] Jan Michalczyk, Roland Jung, Christian Brommer, and Stephan Weiss. Multi-state tightly-coupled ekf-based radar-inertial odometry with persistent landmarks. In *2023 IEEE International Conference on Robotics and Automation (ICRA)*, pages 4011–4017, 2023.
- [54] Jan Michalczyk, Roland Jung, and Stephan Weiss. Tightly-coupled ekf-based radar-inertial odometry. In *2022 International Conference on Intelligent Robots and Systems (IROS)*. IEEE, Accepted June 2022.
- [55] Jan Michalczyk, Julius Quell, Florian Steidle, Marcus G. Müller, and Stephan Weiss. Tightly-coupled factor graph formulation for radar-inertial odometry. In *2024 IEEE/RSJ International Conference on Intelligent Robots and Systems (IROS)*, pages 3364–3370, 2024.
- [56] Jan Michalczyk, Christian Schöffmann, Alessandro Fornasier, Jan Steinbrenner, and Stephan Weiss. Radar-inertial state-estimation for uav motion in highly agile manoeuvres. In *2022 International Conference on Unmanned Aircraft Systems (ICUAS)*, pages 583–589, 2022.

- [57] Jan Michalczyk, Stephan Weiss, and Jan Steinbrener. Learning point correspondences in radar 3d point clouds for radar-inertial odometry. *arXiv:2506.18580v1*, 2025.
- [58] Anastasios I. Mourikis and Stergios I. Roumeliotis. A multi-state constraint kalman filter for vision-aided inertial navigation. In *Proceedings 2007 IEEE International Conference on Robotics and Automation*, pages 3565–3572, 2007.
- [59] Anastasios I. Mourikis and Stergios I. Roumeliotis. A multi-state constraint kalman filter for vision-aided inertial navigation. In *Proceedings 2007 IEEE International Conference on Robotics and Automation*, pages 3565–3572, 2007.
- [60] James Munkres. Algorithms for the assignment and transportation problems. *Journal of the society for industrial and applied mathematics*, 5(1):32–38, 1957.
- [61] Yin Zhi Ng, Benjamin Choi, Robby Tan, and Lionel Heng. Continuous-time radar-inertial odometry for automotive radars. In *2021 IEEE/RSJ International Conference on Intelligent Robots and Systems (IROS)*, pages 323–330, 2021.
- [62] Yin Zhi Ng, Benjamin Choi, Robby Tan, and Lionel Heng. Continuous-time radar-inertial odometry for automotive radars. In *2021 IEEE/RSJ International Conference on Intelligent Robots and Systems (IROS)*, pages 323–330, 2021.
- [63] Morten Nissov, Nikhil Khedekar, and Kostas Alexis. Degradation resilient lidar-radar-inertial odometry. In *2024 IEEE International Conference on Robotics and Automation (ICRA)*, pages 8587–8594, 2024.
- [64] Yeong Sang Park, Young-Sik Shin, and Ayoung Kim. Pharao: Direct radar odometry using phase correlation. In *2020 IEEE International Conference on Robotics and Automation (ICRA)*, pages 2617–2623. IEEE, 2020.
- [65] Yeong Sang Park, Young-Sik Shin, Joowan Kim, and Ayoung Kim. 3d ego-motion estimation using low-cost mmwave radars via radar velocity factor for pose-graph slam. *IEEE Robotics and Automation Letters*, 6(4):7691–7698, 2021.
- [66] Tong Qin, Peiliang Li, and Shaojie Shen. Vins-mono: A robust and versatile monocular visual-inertial state estimator. *IEEE Transactions on Robotics*, 34(4):1004–1020, 2018.

- [67] Kyle Retan, Frasher Loshaj, and Michael Heizmann. Radar odometry on  $se(3)$  with constant velocity motion prior. *IEEE Robotics and Automation Letters*, 6(4):6386–6393, 2021.
- [68] M.A. Richards. *Fundamentals of Radar Signal Processing*. Professional Engineering. McGraw-Hill Education, 2005.
- [69] Hermann Rohling and M-M Meinecke. Waveform design principles for automotive radar systems. In *2001 CIE International Conference on Radar Proceedings (Cat No. 01TH8559)*, pages 1–4. IEEE, 2001.
- [70] Stergios I Roumeliotis and Joel W Burdick. Stochastic cloning: A generalized framework for processing relative state measurements. In *Proceedings 2002 IEEE International Conference on Robotics and Automation (Cat. No. 02CH37292)*, volume 2, pages 1788–1795. IEEE, 2002.
- [71] Martin Schneider. Automotive radar-status and trends. In *German microwave conference*, pages 144–147, 2005.
- [72] F. Schuster, C. G. Keller, M. Rapp, M. Haueis, and C. Curio. Landmark based radar slam using graph optimization. In *2016 IEEE 19th International Conference on Intelligent Transportation Systems (ITSC)*, pages 2559–2564, 2016.
- [73] Christian Schöffmann, Barnaba Ubezio, Christoph Böhm, Stephan Mühlbacher-Karrer, and Hubert Zangl. Virtual radar: Real-time millimeter-wave radar sensor simulation for perception-driven robotics. *IEEE Robotics and Automation Letters*, 6(3):4704–4711, 2021.
- [74] J. Sola, A. Monin, M. Devy, and T. Lemaire. Undelayed initialization in bearing only slam. In *2005 IEEE/RSJ International Conference on Intelligent Robots and Systems*, pages 2499–2504, 2005.
- [75] Hannes Sommer, Igor Gilitschenski, Michael Bloesch, Stephan Weiss, Roland Siegwart, and Juan Nieto. Why and how to avoid the flipped quaternion multiplication. *Aerospace*, 5(3):72, 2018.
- [76] Cagatay Uluisik, Gonca Cakir, Mustafa Cakir, and Levent Sevgi. Radar cross section (rcs) modeling and simulation, part 1: a tutorial review of definitions, strategies, and canonical examples. *IEEE Antennas and Propagation Magazine*, 50(1):115–126, 2008.

- [77] Ashish Vaswani, Noam Shazeer, Niki Parmar, Jakob Uszkoreit, Llion Jones, Aidan N Gomez, Łukasz Kaiser, and Illia Polosukhin. Attention is all you need. In I. Guyon, U. Von Luxburg, S. Bengio, H. Wallach, R. Fergus, S. Vishwanathan, and R. Garnett, editors, *Advances in Neural Information Processing Systems*, volume 30. Curran Associates, Inc., 2017.
- [78] Arthur Venon, Yohan Dupuis, Pascal Vasseur, and Pierre Meriaux. Millimeter wave fmcw radars for perception, recognition and localization in automotive applications: A survey. *IEEE Transactions on Intelligent Vehicles*, 7(3):533–555, 2022.
- [79] Yue Wang and Justin Solomon. Deep closest point: Learning representations for point cloud registration. In *2019 IEEE/CVF International Conference on Computer Vision (ICCV)*, pages 3522–3531, 2019.
- [80] Stephan Weiss, Markus W Achtelik, Margarita Chli, and Roland Siegwart. Versatile distributed pose estimation and sensor self-calibration for an autonomous mav. In *2012 IEEE International Conference on Robotics and Automation*, pages 31–38. IEEE, 2012.
- [81] Stephan Weiss and Roland Siegwart. Real-time metric state estimation for modular vision-inertial systems. In *2011 IEEE International Conference on Robotics and Automation*, pages 4531–4537, 2011.
- [82] Emmett Wise, Juraj Peršić, Christopher Grebe, Ivan Petrović, and Jonathan Kelly. A continuous-time approach for 3d radar-to-camera extrinsic calibration. In *2021 IEEE International Conference on Robotics and Automation (ICRA)*, pages 13164–13170, 2021.
- [83] Xiaoyi Wu, Yushuai Chen, Zhan Li, Ziyang Hong, and Liang Hu. Efear-4d: Ego-velocity filtering for efficient and accurate 4d radar odometry. *IEEE Robotics and Automation Letters*, 9(11):9828–9835, 2024.
- [84] Chunmei Xu, Yang Li, Chao Ji, Yongming Huang, Haiming Wang, and Yili Xia. An improved cfar algorithm for target detection. In *2017 International Symposium on Intelligent Signal Processing and Communication Systems (ISPACS)*, pages 883–888, 2017.
- [85] Wei Xu, Yixi Cai, Dongjiao He, Jiarong Lin, and Fu Zhang. Fast-lio2: Fast direct lidar-inertial odometry. *IEEE Transactions on Robotics*, 38(4):2053–2073, 2022.

- [86] Wei Xu and Fu Zhang. Fast-lio: A fast, robust lidar-inertial odometry package by tightly-coupled iterated kalman filter. *IEEE Robotics and Automation Letters*, 6(2):3317–3324, 2021.
- [87] Yang Xu, Qiucan Huang, Shaojie Shen, and Huan Yin. Incorporating point uncertainty in radar slam. *IEEE Robotics and Automation Letters*, 10(3):2168–2175, 2025.
- [88] Qiangwen Zheng, Lijie Yang, Yaping Xie, Junjie Li, Tang Hu, Jiang Zhu, Chunyi Song, and Zhiwei Xu. A target detection scheme with decreased complexity and enhanced performance for range-doppler fmcw radar. *IEEE Transactions on Instrumentation and Measurement*, 70:1–13, 2021.
- [89] Jinwen Zhu, Jun Hu, Xudong Zhao, Xiaoming Lang, Yinian Mao, and Guoquan Huang. Robust 4d radar-aided inertial navigation for aerial vehicles. In *2025 IEEE International Conference on Robotics and Automation (ICRA)*, pages 9848–9854, 2025.
- [90] Yuan Zhuang, Binliang Wang, Jianzhu Huai, and Miao Li. 4d iriom: 4d imaging radar inertial odometry and mapping. *IEEE Robotics and Automation Letters*, 8(6):3246–3253, 2023.